Electronic Molecular Detection: from Proteins to Neurons

Andrei Afanasiev

A dissertation
submitted in partial fulfillment of the
requirements for the degree of

Doctor of Philosophy

University of Washington
2014

Reading Committee:
Karl Böhringer, Chair
Jeffrey Ojemann
Brian Otis

Program Authorized to Offer Degree:
Electrical Engineering

University of Washington

Abstract

Electronic Molecular Detection:
from Proteins to Neurons

Andrei Afanasiev

Chair of the Supervisory Committee:
Professor Karl Böhringer
Department of Electrical Engineering

This dissertation presents my research investigating a number of microscale devices designed to interact with various biological systems. First, I describe the development of nanoscale electronic sensor devices for quantitative detection of biomolecule concentrations in liquids. Two sensor designs are discussed – one using semiconducting nanowires and another employing a novel fluid nanochannel layout. Microfabrication and sensor performance optimization methods are discussed, culminating with an overview of molecular sensing results. Second, I describe an effort undertaken in support of a project aimed at creating a contact lens based glucose sensor. A miniature version of the sensor was created and tested in-vivo, inside a rabbit's eye, using the intraocular fluid as an ersatz tear fluid. Also, described is an anatomically correct model of a human eye, complete with moving eyelids and working tear ducts, used for testing contact lens sensors in a life-like environment. This effort has helped focus further development of the contact lens sensor project on solving the issue of chemical interference in in-vivo environments. Lastly, I describe design, microfabrication and in-vivo testing of implantable, highly flexible, non-invasive active neural electrode arrays used in an effort to create a fully implantable and wirelessly powered brain-computer interface system. Multiple array geometries for both subcranial and intraspinal implantation as well as their in-vitro and in-vivo performance are discussed. Ultimately, I present an active electrode array assembled with four neural signal amplifiers, using a novel two-sided parylene process.

Table of Contents

Table of Figures

1 Introduction

The future of medical diagnostics and therapeutic interventions lies deeply rooted in our ability to reliably quantify, in real time, the various chemical processes regulating our bodies' functions. Infectious and inflammatory diseases telegraph their progress via a slew of biochemical markers that if promptly and accurately detected can facilitate a proper treatment plan. Diabetes, a chronic disease, can be effectively managed if timely information can be obtained about the concentration of sugar in the blood. Neural disorders and trauma can also be either treated or managed through accurate measurements and counteractive stimulation of neural matter.

Using nanoscale fabrication techniques, one is able to create functional devices that can directly interact with many of the biologically important entities such as biomolecules (5-10 nm in diameter) or neurons (>5 μm in width.) Further exploiting the nano- and micro-scale characteristics of such devices, we can use many of the principles and physics developed over the years in the field of semiconductors to our advantage, in order to design novel ways of interacting with biological matter. The manufacturability aspect cannot be overlooked either, as one is able to utilize the cost-optimized fabrication capacity originally intended for semiconductor manufacturing, to develop biological sensor devices that, in the future, can be cheaply and reliably fabricated on very large scales.

In this thesis I describe, in three parts, the development of novel microfabricated devices designed to interact with various biological systems. The first part discusses the development and characterization of nanoscale biomolecule sensors that were made in support of the University of Washington's Microscale Life Sciences Center's mission to create the scientific tools necessary to quantifiably describe the chemical environment surrounding a single cell. The task dictated the requirements for the device. It must be made small enough for a number of such sensors to fit into a circular cavity that is only slightly larger than a macrophage cell – around 10 microns in diameter.

The devices must be able to query several different pertinent biomolecular targets and be sensitive to very small quantities of those targets. We have pursued two separate sensor designs. First, a semiconductor nanowire based sensor in which the target biomolecules are trapped on the surface of the nanowire and change its conduction characteristics by effectively electronically gating it. Second, a fluidic nanochannel based sensor that exploits the fact that most biomolecular targets are nanoscale in size, and can modulate the current through the nanochannel by being trapped on the nanochannel's walls, constricting its inner cross section, and thus decreasing its ability to conduct electrical current.

The second part of the thesis describes the effort that was performed in support of my research lab's development of an eye based glucose sensor. Rooted in a finding that the glucose content of tear fluid is closely related to blood glucose content, my group has designed an alternative to the painful "finger prick" style blood glucose test. Testing the tear fluid promises to be minimally invasive and provide a real time reading of an individual's blood glucose content. In this section I describe a microfabricated intraocular glucose sensor that was tested in a pseudo-in-vivo environment – a removed rabbit's eye. This test has provided us with the first in-vivo data, whereas the majority of the previous experiments have been done in-vitro. I also describe development of a mechanical system that simulates the tear fluid distribution and blinking motion of a human eye. The computer controlled PDMS eye model simulates the workings of tear ducts, an eyeball, an eyelid, and a mechanism that simulates the blinking motion of the eyelid against the eye. This model provides a much more realistic testing environment for contact lens based glucose sensors without having to go through the difficulties and expense of in-vivo experiments.

Lastly, I describe my work with neural interfaces – work that has been done as part of the Keck Neural Electrodes project whose primary goal was to design and fabricate a noninvasive, implantable recurrent brain computer interface (RBCI). The proposed RBCI contained a subcranial, cortical electrode array capable of recording and analyzing the signals on the motor cortex, as well

as a spinal array capable of electrically stimulating the nerves in the spinal cord per the "instructions" of the motor cortex. In support of that goal I have developed a microfabrication process for producing parylene based platinum and iridium oxide neural electrode arrays, extensively tested their in-vitro and in-vivo characteristics, as well as their capacity for long-term deployment. Furthermore, I have developed a novel microfabrication process capable of reliably producing two-sided flexible active neural electrode arrays. Such arrays place all the necessary electronic circuitry on one side of the flexible substrate, while keeping the opposite, electrode containing side as flat as possible in order to safely interact with neural matter. Such an active array employing a low noise neural amplifier has been tested in-vivo, measuring the somatosensory evoked potential (SEP) of a rat.

2 Biomolecular Detection

Most low level protein sensing is carried out by means of radiochemical, fluorescent or enzymatic tags. However, there are also several sensing principles that do not necessitate the use of a label (Daniels, 2007; Grieshaber, 2008). The most successful example of such an approach is surface plasmon resonance (SPR), which has been a valuable tool in protein quantification and binding studies for more than a decade (Homola 2008). Many of these methods, however, rely on expensive and bulky optical equipment (Armani, 2007). Ideally, a sensor needs to be label-free, allow for real-time detection of target molecules and can operate in very small sample volumes and target concentrations. Electronic molecular detection – the use of electronic devices which can translate a concentration of a biomolecule in solution into an electrical signal – satisfies all three requirements (Nair, 2007; Curreli, 2008; Stern, 2007). Furthermore, microfabricated electronic sensors can be easily arrayed in large numbers, allowing for multiple target detection in a single sample. By using standard microfabrication techniques one can create sensors that can be easily

integrated into lab-on-a-chip systems, integrating the signal readout circuitry in the immediate vicinity of the sensor for a truly stand-alone system.

2.1 Nanochannel Biomolecular Sensors

Recent research activities on nanoscale phenomena have produced yet another label-free sensing principle: nanochannel conductance (Stein 2004; Durand 2009; Ali 2010). It is based on measuring conductance along an electrolyte filled channel that has a cross-sectional area comparable to macromolecule dimensions. Protein binding onto the channel walls reduces the free cross-sectional area, thus leading to a reduction in the observed conductance. Such a device can be made analyte-specific by coating the channel walls with a material that selectively binds to the target molecule. (Karnik 2005)

2.1.1 Nanochannel Device Design Overview

Most present designs for nanochannel conductance sensing involve an arrangement where the channel is separating two symmetric solution compartments, each containing an electrode. Such designs are ideal for making precise conductance measurements, but do not lend themselves well to constructing practical sensors. Instead, I present a nanochannel architecture, specifically designed for stand-alone sensor applications that lends itself well to integration with Complementary Metal Oxide Semiconductor (CMOS) read-out circuitry.

My device consists of a set of ten, 2.25 μm long, 60 nm tall nanoscale channels with varying widths, fabricated in silicon dioxide. The sensor contains a gold electrode (working electrode), which probes the inner volume of the nanochannel. A second electrode (counter electrode) is located in the immediate vicinity outside of the nanochannel. The nanochannels are open on one end which allows for liquid to enter, and terminate at the working electrode on the other end. By using an electrolyte solution with a redox-active component, I characterize the conductance of the nanochannels with respect to their cross sectional area.

Differences in the cross sectional area are detected electronically, and as I have found, the conductance is directly proportional to the cross section of the nanochannel in the size regime covered here.

This approach is unique in the sense that it can potentially produce a self-contained amperometric biosensor, using standard fabrication techniques, without the need for external electrodes or complicated fluidic systems to create pressure differentials (Goluch 2009; Kutchoukov 2005; Maleki 2009). The device is small enough to be integrated into large arrays of similar structures, allowing for multiplexed sensing of various target molecules.

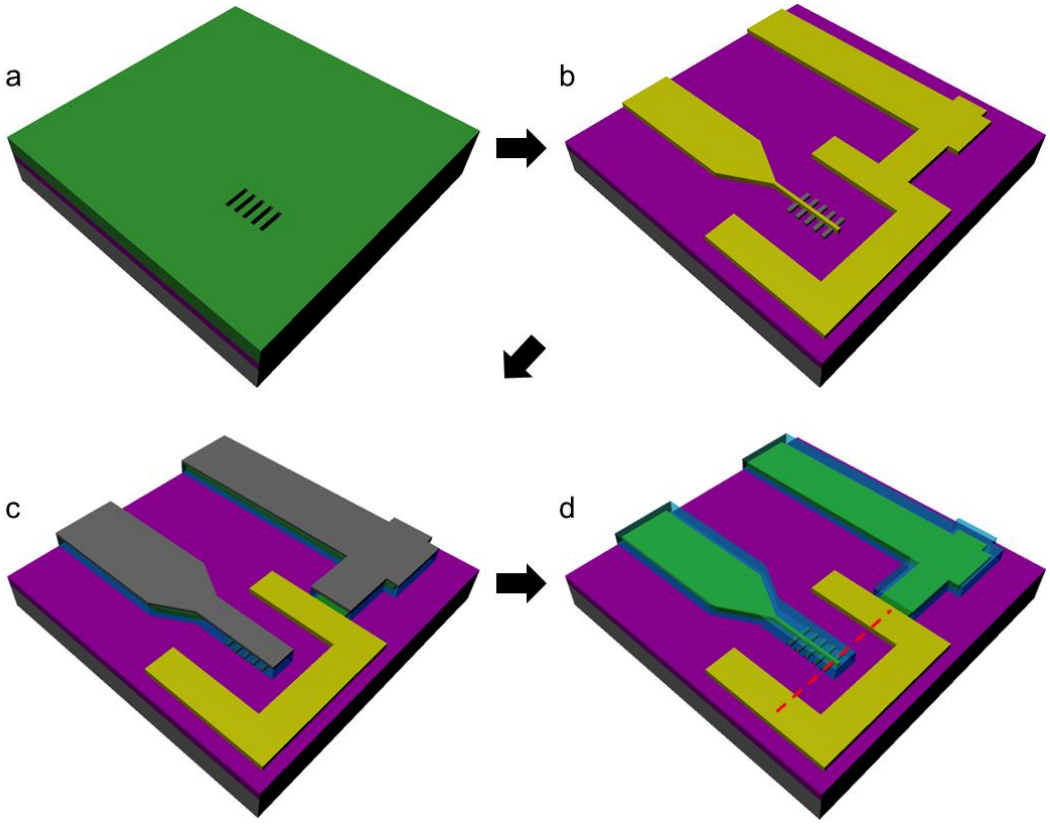

Figure 1. Nanochannel fabrication process. a) Silicon wafer is coated with electron beam resist and a set of five parallel nanowires is patterned using electron beam lithography (EBL). b) After a nickel evaporation which forms the nanowires, working and counter electrodes are patterned over the Ni nanowires using EBL and gold is thermally evaporated. c) A Si_3N_4 and SiO_2 capping dielectric layer is deposited using PECVD. It is patterned using EBL and a nickel layer is evaporated onto the wafer to form a hard mask for the subsequent reactive ion etching (RIE). d) Both the nickel comprising the hard mask as well as the nickel nanowires are removed using nickel wet etch, forming hollow nanochannels in the Si3N4-SiO2 stack. The gold working electrode is exposed inside the nanochannels and can electrically probe the solution within. Figure 3 shows the detail of the cross section through one of five nanochannels, marked by the dashed line above.

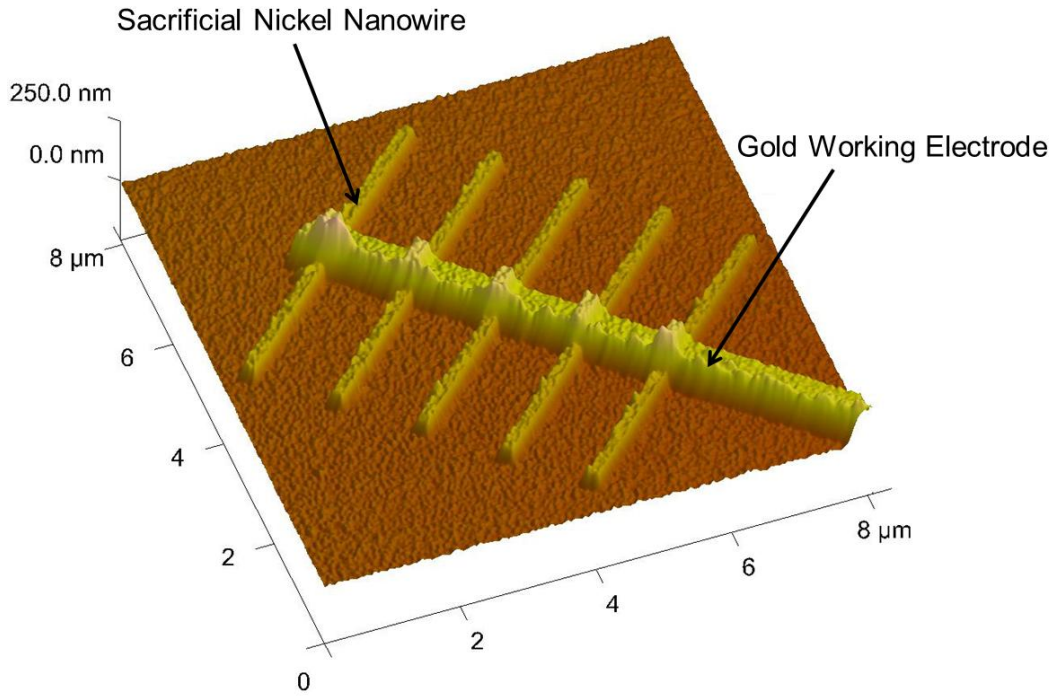

Figure 2. Atomic Force Microscope (AFM) image of 200 nm wide Ni nanowires and an Au working electrode prior to the deposition and patterning of the capping layer. The Ni structures are 60 nm tall and the Au electrode is 120 nm tall. The well-defined metal nanostructures are the result of static, vertical metal evaporation which reduces metal deposition on e-beam resist sidewalls.

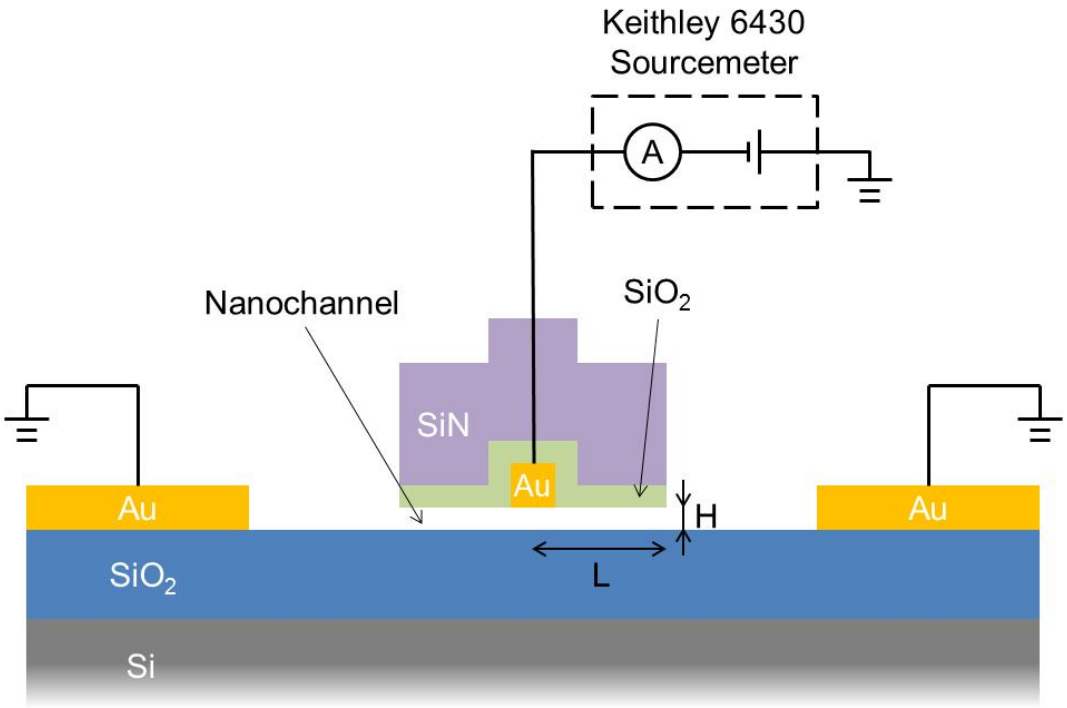

Figure 3. Nanochannel cross section (marked by dashed line in Figure 1d) showing electrical connections and electrode geometry. L defines the length of a single nanochannel, and H defines the height. Width of the nanochannel is defined as the dimension perpendicular to the page. Note that two nanochannels have a back to back connection.

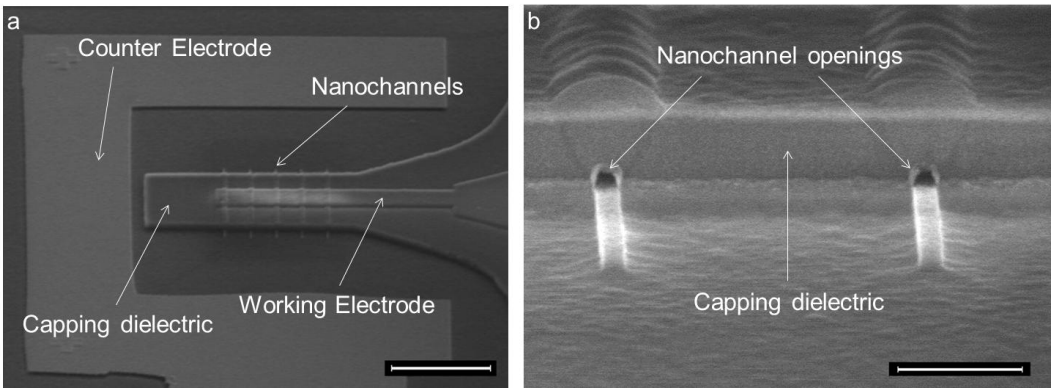

Figure 4 a) A tilted SEM view of the nanochannels, including the working and counter electrodes. The scale bar is 5 µm. b) A close up tilted SEM view of the nanochannel openings. Nanochannel opening dimensions are 60 nm by 60 nm. The scale bar is 500 nm.

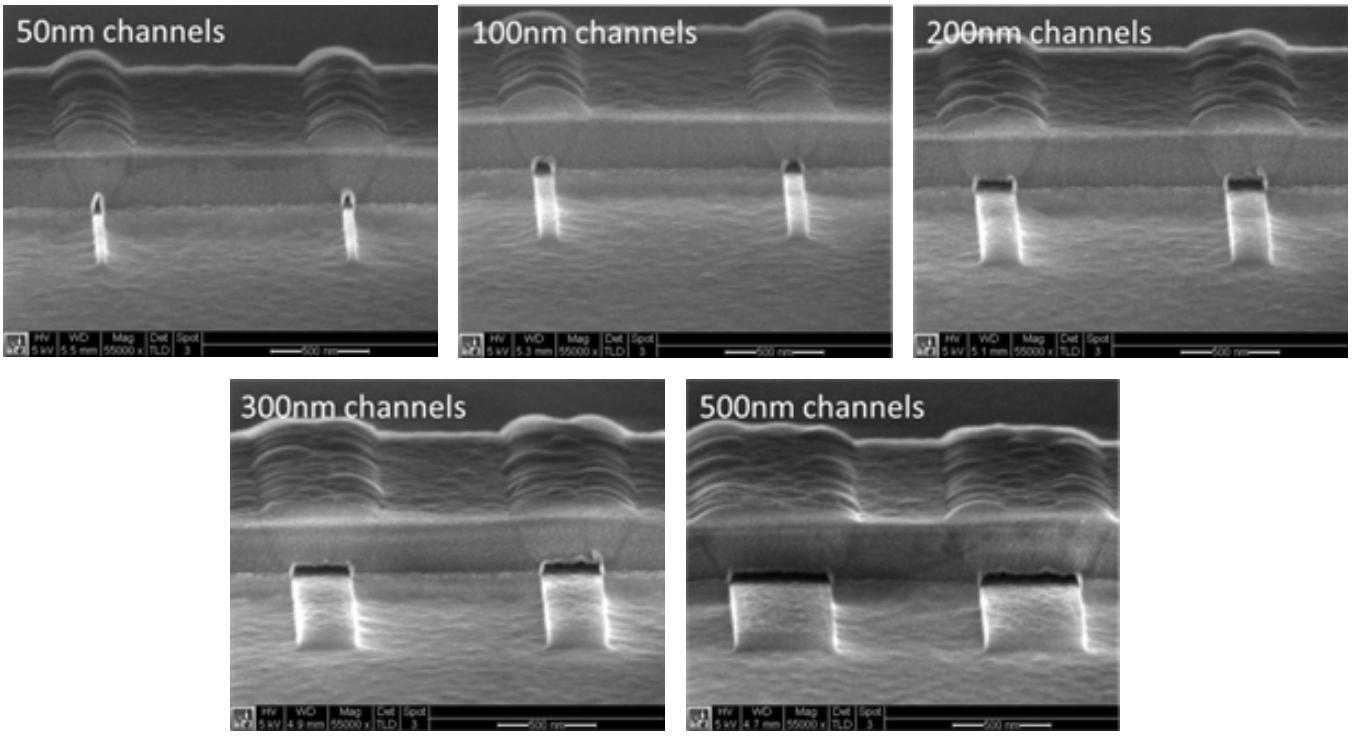

Figure 5 Tilted SEM views of various nanochannels. Width as marked, height is 60 nm.

2.1.2 Nanochannel Microfabrication

Nanochannels were fabricated by first depositing a 350 nm thick layer of silicon oxide onto a low conductivity silicon carrier wafer (100 orientation, ρ = 10 Ω-cm, 500 μm thickness, UltraSil) using plasma-enhanced chemical vapor deposition (PECVD). I then spun-coated a 75 nm thick layer of poly(methyl methacrylate) (PMMA) onto the wafer to use as electron beam resist. An electron beam lithography (EBL) system (JC Nabity NPGS; Bozeman, MT) was used to pattern sets of five 5 μm lines of various widths (60 nm to 500 nm, seen in Figure 5). I developed the nanoscale pattern by submerging the wafer into methyl isobutyl ketone (MIBK) and isopropyl alcohol (IPA) (1:3 v/v) solution and agitating for 70 seconds.

A 60 nm nickel layer was thermally evaporated using an electron beam evaporation system onto the wafer and metal lift-off was performed in acetone to form nickel nanowires on the wafer surface. During the nickel deposition I immobilized the wafer directly above the nickel source in

order to prevent metal coating on the sidewalls of the electron beam resist lines. Doing so resulted in perfectly rectangular nickel nanowires being formed (Figure 2).

I spun-coated a 500 nm layer of PMMA onto the wafer and performed a second EBL step to pattern the working and counter electrodes. The pattern consisted of a 5 μm wide horseshoe-like shape surrounding the nickel nanowires at 5 μm distance and a 500 nm wide line bisecting the nanowires. Both of these structures were then connected via 30 μm wide by 2 mm long lines to 200 μm squares (squares not shown in diagram). The wafer was then developed using the recipe described above.

I thermally evaporated a 120 nm gold layer with a 0.5 nm chromium adhesion layer onto a wafer, again immobilized directly over the gold source to prevent the metal from depositing onto the electron beam resist sidewalls. The sub-1-nm chromium layer was used in order to deposit a discontinuous metal layer, which, while acting as an adhesion layer, does not mask the bottom surface of the gold working electrode. After a metal lift-off in acetone the structure seen in Figure 1b was yielded. The working electrode crosses all five nanowires with the effective electrode area being the area of the gold line that is adjacent to the nanowire surface. The working electrode area varies between 0.09 μm^2 and 0.31 μm^2 for 60 nm and 500 nm wide nanowires, respectively. The counter electrode encircles the nanowires and the working electrode and has a surface area of approximately 250 μm^2.

I deposited a 30 nm layer of silicon dioxide and a 300 nm layer of very low-stress silicon nitride using a 300 °C PECVD process onto the wafer, to form the capping dielectric layer. The dual SiO_2/Si_3N_4 dielectric stack was required in order to preserve the structural integrity of the capping layer. I discovered that using only a silicon dioxide capping layer results in stress fractures emanating from the nickel nanowires (Figure 6), causing catastrophic structural failure of the nanochannels during the measurement process. The thin silicon dioxide layer provides well defined

surface chemistry on the inner surface of the nanochannels, and the silicon nitride layer acts as structural reinforcement.

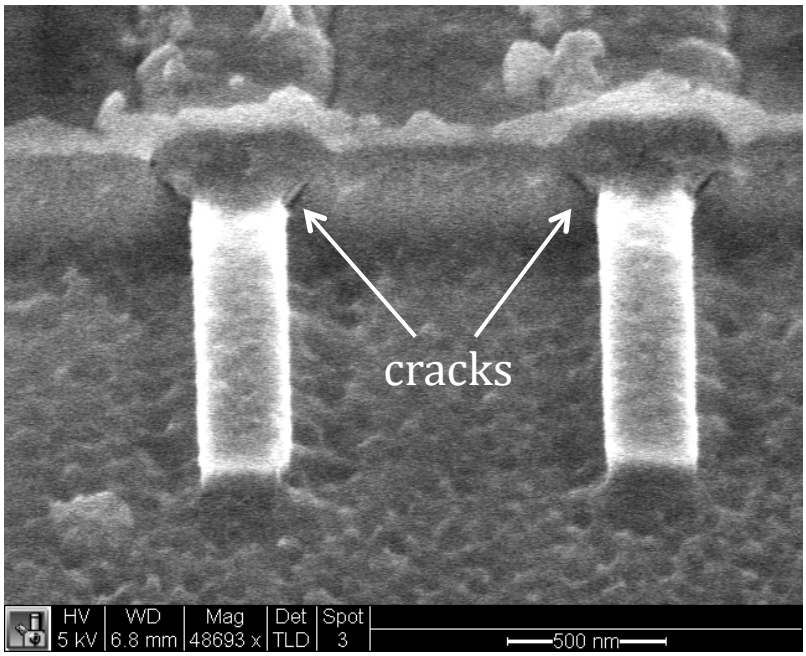

Figure 6 Cracks seen in the non-low stress oxide. Note that the nickel hard mask is still present and the nanochannels are still filled with Ni.

I spun-coated a 75 nm layer of PMMA onto the wafer and performed a third EBL step to pattern the dual dielectric stack. The pattern covered and extended 15 μm past the existing gold lines except at the 200 μm squares and the "horseshoe" structure of the counter electrode. While the working electrode was also fully covered by the pattern, the pattern left unexposed approximately 0.25 μm on either end of the nickel nanowires. I then developed the pattern and sputtered 25 nm of nickel onto the wafer. Sputtering was used instead of evaporation in order to uniformly coat the highly uneven topography of the areas exposed by the last EBL step. I then performed metal lift-off in acetone, and used reactive ion etch (RIE) with SF_6 to etch through the silicon nitride and a mix of CHF_3 and O_2 gases to etch through the silicon oxide of the dielectric

stack. The sputtered nickel layer acted as a hard mask for the RIE. The resulting structure can be seen in Figure 1c.

Lastly, the wafer was submerged into nickel etchant solution (Nickel Etchant TFB; Transene, Davers, MA) for 72 hours. The exposed nickel nanowire ends allowed the nickel etchant to fully etch out the nanowires (Figure 7), forming nanochannels in the capping dielectric layer. The gold working electrode inside the nanochannel is left intact due to the high etch selectivity of the nickel etchant. The nickel layer used as the hard mask for the RIE was also etched away during the process, resulting in the final structure seen in Figure 1d, Figure 3 and Figure 4.

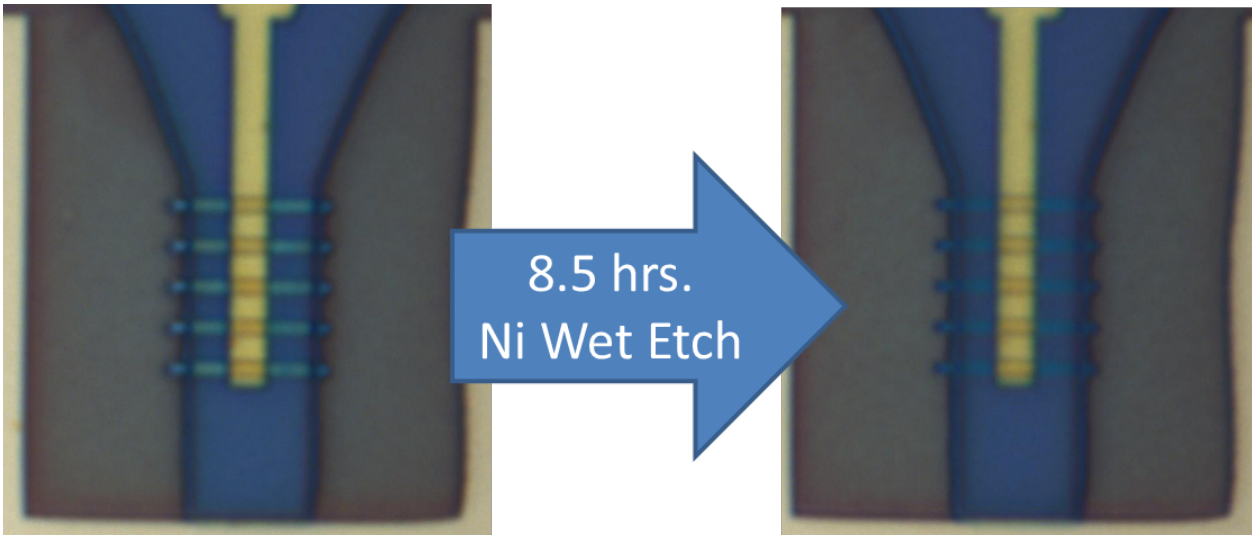

Figure 7 Effect of wet etching of sacrificial nickel nanowires can be observed via an optical microscope. Note the darker channels in the post-etch photograph, indicating an absence of nickel.

2.1.3 Nanochannel Testing

In order to sustain a DC current through the nanochannels we exploited the redox properties of ferricyanide and ferrocyanide ($Fe(CN)_6^{3-}$ and $Fe(CN)_6^{4-}$, respectively), which is a widely used redox couple in label-free electrochemical sensing arrangements. We mixed equal proportions of ferrocyanide and ferricyanide, to achieve 10 mM total concentration, a value based on available literature (Patolsky 1998, Zayats 2002) which provides optimal conditions for current

measurement and device stability. When a negative bias is applied to the working electrode, ferri(III)cyanide is reduced at the electrode, giving rise to a current signal.

$$Fe(CN)_6^{3-} + e^- \rightarrow Fe(CN)_6^{4-} \qquad (1)$$

The reduction reaction at the working electrode must be balanced by an oxidation process at the counter electrode. Ferro(II)cyanide was included in the solution in order to provide a facile route for an oxidation reaction at the counter electrode.

$$Fe(CN)_6^{4-} \rightarrow Fe(CN)_6^{3-} + e^- \qquad (2)$$

In the absence of ferrocyanide, significant pitting corrosion was observed at the counter electrode, possibly due to generation of chlorine gas as an oxidation product at the electrode. No evidence of pitting corrosion was observed after including ferrocyanide in the test solution. The redox couple was dissolved in pH 7.4 1x phosphate-buffered saline (PBS) consisting of 3.0 mM Na_2HPO_4, 155 mM NaCl and 1.1 mM KH_2PO_4 dissolved in deionized water. This was done in order to preserve neutral pH, provide a supporting electrolyte and simulate a biologically relevant environment. PBS has also played the role of shielding the nanochannel surface charge by making the positive potassium ion available as a counterion to the largely negatively charged silica sidewalls of the nanochannel. A potassium double layer is formed, its thickness given by the Debye length. At a given concentration of PBS, the Debye length is on the order of a few nanometers, effectively rendering the influence of nanochannel surface charge insignificant. (Karnik 2005; Stein 2004)

In order to remove possible air bubbles trapped inside the nanochannels prior to starting measurements, I briefly placed the liquid covered devices into a low pressure chamber evacuated using lab vacuum, forcing the bubbles out. The sensor was thoroughly flushed with PBS whenever a

replacement of the measurement solution was required and the bubble extraction procedure was performed again. A 5 mm thick piece of polydimethylsiloxane (PDMS) with a bored-out hole was then placed over the sensor, with the hole creating a well over the sensor and a watertight barrier between the well and the electrode pads. During electrical testing, liquid is introduced into the PDMS well and a glass cover slip is placed over the well opening to prevent liquid evaporation during measurements. The PDMS structure also insures that leakage currents are minimized by isolating any liquids away from the contact pads.

Electrical measurements were performed using a probe station (Lakeshore Cryotronics, Model TTP4) to contact the sensor's electrode pads. A bias of –0.5 V DC was applied on the working electrode, while measuring the current output using a Keithley 6430 Femtoammeter (Figure 3). The current would be monitored until all the transient current components disappeared. A stable current reading was recorded after 120 seconds of continuous application of an electrical potential. Repeatability of current measurements was verified by performing three replicate measurements. The devices were washed and the measuring solution was exchanged between measurements.

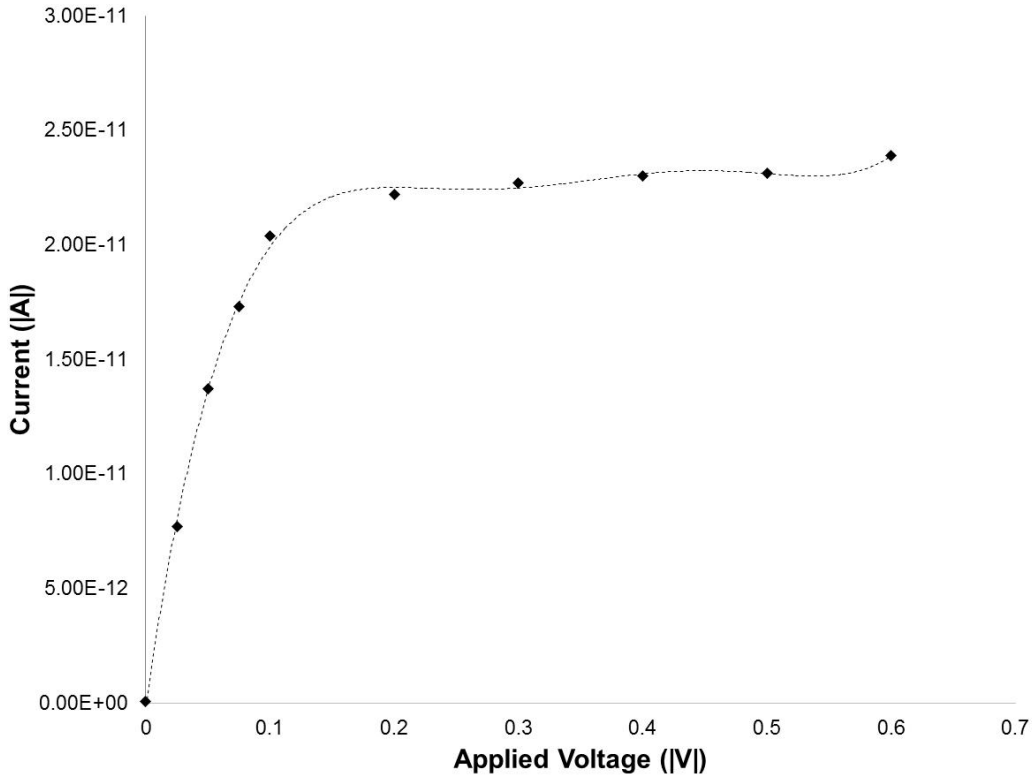

Figure 8 Measured nanochannel current vs. applied voltage. Voltages between 0 and –0.6V were applied to a device consisting of twelve 320 nm wide, 60 nm tall and 2.25 µm long channels. Current levels stabilize and become independent of applied voltage for potentials above –0.2V, indicating that the device is operating in diffusion-limited mode, with the $Fe(CN)_6^{3-}$ acting as a charge carrier.

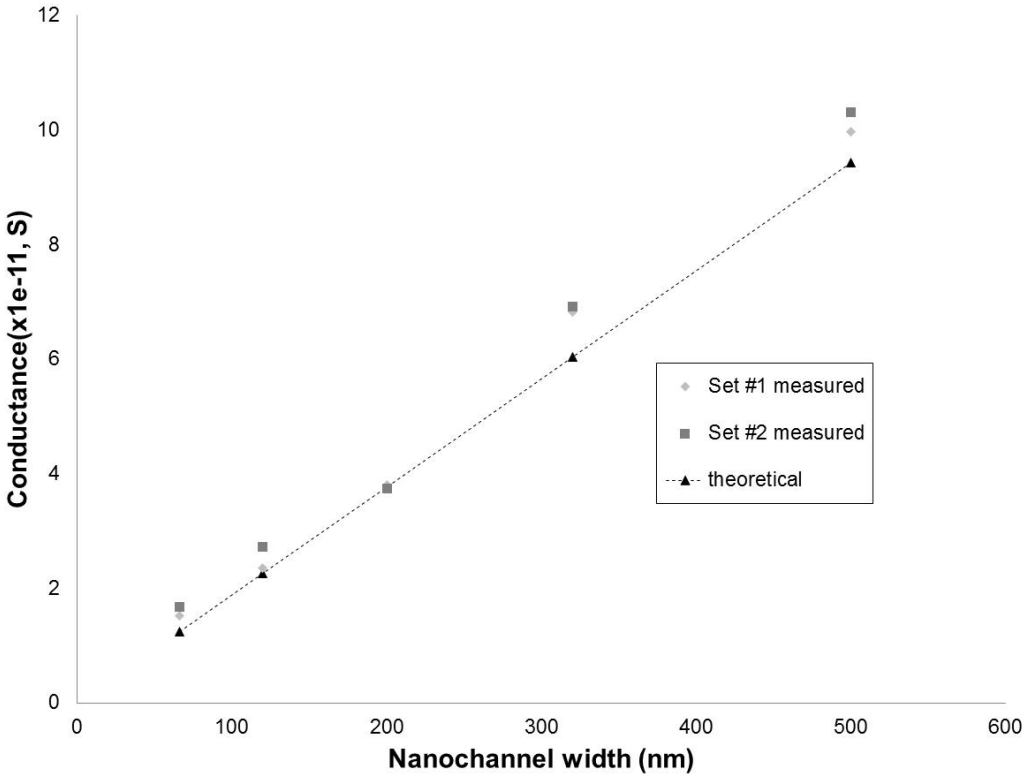

Figure 9 Measured nanochannel conductance vs. nanochannel width. Data from two sets of nanochannel devices. Dashed line represents the current as predicted by the diffusion current of $Fe(CN)_6^{3-}$. All measurements were taken at –0.5 V DC. Three measurements were averaged to produce current values indicated – the range of the measured values was within 3% of the mean for all nanochannel widths.

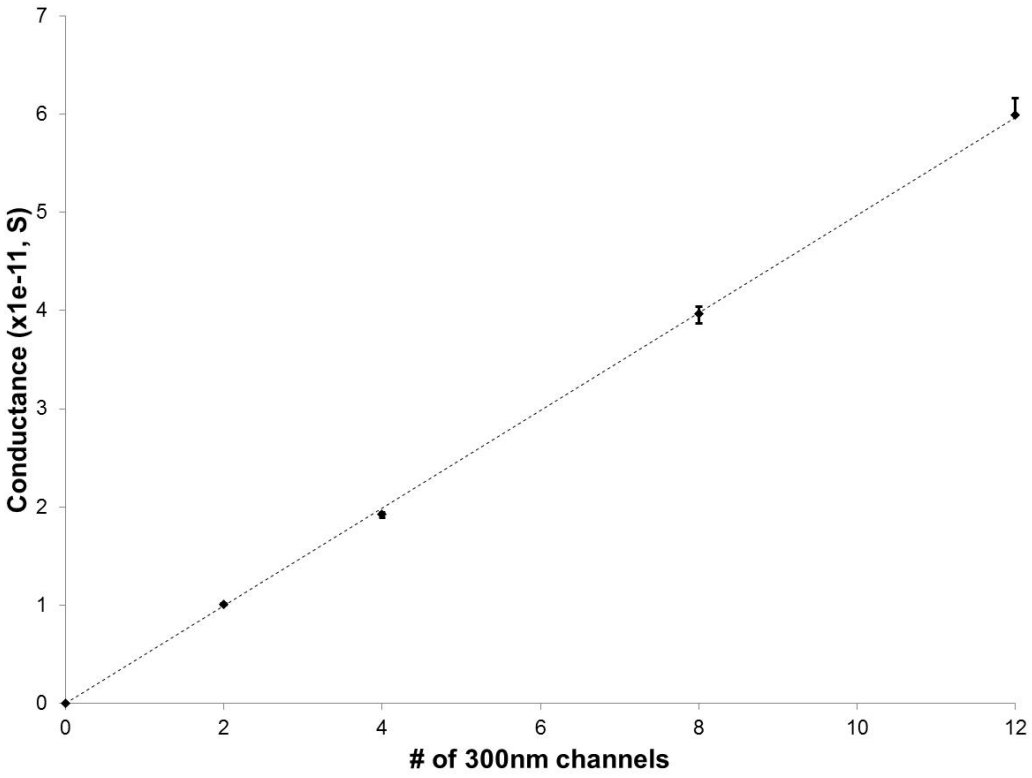

Figure 10 Measured nanochannel conductance vs. number of 300 nm wide nanochannels. All measurements were taken at –0.5 V DC. Three measurements were taken per current value indicated – the range of the values measured is indicated by the extent of the error bars.

The influence of applied voltage, as measured on the working electrode with respect to the counter electrode, on the observed current is shown in Figure 8. I incrementally increased the voltage, letting the resulting current settle for 120 seconds. I observed that the current levels off, becoming independent of the applied voltage at –200 mV, indicating that a diffusion limited reduction-oxidation reaction was taking place in the nanochannel. Selecting a measurement potential at –500 mV guaranteed a diffusion-dominated current that is insensitive to fluctuations in applied potential, instead being dependent only on the channel dimensions.

We characterized the conductance of the nanochannels with respect to the nanochannel width and quantity. Since both the length and height of the nanochannels are kept constant in our experiments, the channel width is directly proportional to the cross sectional area of the

nanochannel. The widths of the nanochannels in Figure 9 were distributed in such a way as to simulate a reduction in cross sectional area attributable to a 10 nm reduction in both the height and width of the nanochannel, as would be the case if a protein monolayer were to be placed on the nanochannel walls. As is evident from Figure 6, the observed current is linearly proportional to the channel width.

The conductance of the nanochannels can be modeled by the standard diffusion current equation (Daiguji 2004)

$$I_{diff} = NqeD\frac{nWH}{L} \qquad (3)$$

where N is the number of nanochannels (10), q is the number of charges provided by a single charge carrier (1), D is the diffusion constant (7.35×10^{-10} m^2/V s) (CRC Handbook 2011), n is the concentration of the redox species (5 mM) and W, L and H correspond to width (variable), length (2.25 μm) and height (60 nm) of the nanochannel, respectively.

I am making an assumption that the concentration of the redox couple varies linearly across the length of the nanochannel, starting at the bulk concentration (5 mM) at the entrance to the nanochannel and decreasing to zero at the electrode (Pletcher, 2001; Schoch 2008).

As seen in Figure 9, Equation 3 gives a reasonably accurate approximation for the diffusion current in the nanochannels.

Similarly, I observed an analogous change in conductance when characterizing devices with a varying number of nanochannels. A single 300 nm by 60 nm by 2.25 μm channel has a conductance of 5×10^{-12} S, and conductance is directly proportional to the number of such channels (Figure 10). Such a well-defined correlation with nanochannel size and quantity shows the

possibility of increasing the overall current signal by increasing either the number of nanochannels or their size.

Since the current signal shows strict dependence on channel dimensions, the nanochannel structure has potential to be used as a protein sensor. In order to confer selectivity to the sensor, the channel walls need to be coated with an antibody that has affinity to the protein of interest. Binding of the protein to the antibody would lead to channel constriction, which would be reflected as a decrease in observed redox current (Figure 12). Based on the characterization of the change in conductance with respect to channel constriction, a typical deposition of a 60% complete (Ihalainen 2001) monolayer of streptavidin (roughly a 5 nm diameter sphere – (Karnik 2005)) to the inner surface of a 60 nm by 60 nm nanochannel would decrease its cross section, and hence conductance, by approximately 15%.

2.1.4 Nanochannel Functionalization

In order to characterize the nanochannels' sensing potential we produced a device to create a streptavidin sensor, with the functionalization procedure described in Figure 11. The sensors were incubated in a solution containing 2% aminopropyldimethylethoxysilane (APDMES) in ethanol for 4 hours at room temperature, forming a covalently bound layer of APDMES molecules on all silicon oxide surfaces. Excess unbound molecules were washed away with an ethanol rinse, followed by a deionized water wash. The wafer, now containing a monolayer of covalently attached amine-ended molecules was immersed into a 0.5 mM solution of sulfosuccinimidyl-6-[biotinamido]-6-hexanamidohexanoate (sulfo-NHS-SS-biotin; Thermo Fisher Scientific, Rockford, Il) in pH 7.4, 10 mM phosphate buffer for 1 hour. Any unbound molecules were removed with a deionized water wash. The NHS reacts with the amine of the APDMES to covalently bind a biotin molecule to the surface. The 2.5 nm long spacer of the sulfo-NHS-SS-biotin is used to decrease steric hindrance during subsequent streptavidin binding. The sensors are then held in a solution of streptavidin (Thermo Fisher Scientific, Rockford, Il) dissolved in 1x PBS to a concentration of .2 to

2000 µg/mL for 30 minutes at room temperature during which the streptavidin molecules very strongly bind to the biotin coated nanochannel walls. A series of PBS and deionized water rinses was used in order to remove any unbound streptavidin molecules. Extra caution must be observed during the functionalization process to never allow the buffer solutions to evaporate. The resulting salt crystals embed themselves into the nanochannels, disabling the sensors.

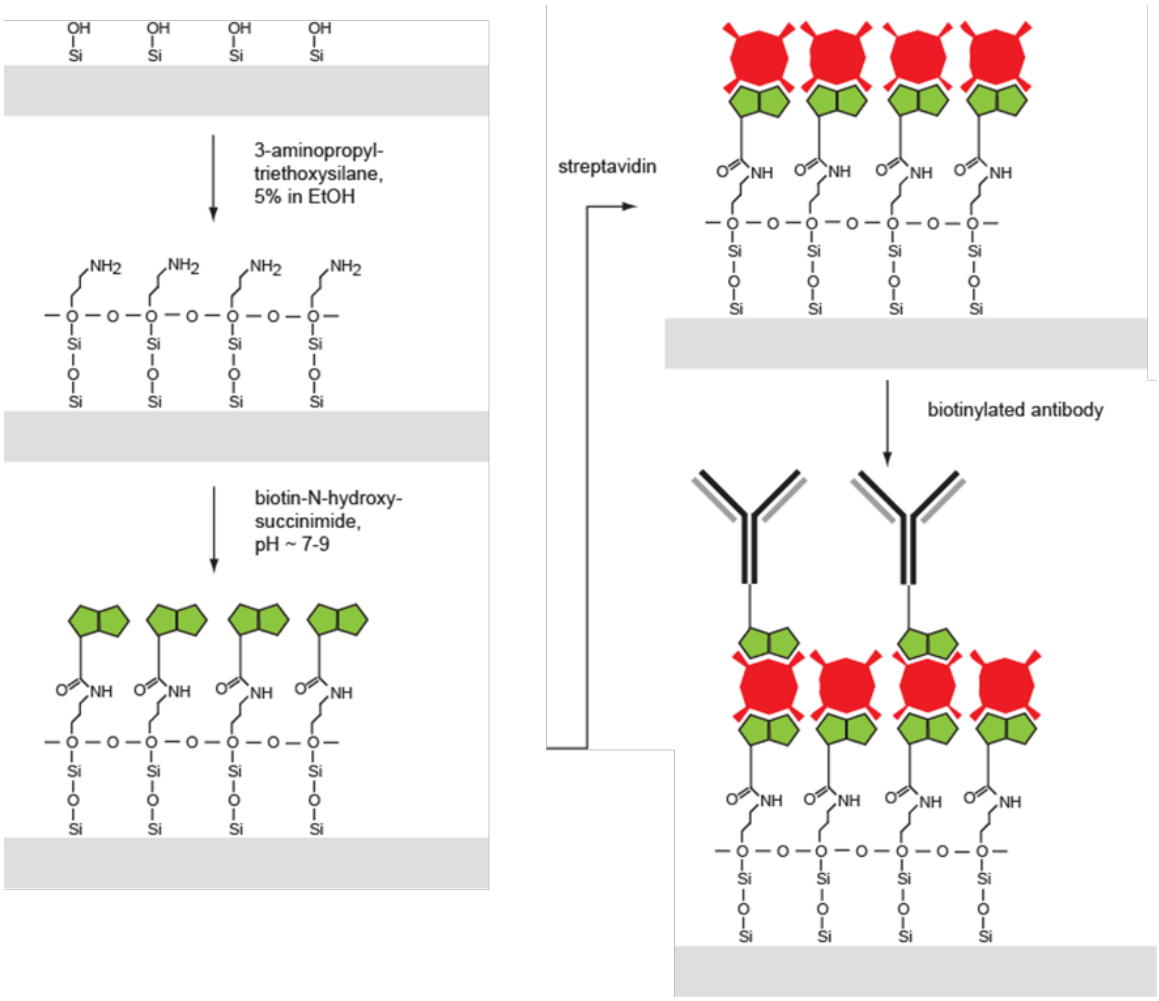

Figure 11. Nanochannel inner surface functionalization process.

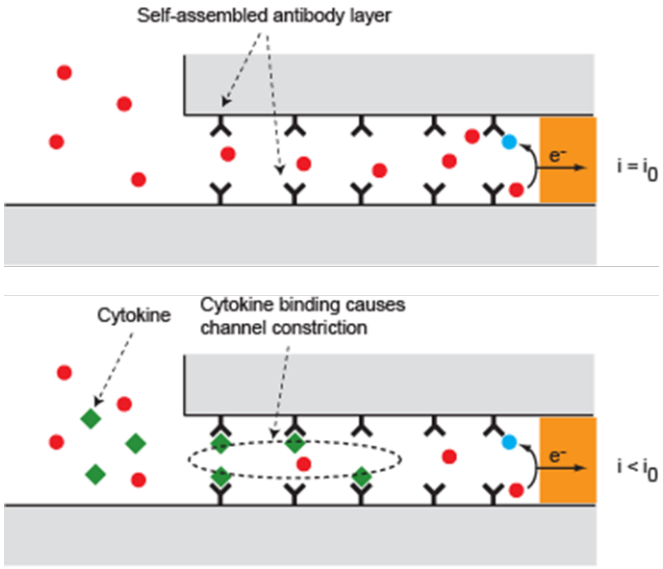

Figure 12. Nanochannel biosensor function diagram. Target molecule binding inside the nanochannel constricts the nanochannel, reducing the diffusion rate of the redox couple to the working electrode, thus decreasing the redox current of the device.

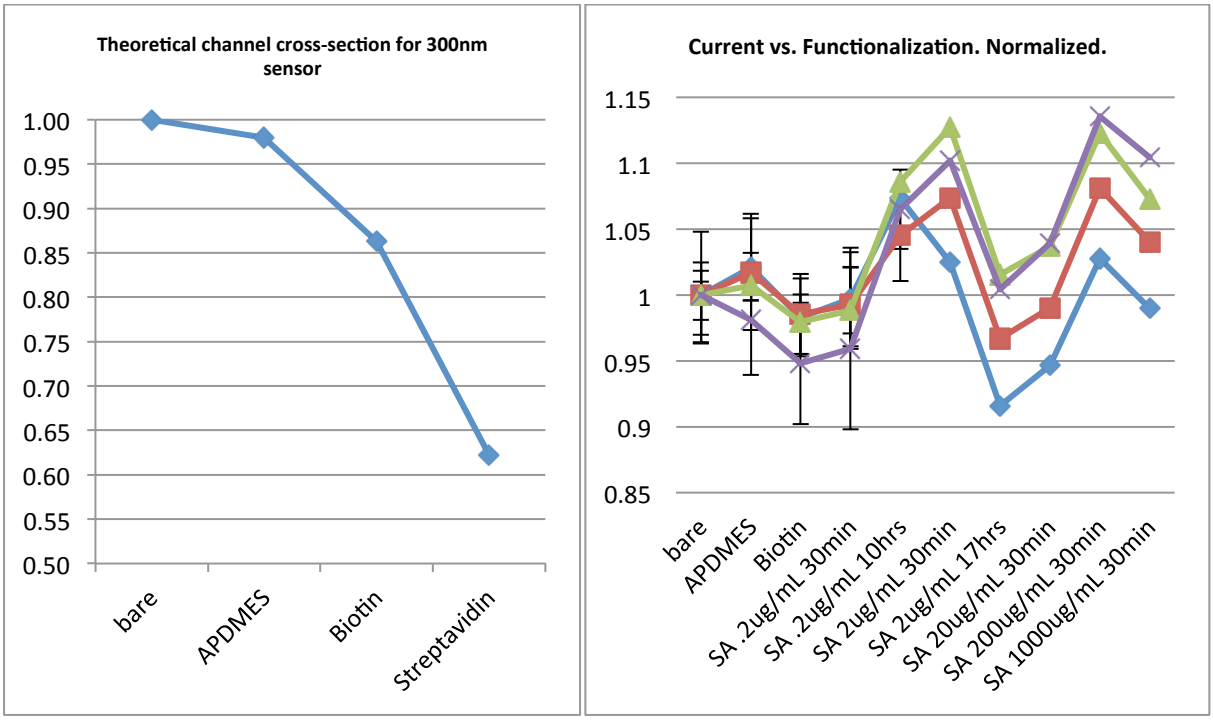

Figure 13. a) Theoretical normalized change in conductance of a 300 nm wide nanochannel sensor after each functionalization step. b) Measured nanochannel conductance normalized to conductance of an unfunctionalized device is plotted for four 300 nm wide nanochannel sensors, with respect to the functionalization step. A general decrease in conductance with addition of functionalization layers is noted, albeit not of significant enough magnitude.

In the characterization experiments of the functionalized sensors (Figure 13) I observed general trends that indicated successful sensing of streptavidin and biotin-SS-NHS immobilizations. However, much work remains in order to fully confirm the sensing functionality.

Had the sensor been viable, possible failure vectors have been considered, such as gold electrode fouling by biomolecules and electrode deterioration. I have discovered that gold electrode fouling can be reversed by hydrolyzing pure water inside the nanochannels, creating micro gas bubbles and thus mechanically clearing the electrode surfaces. Electrode deterioration can be controlled by adjusting the redox couple concentration levels.

2.1.5 Chemical Functionalization Verification

In order to verify that the chemical functionalization parameters are correct, a series of experiments were conducted using fluorescently marked streptavidin and verified using a light scanning microscope (LSM).

Silicon oxide coated silicon substrates were first functionalized with APDMES per the standard recipe described in the previous section. PDMS pieces with punched out cores were attached to the silicon chips and used as "wells" to contain the liquid reactants used in subsequent functionalization steps. As can be seen in Figure 14, three of the wells were then functionalized using sulfo-NHS-SS-biotin (10 mM for 1 hour) and three were left blank. After a thorough DI water rinse, the PDMS wells were shifted by a well radius. This exposed an area of the substrate that was not functionalized with biotin. Then, three different concentrations of fluorescently labeled streptavidin-Alexa488 (10, 5 and 1 μL in 1x PBS; streptavidin, Alexa Fluor® 488 conjugate, Invitrogen) were injected into the wells and allowed to react with the substrate for 30 minutes. The PDMS wells were then removed, substrates were washed in DI water, thoroughly dried, and analyzed using the LSM.

As can be most easily observed from the upper-middle panel in Figure 14, four different functionalization combinations are present in the sample: 'A' – only APDMES, 'A,B' – APDMES and

biotin, 'A,S' – APDMES and streptavidin-Alexa488, and 'A,B,S' – APDMES, biotin and streptavidin-Alexa488. The experiment verified, qualitatively, the preferential deposition of streptavidin onto biotinilated surfaces, demonstrating that both the APDMES coating and biotinilation steps, as well as, the streptavidin-biotin binding have occurred successfully. Furthermore, it was shown that using a streptavidin concentration of more than 5 μg/mL did not result in a more complete coating – rather, the biotin binding sites were saturated at the above concentration.

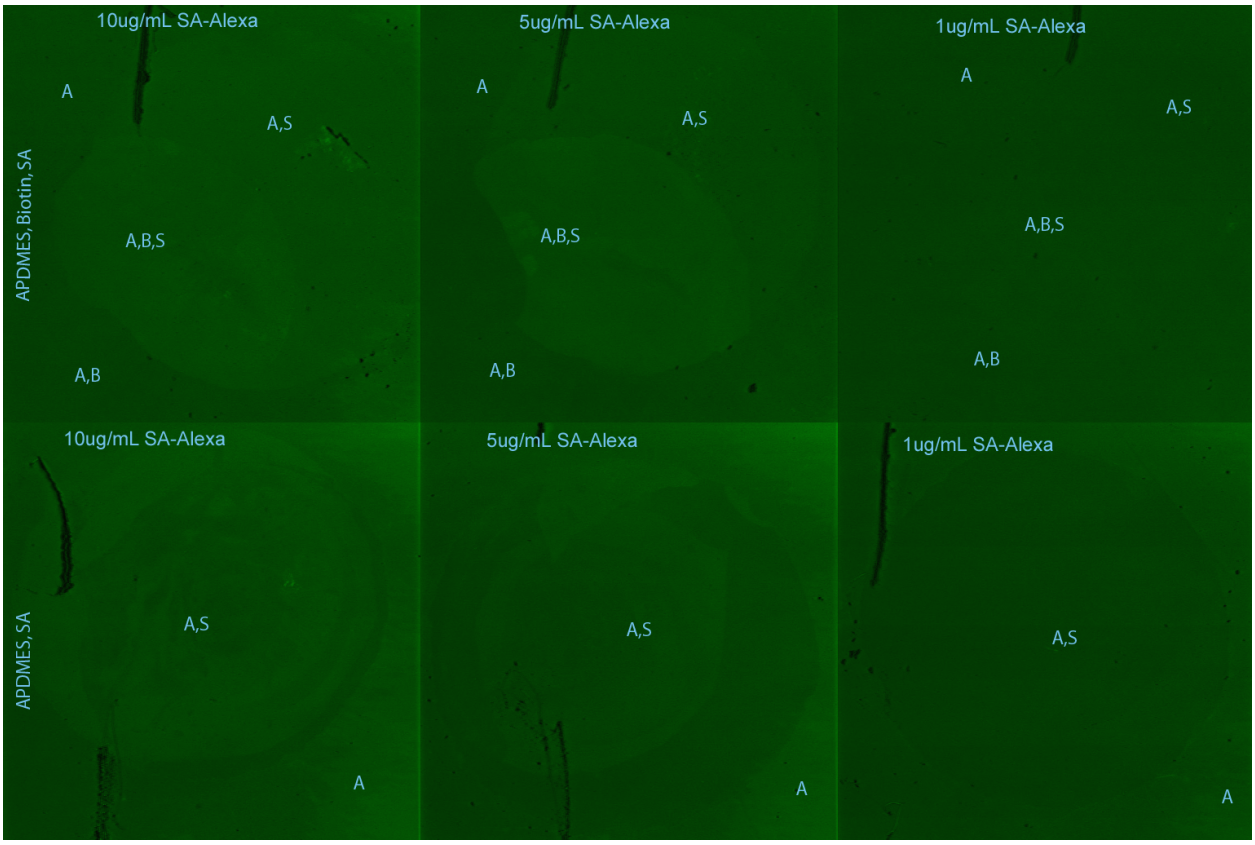

Figure 14 Light Scanning Microscope images demonstrating the effectiveness of the APDMES-Biotin-Streptavidin functionalization on silicon oxide surfaces. Areas marked 'A' are functionalized with APDMES, 'B' - biotin-NHS, 'S' - streptavidin-Alexa488. Multiple depositions are demarcated with commas – with the deposition sequence left-to-right.

However, the question remains as to why we haven't been able to observe similarly effective functionalization inside the sensor nanochannels. Two failure modes are proposed. First, one must recognize the difference in the chemical conditions present inside a constrained space of the nanochannel. The effectiveness of both the biotinilation and the antibody coating steps are greatly

influenced by the pH of the solution in which the reaction is allowed to happen. One cannot simply assume that the pH of the liquid inside the nanochannel is the same as that in the bulk. Second, the diffusion dynamics of nanoscale objects must be considered. Although I have allowed in some experiments for the streptavidin functionalization step to run for as long as 24 hours at concentrations as high as 2000 μg/mL, perhaps a much longer time is required in order for a sufficiently large number of streptavidin molecules to diffuse into the 60 nm tall channel opening and attach to the channel walls.

2.1.6 Nanochannel Sensor Conclusions

We have fabricated and characterized sets of nanochannels which show great potential as a biomolecule sensor platform. The relatively simple nanochannel design allows for precise control of two nanoscale dimensions – the height and width of the nanochannels. This enables us to optimize the size of the nanochannels for both the overall conductance, as well as the biomolecule detection sensitivity. By using a redox couple-mediated conduction scheme, I have shown that the nanochannel conductance is directly proportional to both the nanochannel cross section and the number of nanochannels. Furthermore, the robust redox transduction scheme allows the nanochannel conductance to be significantly larger in order to minimize electronic noise concerns. Using a separate redox couple also lets us predict nanochannel performance using the standard diffusion current equation.

Given the conductance characteristics of the nanochannels, it should be possible to build a biomolecule sensor by immobilizing antibodies on the inner surfaces of the nanochannels. When exposed to a solution containing the respective antigen – the antigens bind to the antibodies, effectively constricting the nanochannel cross section, which, in turn, decreases the channel conductance. We can exploit the fact that the diameter of many biomolecules is similar in size to the inner dimensions of the nanochannel, thus allowing us to couple an alteration of a physical characteristic of the nanochannel to a purely electronic quantity. Immobilization of a layer of

proteins with a diameter of 5 nm will decrease the cross sectional area of the 60 nm nanochannel, and thus the conductance, by 15% making such a device potentially a very sensitive biomolecular sensor. However, it can be challenging to assemble the necessary biomolecular acceptors on the inner surface of the nanochannels, requiring significant future effort in order to realize such a sensor.

The nanochannel fabrication process is compatible with standard CMOS processing, which allows for the creation of large arrays of sensors interconnected using multiplexing circuitry. By selectively functionalizing the nanochannels with various biomolecular receptors, a highly versatile sensing platform can be created. Furthermore, individual nanochannel conductance can be controlled by applying a gating voltage to the outer insulating oxide layer (Daiguji 2004). The inherent sensitivity and the fact that the charge transfer is provided by a separate redox molecule, and not the molecule whose concentration is being measured, makes the sensor ideal for very low concentration measurements such as those in single cell biology.

2.2 Nanowire Sensors

A promising biomolecule detection approach investigated in recent years is a selective, sensitive, purely electronic sensor platform utilizing semiconducting nanowires coated with various biomolecule receptors as the sensor element. (Cui, 2001; Lund, 2006, Li, 2004; Wang 2005) Such a device does not require labeling of the target molecules, thus eliminating the need for bulky fluorescent detection and flow cytometry equipment, instead, sensor output is interfaced directly with measurement electronics. Semiconducting nanowires and supporting circuitry take up a very small space, and can be fabricated using standard semiconductor processing techniques, utilizing widely available equipment.

Described below is the fabrication and characterization of a nanoscale sensor platform made of single crystal silicon that can be adapted for electronic detection of various biomolecular targets, as well as solution pH. The sensor offers a number of potential advantages: a) its fabrication

process allows for direct integration with silicon interface circuits and thus allows us to precisely control the size, location and orientation of the nanowire devices, b) its small footprint (~ 1 μm^2) allows for placement of multiple sensors within a very small area c) its transduction mechanism directly generates an electronic signal hence simplifying signal conversion and manipulation, and d) it can be easily modified, by changing the receptor molecules to detect different targets.

Specifically, a method that can be used to measure levels of cytokine IL-1β is laid out below. Deciphering the conversations of the immune system hinges upon capturing a snapshot of the cytokines that cells secrete and receive. Cytokines are usually secreted in response to a pathogen and the need for triggering and mounting a defense, or causing inflammation in response to bodily damage. Itemizing the cytokines that cells secrete and receive is crucial to better understanding disease development and the body's response.

2.2.1 Nanowire Device Design Overview

The main component of the biosensor is a nanoscale silicon wire with a surface functionalized with receptor molecules. Upon exposure, target molecules bind to these receptors and effectively change the surface dipole moment of the nanowire. This change of dipole moment, in turn, affects the charge carrier density at the nanowire surface. Due to the extremely small cross section of the conductive path (100 nm x 200 nm), changes close to the surface significantly affect the apparent conduction in the nanowire and can be monitored electronically to determine the occurrence of molecular binding events.

2.2.2 Microfabrication

To fabricate the sensors I used a silicon-on-insulator (SOI) wafer as the substrate. I used electron beam lithography to pattern 200 nm-wide and 5 μm-long nanowires with tapered leads connected to 200 μm square contacts. Evaporation of 25 nm of chromium and lift-off defined a masking layer that we used for etching the 100 nm thick top silicon layer down to the buried oxide (BOX) layer with RIE. We then removed the chromium layer with wet etching, and used two

subsequent e-beam lithography steps to define the chromium-platinum contacts and a 500 nm thick PMMA passivation layer (only allowing for exposure of the nanowire to the test solution). The final sensor structure is shown in Figure 15. The sensor structure allows for direct conversion of molecular recognition and binding events to electronic signals. This sensor offers a number of advantages: a) its fabrication process allows for direct integration with CMOS, b) its small footprint ($\sim 1\ \mu m^2$) allows for placement of multiple sensors within an area covered by a typical mammalian cell (example: macrophage), c) its transduction mechanism directly generates an electronic signal hence simplifying signal conversion and manipulation, and d) it can be easily modified, by changing the receptor molecules to detect different targets.

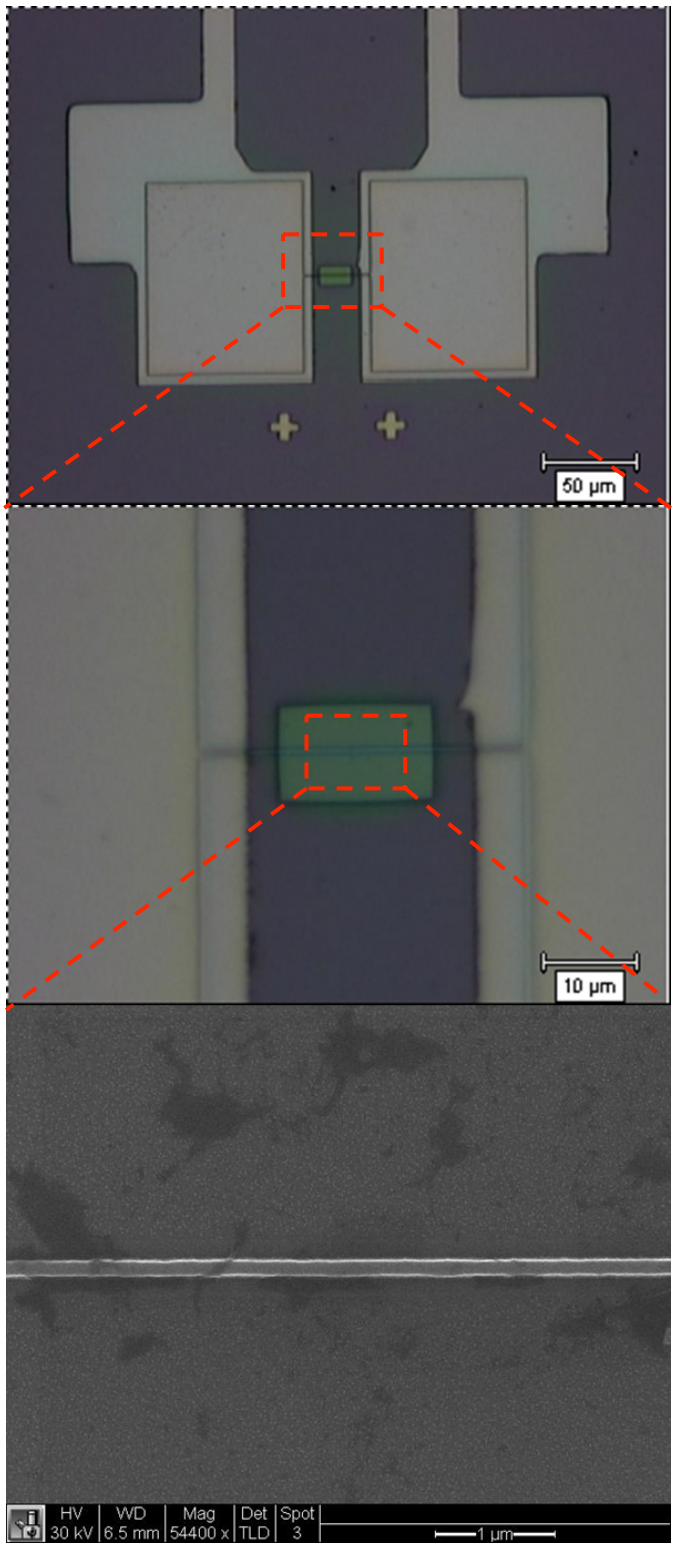

Figure 15 Nanowire device at various magnifications. Width of the nanowire in the final SEM micrograph is 100 nm.

2.2.3 Nanowire Testing

The electrical properties of the nanowire were tested using a standard transistor 3-electrode setup, illustrated in Figure 16. Gating effect was achieved by contacting the back side of the wafer via an aluminum foil extender, and the nanowire was accessed via platinum contact pads on the top side of the device.

Device behavior was that of an n-channel MOSFET. As one can see from Figure 17, Ids vs. Vds behavior for a 78 nm wide, 50 nm tall and 5 μm long contains all the features of a standard MOSFET. Vth for this particular device was estimated at 9.75 V. Other nanowire devices on the same wafer exhibited analogous behavior. Figure 18a illustrates the relationship between nanowire width and its conductance. Predictably, conductance increases with increasing nanowire size, both because of a larger cross-sectional area, but also because of a decreased surface area to volume ratio (Zheng, 2005). The lower the ratio, the more control the back gate has of the conductive channel, diminishing the influence of nanowire surface charges (Elfstrom, 2007). The same trend is also observed in Figure 18b where decreasing nanowire width strongly correlates to a higher Vth.

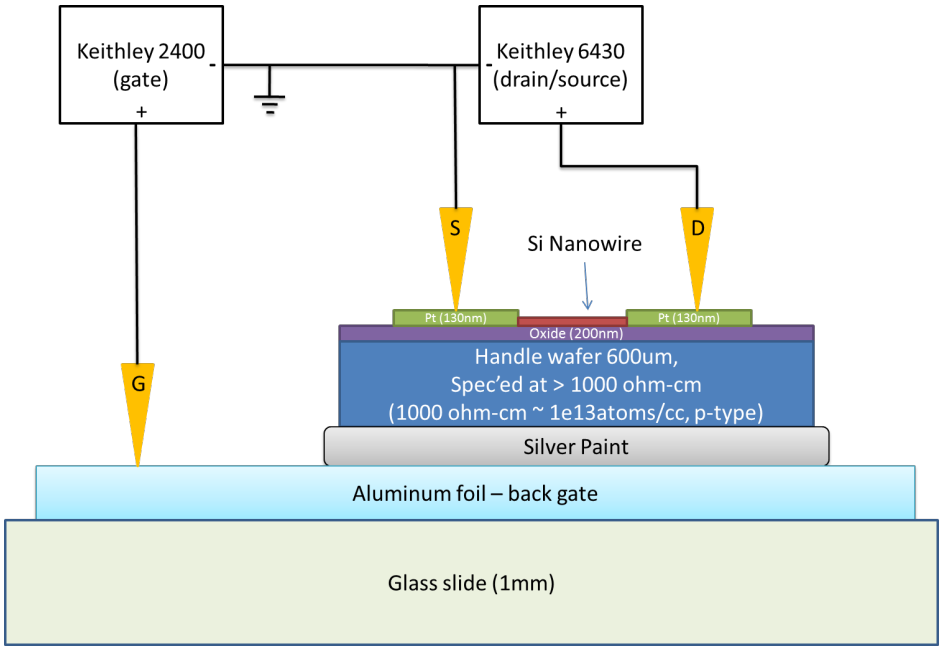

Figure 16. Measurement setup diagram for nanowire testing.

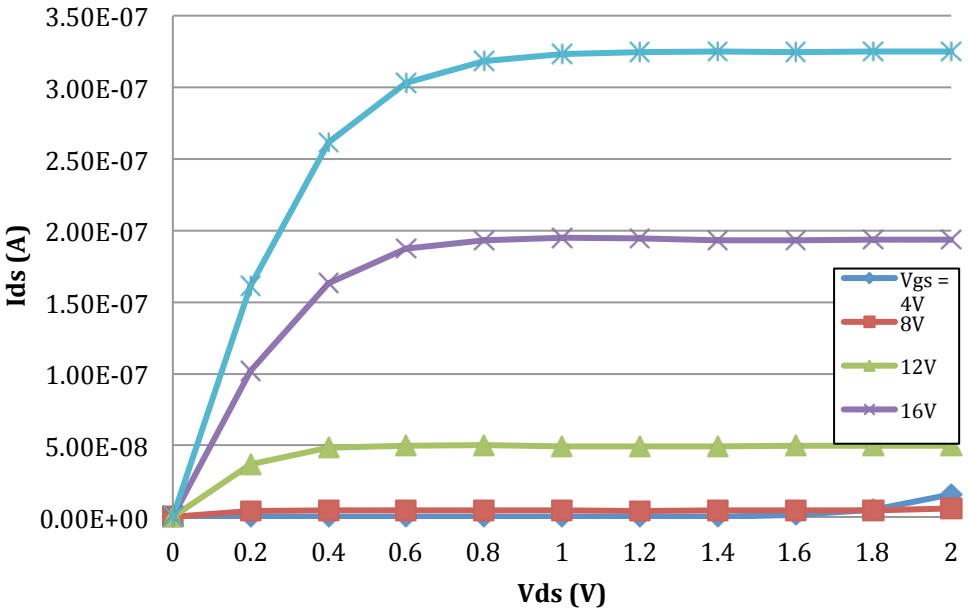

Figure 17. Ids vs. Vds plot at various Vgs for a 78 nm wide, 5 micron long nanowire. Vgs is applied via backgate.

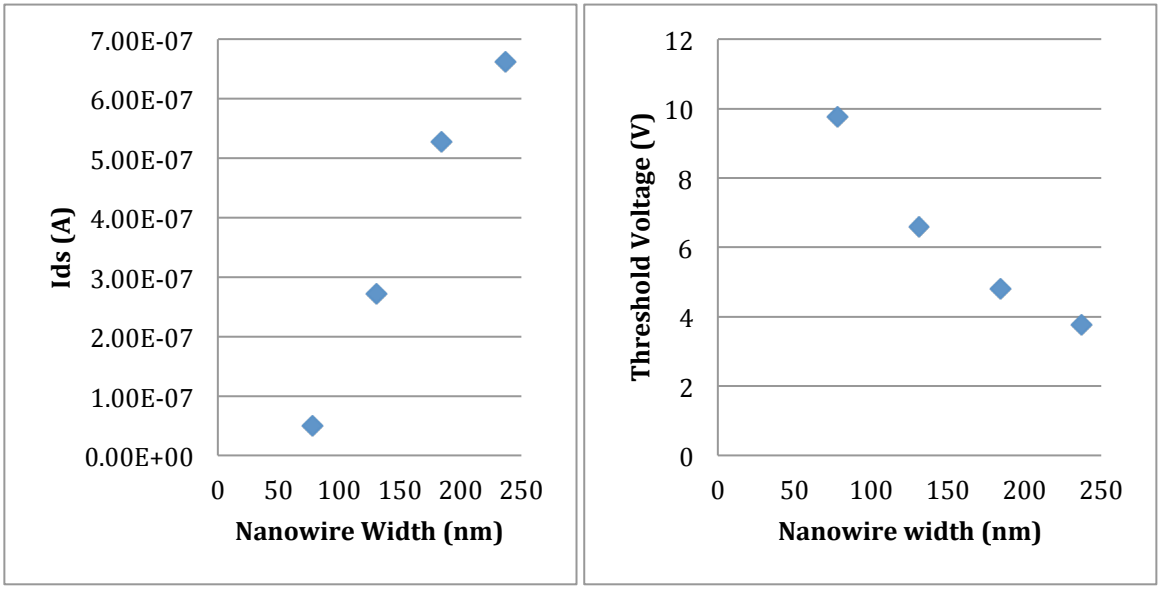

Figure 18. a) Ids vs. nanowire width measured at Vgs=12V and Vds = 1V (saturated device). b) Vth vs nanowire width. Increasing Vth with decreasing nanowire width as expected – surface charges exhibit a larger degree of control over the conduction channel as the surface area to volume ratio increases.

2.2.4 Nanowire Functionalization

The sensor surface was functionalized by receptor molecules to detect the cytokine, interleukin-1β (IL-1β) (Figure 19.) As a first step the sensor was incubated for 2 hours in biotinamidocapropyl-labeled bovine serum albumin (BAC-BSA) solution (5 μM in 1 mM phosphate buffer with 5mM NaCl, pH 5.6). BSA readily binds to the surface of the nanowire and makes biotin groups available for further binding. The attachment of BAC-BSA changes the apparent conductivity of the structure. This was followed by incubating the BSA functionalized sensors in streptavidin (5 μM in 1:10 diluted phosphate buffered saline, pH 7.4) and measuring the change in conductance due to biotin-streptavidin interactions. Next, the biotin conjugated anti-mouse IL-1β (5 μM in 1:10 diluted phosphate buffered saline, pH 7.4) is attached to the streptavidin, owing to the presence of four binding sites in the streptavidin molecule. Finally, this biomolecular stack is employed for the detection of mouse IL-1β (5 μM 1:10 diluted phosphate buffered saline, pH 7.4.) After each step, the device was washed 5 times with the same buffer as used in the solution to remove the excess unbound bio-molecules present on it.

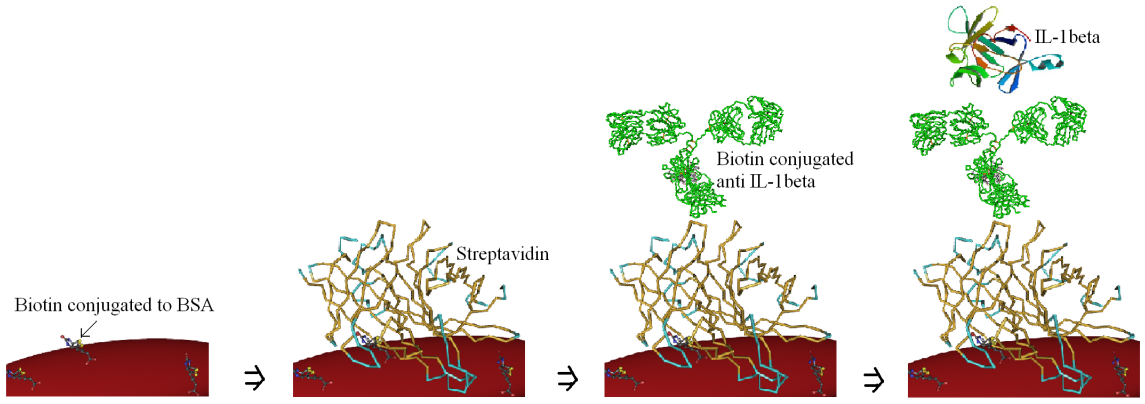

Figure 19 Nanowire functionalization procedure.

2.2.5 Nanowire Conclusions

Although significant effort went into attempting to detect the presence of IL-1β, the sensor was plagued with current leakage problems when it came into contact with liquids. The problem was narrowed down to a leaky PMMA and the fact that the BOX layer deteriorated during the measurements and resulted in unacceptable current leakage to the gate electrode. These problems can be overcome with use of more sophisticated SOI substrates which have a more robust insulating layer. Also, it appears that PMMA is not the ideal choice of material for liquid insulation, perhaps use of a negative photoresist such as SU-8 could improve the device performance.

3 Ocular Contact Lens Based Glucose Sensing

Tear fluid presents an abundance of molecular targets that can provide valuable information about the well-being of a patient (Tapaszto, 1973; van Haeringen, 1981). In particular, continuous monitoring of specific biomarkers can be especially effective in early detection of various cancers (Grus, 2007; Evans, 2011), early warning of stroke occurrence based on lactate measurements (Cvoro, 2009), and constant monitoring of glucose levels in diabetic patients (March, 2004).

Below is a summary of my work relating to the intraocular glucose sensor implant. Due to an increasing incidence of diabetes in the Western world, there comes a need for a more effective method of monitoring blood glucose levels. While the blood draw method has been accepted as a reliable standard, it is neither convenient, nor does it allow for continuous monitoring of glucose which would allow diabetic patients to more effectively control the negative symptoms of the disease.

It has been shown that glucose levels in tear fluid closely reflect the glucose levels found in blood (Baca, 2007). As an example, our group has designed and fabricated a non-invasive amperometric glucose sensor on a contact lens to take advantage of that property (Yao, 2010).

In vitro testing of the intraocular glucose sensor was performed by suspending the sensor inside a stirred buffered saline solution which mimicked physiological pH conditions. Known quantities of glucose were then added to the saline in order to progressively increase the glucose concentration. Ascorbic acid, lactate and urea were also added to the solution as interference agents as an attempt to more closely approximate the chemical makeup of the tear fluid. The sensor showed good interference rejection to these three species.

In vivo glucose detection, however, is complicated by a much more complex environment for sensing. Aside from the three interference agents used in in-vitro testing, the complex makeup of tear fluid may contain other chemicals that can negatively affect the measurement quality. Also, eyelid motion creates a turbulent and unpredictable fluid environment that may be detrimental to the both the sensor structure, and the stability of the signal. In order to verify the functionality and the reliability of the sensor on the eye surface I created a polymer mechanical eye model that more closely reproduces the chemical composition, mechanical characteristics and geometric features of a human eye than any other existing model (Millar, 2002). Also described is in-vivo testing of a miniaturized glucose sensor that uses intraocular fluid as an imitation for tear fluid.

3.1 Intraocular glucose sensor fabrication and in-vivo testing

The glucose sensor is comprised of four metal electrodes fabricated on a 100 μm thick layer of transparent polyethylene terephthalate (PET) using standard microfabrication techniques. PET is then cut into 5.5 mm by 2.5 mm rounded rectangles, seen in the left panel of Figure 20. One of the electrodes is then covered by a titanium sol-gel containing embedded glucose oxidase (GOD) enzyme. The covered electrode acts as the working electrode (WE1) in a typical three-electrode electrochemical cell setup, with the other three electrodes serving as the reference (RE) and counter (CE) electrodes, as well as a second, bare working electrode (WE2).

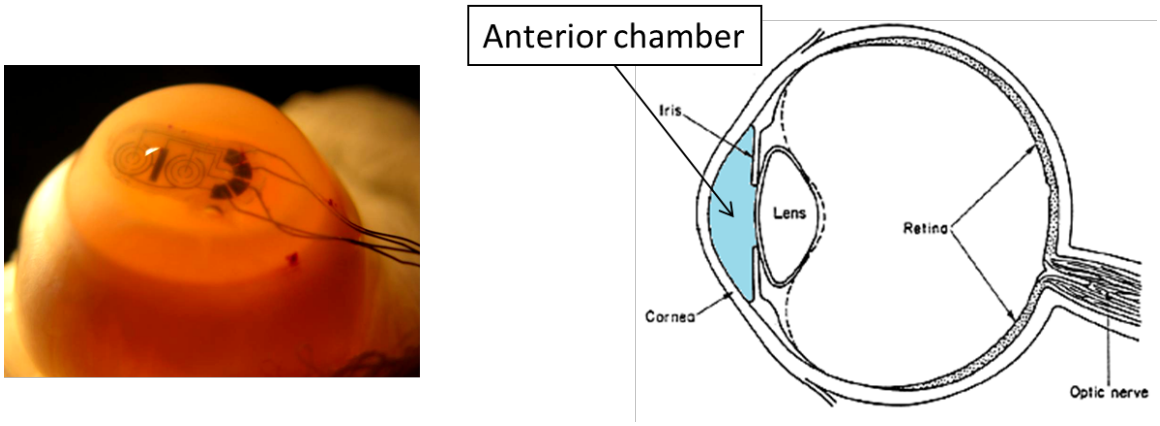

Figure 20. Testing the intraocular glucose sensor in a rabbit's eye. The sensor was inserted into the anterior chamber of the eye, highlighted in the right panel.

Glucose molecules diffusing through the sol-gel undergo an enzymatic reaction and produce hydrogen peroxide, per Eq. (4), which, in turn, undergoes a redox reaction at the working electrode, producing a measureable current, per Eq. (5). An external potentiostat was used in order to perform the amperometric measurements in a glucose containing solution, interfacing with the sensor via leads, soldered to the contact pads seen in Figure 19. The sensor proved to be very effective at detecting glucose concentrations in the range found in human tear fluid – between 0.1 mM and 0.6 mM, Fig 20.

$$D\text{-}glucose + O_2 \rightarrow H_2O_2 + D\text{-}gluconalactone \qquad (4)$$

$$H_2O_2 \rightarrow 2H^+ + O_2 + 2e^- \qquad (5)$$

We performed a differential current measurement, using the second working electrode which is not treated with GOD containing sol-gel to measure the signal resulting from the interfering species in the solution. Thus, subtracting the signal measured on the untreated working electrode from the signal measured on the one that contains GOD, results in a current signal attributable solely to the presence of glucose in solution, virtually eliminating the influence of the interfering species (Figure 21).

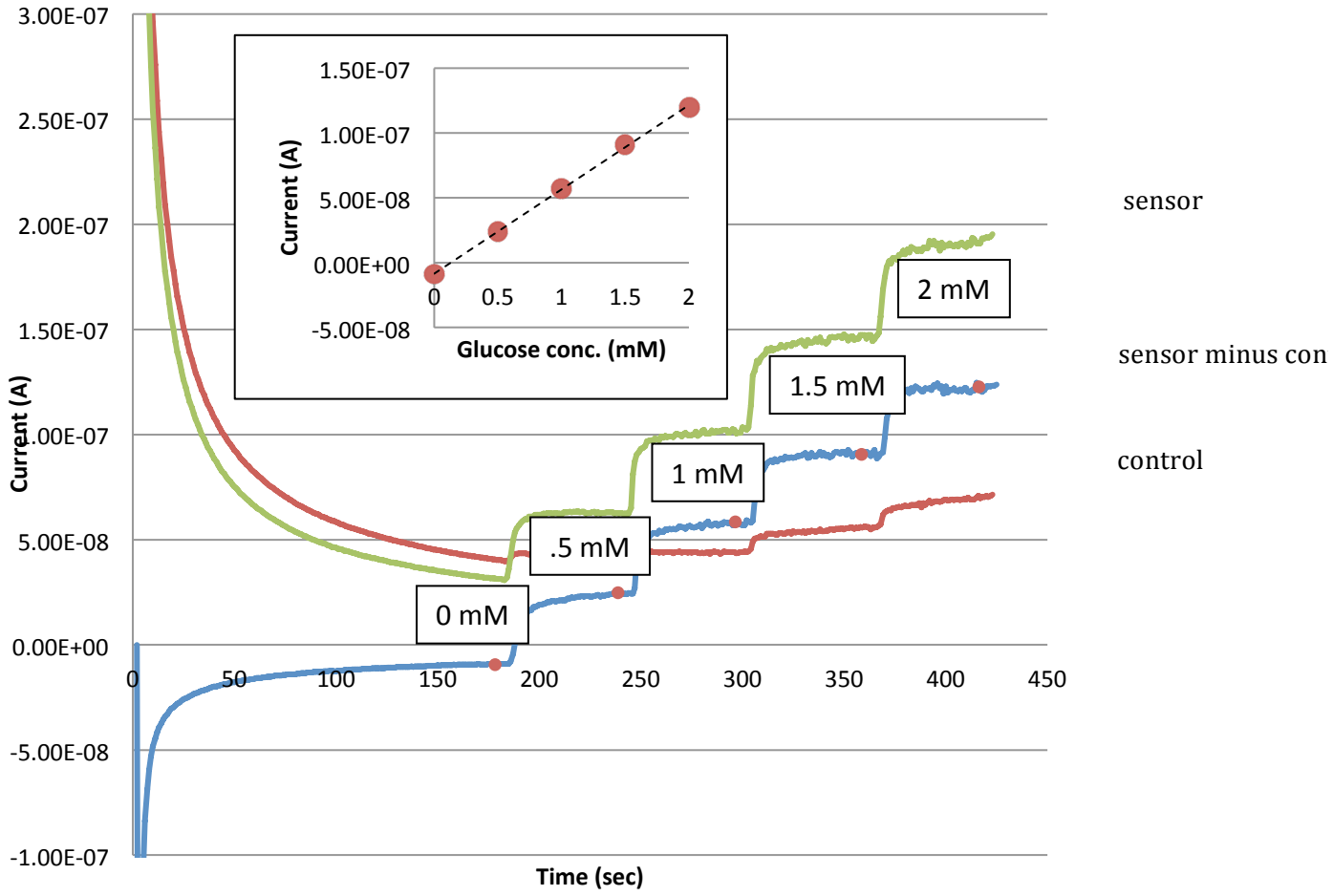

Figure 21. ***In vitro*** **testing of the intraocular glucose sensor. Inset is a plot of stable reading values at each concentration, demonstrating the sensor's linearity.**

Satisfied with the *in vitro* results, we tested the sensors *in vivo*, inside the anterior chamber of a removed rabbit's eye (Figure 20.) As Figure 22 shows, the glucose sensor performed much worse *in vivo*. No differentiation in glucose level signals is seen.

The suspicion is that during the insertion of the sensor into the rabbit's eye, some of the parylene insulation coating was scraped off the sensor, resulting in the very high sensor and control currents, which masked the glucose signal. Also likely is the chemical interference of various components of the intraocular fluid.

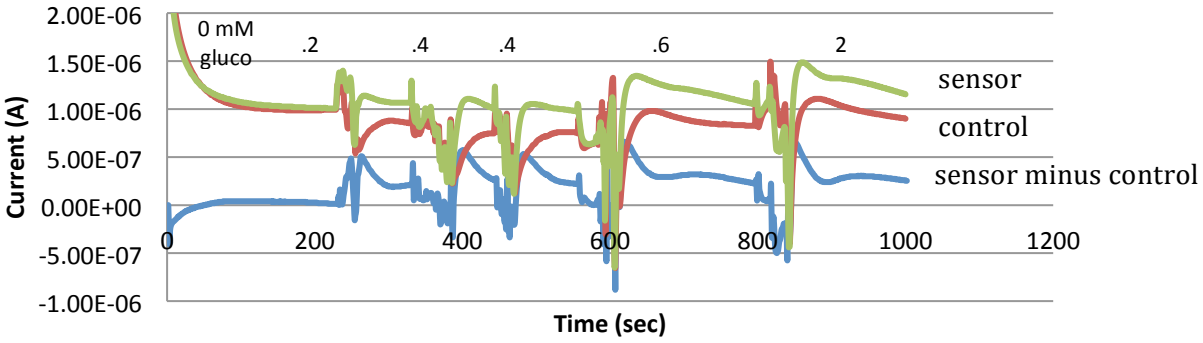

Figure 22. *In vivo* testing of the intraocular glucose sensor. Current reading did not correspond to the injected glucose solution concentration.

3.2 Eye model

The mechanical eye model was created in order to better test the performance of a contact lens based glucose sensor. The lens-based sensor was designed and fabricated by my labmate (Yao, 2010), and functions much the same way as the intraocular glucose sensor described in the previous section. However, the contact lens sensors faces a challenge in that, unlike the intraocular protected environment, the blinking motion of an eyelid creates a constantly changing fluidic environment (Peters, 2002), introduces various motion artifacts into the sensor system, as well as diminishes the fluid layer over the sensor's electrodes to just a few microns. It has not been possible to test this behavior outside of an in-vivo system – the eye model represents a step up from the in-vitro bulk measurement setup, without incurring the cost and additional challenges of in-vivo testing.

The eye model consists of a hemispherical polydimethylsiloxane (PDMS) piece that represents the eye surface and the lower eyelid. The top lid is made of a concave slab of PDMS with the same radius of curvature as the top of the hemispherical "eye". The top lid is positioned using a thin Plexiglas rod attached to a 3D micromanipulator which allows for very precise control of the spacing between the eyelid and the sensor. The bottom lid and the eye are mounted on a rotating axle that is driven by a computer-controlled stepper motor. A shortened and dulled 22-gauge

syringe needle inserted through the PDMS top eyelid acts as a tear fluid outlet. Tubing, with an internal diameter of 500 μm is embedded into the bottom eyelid and serves the role of tear ducts, removing excess tear fluid from the eye surface. PDMS was used as the primary building material due to its well-known surface chemistry (Lee, 2009), which, if needed, can allow for simple biological surface modification in the future. As illustrated in Figure 23, in order to simulate an eye blink, the contact lens containing a glucose sensor is placed onto the hemispherical eye surface, the top eyelid is moved into position just above the lens, imitation tear fluid is fed through the top eyelid via a syringe pump, and the computer, using a custom built LabView program, instructs the stepper motor to rotate the bottom eyelid upwards until it comes into contact with the top lid at a predetermined speed. When the bottom lid touches the top lid, the stepper motor's rotation direction reverses and the bottom eyelid returns to its initial position. Throughout the blink, excess tear fluid is aspirated through the tubing in the bottom eyelid, which allows for a thin sheet of tear fluid to be created over the sensor surface.

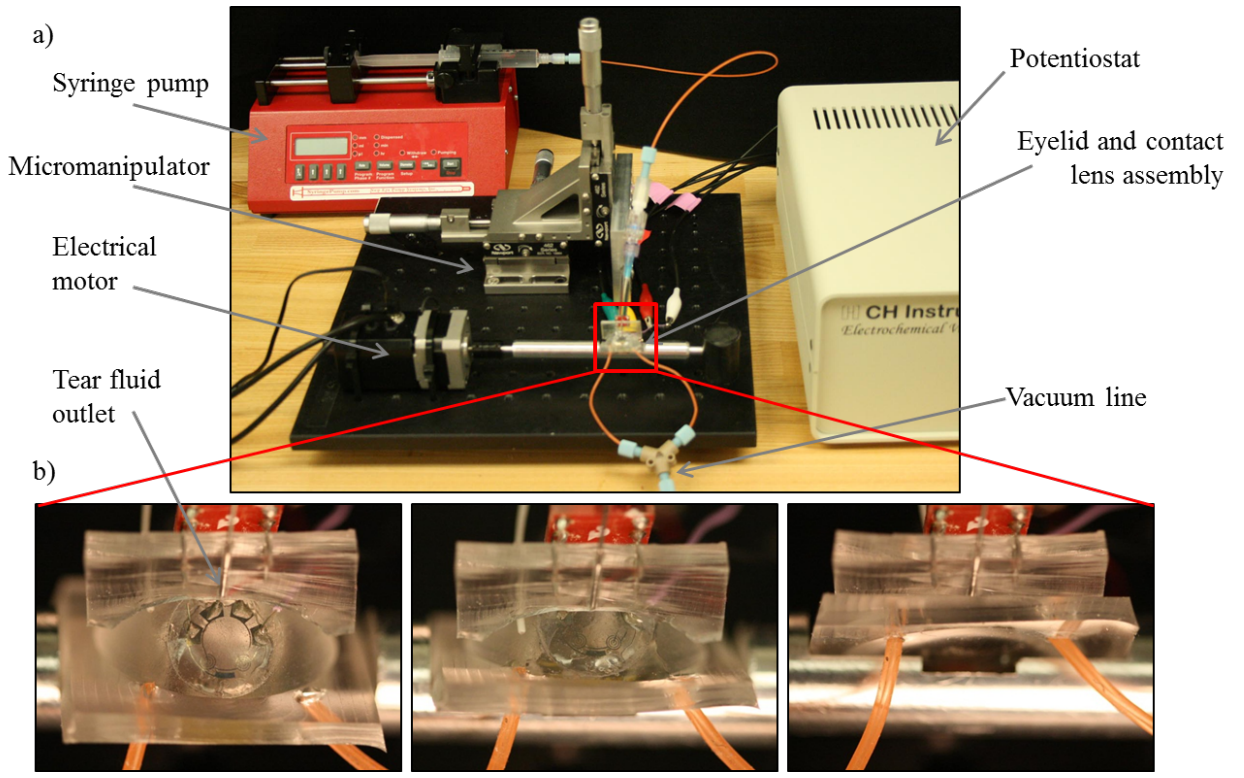

Figure 23. Overview of the eye model assembly. b) a timelapse of a single "blink". Tear fluid enters through the metal line embedded in the top eyelid, and exits through the orange tubing in the bottom eyelid.

The PDMS structure representing the eye and the bottom eyelid was fabricated using a molding process (Figure 24), utilizing a custom machined Teflon mold. The mold consisted of a hemispherical indentation with a radius of 2.54 mm, sunken below the top of the mold by 3 mm. PDMS was prepared at a ratio of 10:1, PDMS base to curing agent (Sylgard 184, Dow Corning, Midland, MI) and poured into the mold. After a one hour degasing step under house vacuum, the mold was placed into a 70 °C oven for 10 hours, allowing the PDMS to cure and harden. The PDMS part was then peeled away from the Teflon mold, placed into a desiccator containing three drops of hexamethyldisilazane (HMDS) and left at house vacuum for one hour. The resulting vapor-deposited HMDS coating on the PDMS surface allowed us to use the PDMS part as a mold by preventing subsequent PDMS coatings from bonding to it.

In order to ensure that the top eyelid has exactly the same curvature as the underlying eye surface, we used the PDMS eye as a mold for the top eyelid. The polymer solution was prepared

using the same procedure as in the previous step, and poured over the PDMS eye mold. The same degassing and curing steps were followed, as well. Upon curing, the resulting concave PDMS piece was separated from the eye-shaped mold and sliced using a scalpel to form a 3 mm thick semicircle – the top eyelid.

Protein fouling of the sensor electrodes is an important concern when dealing with biosensors that come into contact with bodily fluids. My lab has been working on developing an effective method of screening interference redox species via permselective coatings, such as Nafion (Yao, 2010). An important factor in correctly modeling the environment of an eye is, hence, accurately replicating the chemical composition of the tear film solution. Not only will the tear film composition affect the amperometric measurement quality, but also the mechanical characteristics of the blinking motion and tear film thinning and rupture (King-Smith, 2009). We made an imitation tear fluid which contains several proteins commonly found in the eye (lysozyme 1.9 mg/mL, albumin 0.2 mg/mL, and mucin 0.15 mg/mL) dissolved in phosphate buffer saline (1x, PBS, pH 7.4). The exact protein combination has been derived from (Ohashi, 2006).

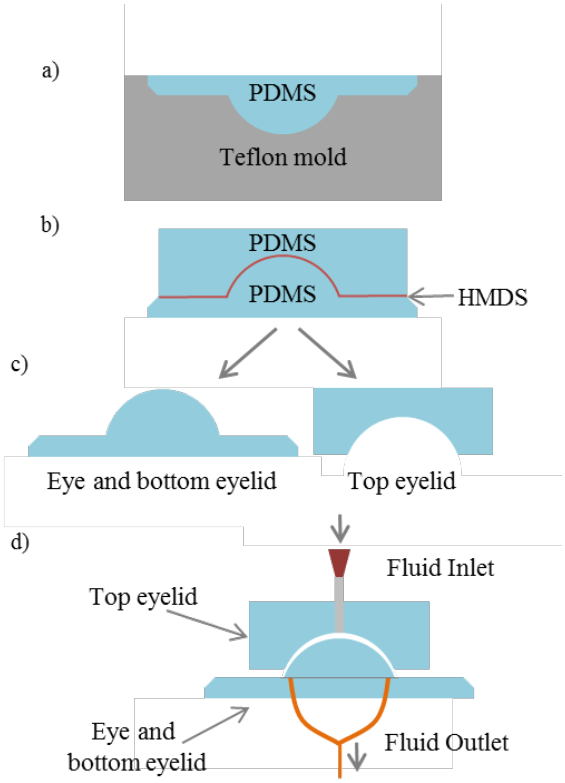

Figure 24. PDMS eye model fabrication procedure. a) The eye and bottom eyelid are fabricated using a custom Teflon mold. b) After an HMDS deposition, the PDMS eye piece fabricated during the previous step, is used as a mold for the top eyelid. c) HMDS coating allows the two pieces of the eye model to be separated. d) final assembly of the eye model, with the fluid inlet and outlet microtubing inserted into the top and bottom eyelids, respectively.

Such an eye model allows us to test the electrical characteristics of contact lens based microscale sensors in an environment that closely resembles a human eye without the inconvenience and expense associated with working with live animals. The eye model also allows us to test structural integrity of the electronics assembled on the contact lens, as well as test various fouling resistant coatings by cycling the blinking motion for a prolonged amount of time.

4 Neural Interfaces

Our ability to effectively communicate with neural tissue is central to creating the next generation of brain-computer interface systems. Recurrent Brain-Computer Interfaces (RBCI) hold great promise in facilitating future clinical treatments of ailments related to damaged neural tissue (Berger, 2005). As opposed to traditional BCI, recurrent BCI assumes a feedback mechanism where

one part of the nervous system is stimulated based on the information gathered from another part of the nervous system, allowing for such applications as bridging missing neural pathways and conditioning of cortical neural circuitry during stroke rehabilitation.

An important challenge in the creation of a standalone, implantable RBCI is the creation of a biocompatible, durable platform that can house all the necessary computational and power transduction circuitry. Cortical electrode arrays built on thin flexible polymer arrays are an attractive option as they can be placed directly on the neural tissue both sub- and epidurally, without causing excessive damage associated with penetrating electrode arrays. Furthermore, interfacing the electrodes with the stimulation and recording circuitry is facilitated by the fact that several proposed materials can be used in standard microfabrication.

4.1.1 Review of state-of-the-art flexible neural arrays

Several recent attempts at a flexible neural tissue interface platform can be seen in Figure 25, below. Figure 25 a shows a flexible parylene-based array containing twenty-seven planar platinum microelectrodes. This electrode array was implanted, epidurally, onto a rat's spinal cord for a period of eight weeks. During that time, using pulsed stimulation of the underlying neural tissue, walking motion in the hindlimbs could be recreated. This work confirms the compatibility of parylene based arrays with neural tissue, and the effectiveness of planar, epidural arrays in targeted stimulation of spinal neural tissue. Figure 25 b shows a parylene based device that integrates two stimulation electrodes, a pair of discrete capacitors, an RF coil, and an IC that converts the received power into an electrical stimulus delivered to one of the electrodes. The system – a step towards a wireless retinal stimulator - has been tested in vitro, in a removed and dissected eye. While the fabrication process used in this report does not allow for a large scale integration of the various components used, the successful demonstration of power transfer to a parylene-based RF coil is encouraging. Figure 25 c demonstrates the best example of a large (252-electrode) passive cortical recording array. While it has no integrated circuitry, the report

showcases a 5-month long chronic implant that covered an entire hemisphere of a monkey brain. The planar platinum electrodes showed good performance throughout the implantation period. A large *active* array that demonstrates the state of the art is shown in Figure 25 d. 360 pairs of transistors were fabricated on 260 nm thick "nanoribbons" and transferred onto the flexible polymer substrate. While extremely rudimentary, the circuitry allowed for simple multiplexing of the recording signal. While the fabrication process is not applicable to use with traditional bare-die integrated circuits, the demonstration of large scale integration of active components on a flexible substrate is an important milestone in non-penetrating ECoG array fabrication.

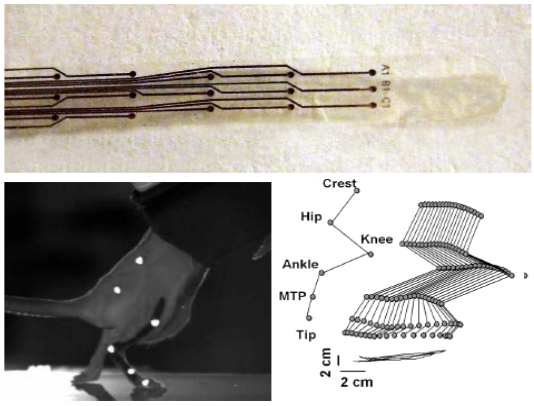

a) Spinal stimulation in a rat (Nandra, 2011)

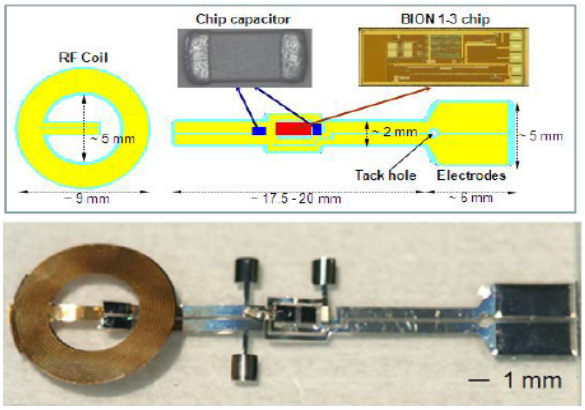

b) Wireless retinal stimulator (Li, 2009)

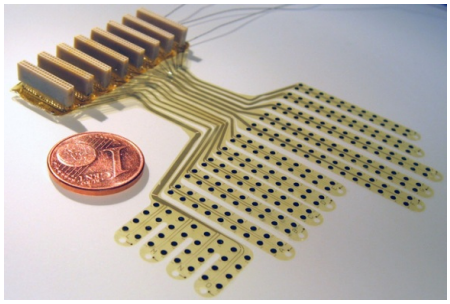

c) Cortical recording, polyimide arrays (Rubehn, 2009)

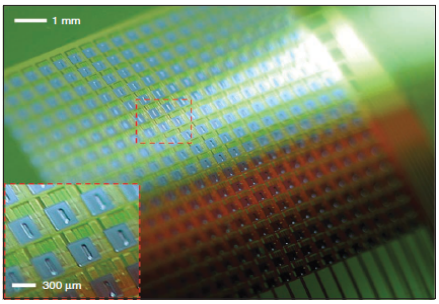

d) Amplified cortical recording arrays (Viventi, 2011)

Figure 25. Four examples of existing planar flexible neural electrode arrays.

Having shown the effectiveness of flexible, planar ECoG arrays, attempts were made to design a process that would allow for integration of large numbers of high lead count, bare-die ICs

onto the polymer surface. The two methods described in Figure 26, below propose first immobilizing the ICs in either through-holes or indentations etched into a silicon wafer with the electrical pads facing up, and then fabricating the polymer electrode array on top. These methods have the distinct disadvantage that the IC is put through the entire fabrication process of the flexible array, increasing the risk that either the array or the circuit will be damaged in the process. Clearly, a better IC integration procedure must be developed.

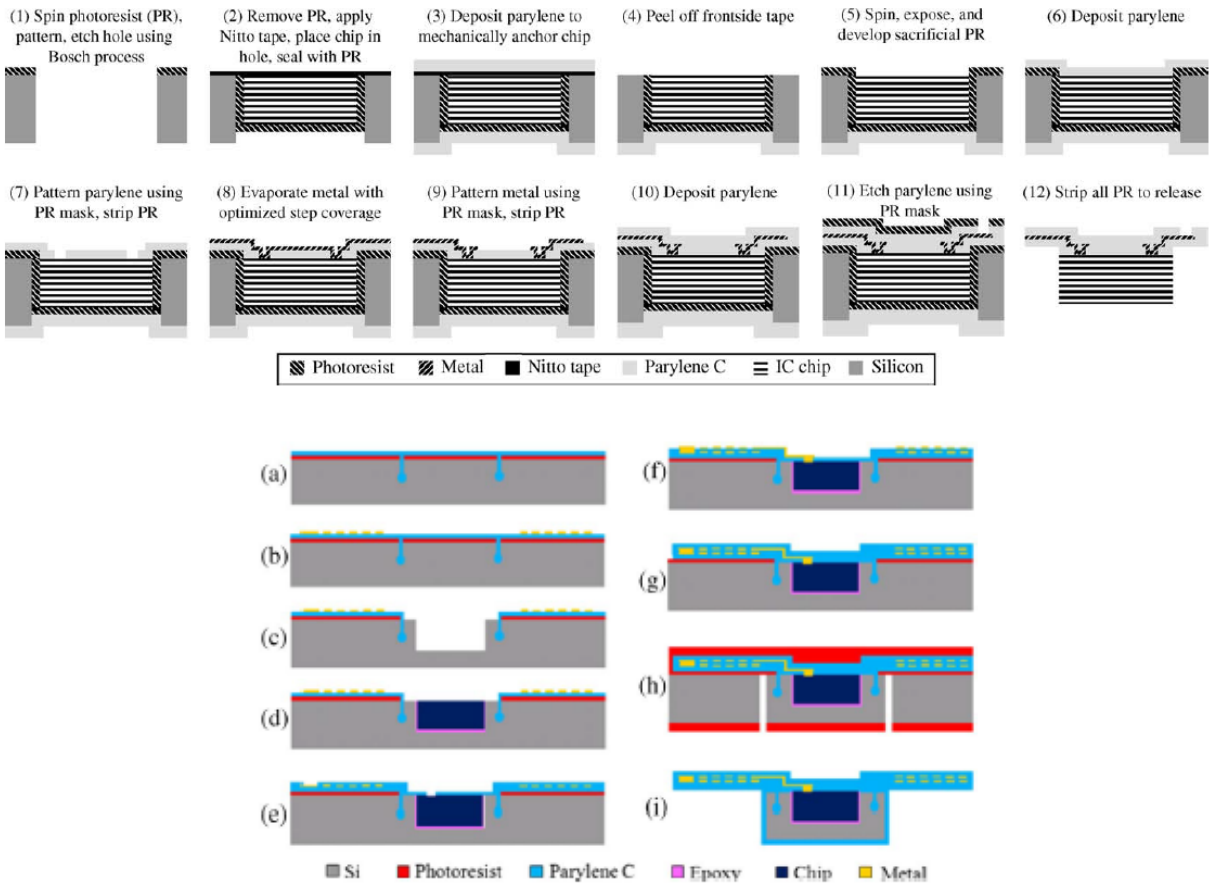

Figure 26. Two high lead count IC packaging processes (Rodger, 2006 and Wen Li 2010)

4.1.2 Quantifying Electrode Performance

All of the electrode arrays have been thoroughly characterized both *in vitro* and *in vivo*. Three main approaches are used in order to fully characterize the electrodes: alternating current impedance spectroscopy (ACIS), cyclic voltammetry (CV) and voltage excursion analysis. Measured

using a standard three-electrode electrochemical cell with an Ag/AgCl reference electrode, ACIS allows us to probe the impedance of the individual electrodes by applying a voltage signal of varying frequency and measuring the resulting impedance. Platinum is used as the electrode material, so the major factors determining impedance are the series resistance of the metal traces leading from the edge of the array to the electrodes and the capacitance of the electrodes. Since only the reversible faradaic processes are activated during stimulation and the redox product remains attached to the electrode, the behavior of the metal is described by using an extra capacitive term, not a resistive term as is usually the case for faradaic reactions (Merrill, 2005). A typical ACIS plot can be seen in Figure 28, in the top panels. At lower frequencies, the capacitive term dominates the impedance, whereas the series resistance determines the impedance at lower frequencies. Cyclic voltammetry plots are generated by performing a voltage sweep, at a certain rate, and measuring the current. The area enclosed in a single CV curve is equivalent to the amount of charge that has been accessed during the cycle. This technique allows us to determine how active the various charge transduction processes are on the electrodes. Figure 27 shows the peak CV current during platinum oxidation for electrodes of different size. As expected, the current increases with increasing electrode area, as more surface area becomes available for the reaction. The CV can also determine the width of the "water window" (Hudak, 2010) – the range of electrode potentials at which no gas is generated from the breakdown of water. For platinum, the water window is normally taken as -.8V to .8V. Applying voltages outside of the lower window will lead to catastrophic breakdown of the electrode surface both through mechanical (gas bubble generation), as well as electrochemical means (platinum corrosion in a chloride containing environment). Figure 28 shows what happens to an electrode when the current output required of it drives the potential too high and destroys the electrode.

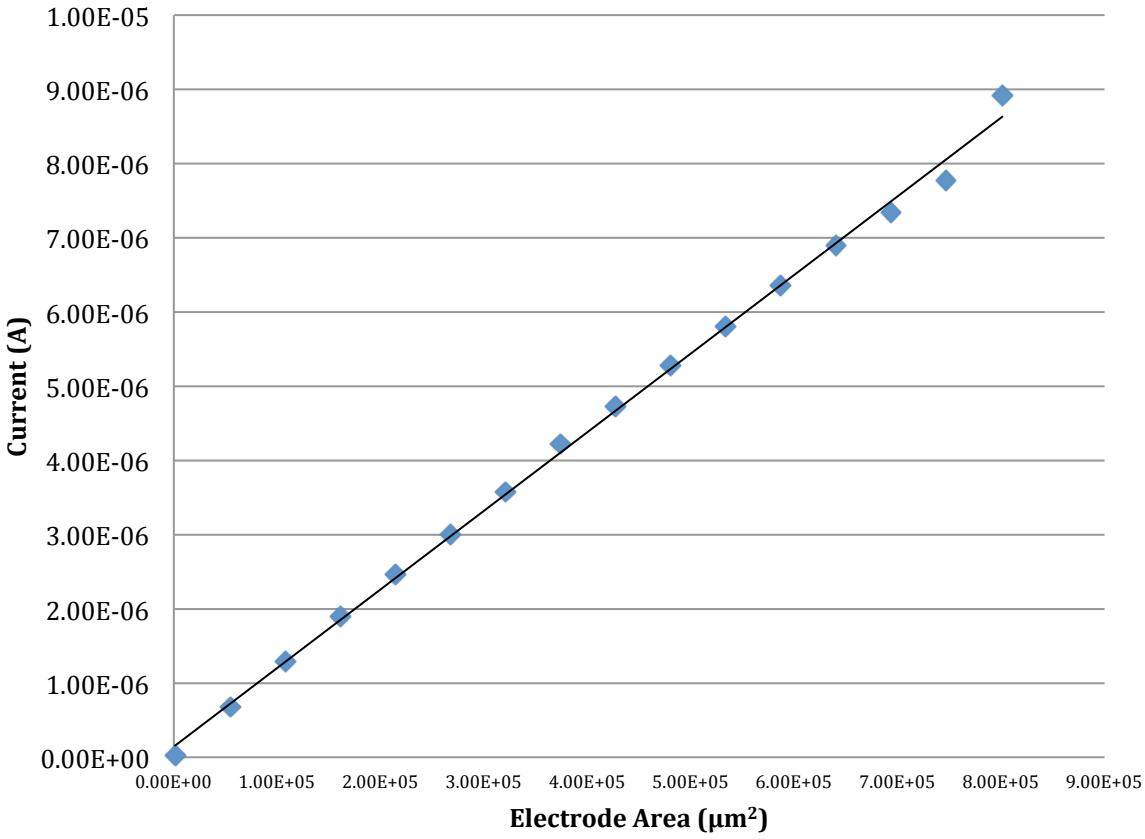

Figure 27. Peak current during the platinum oxidation phase of a CV cycle plotted against the size of the electrode.

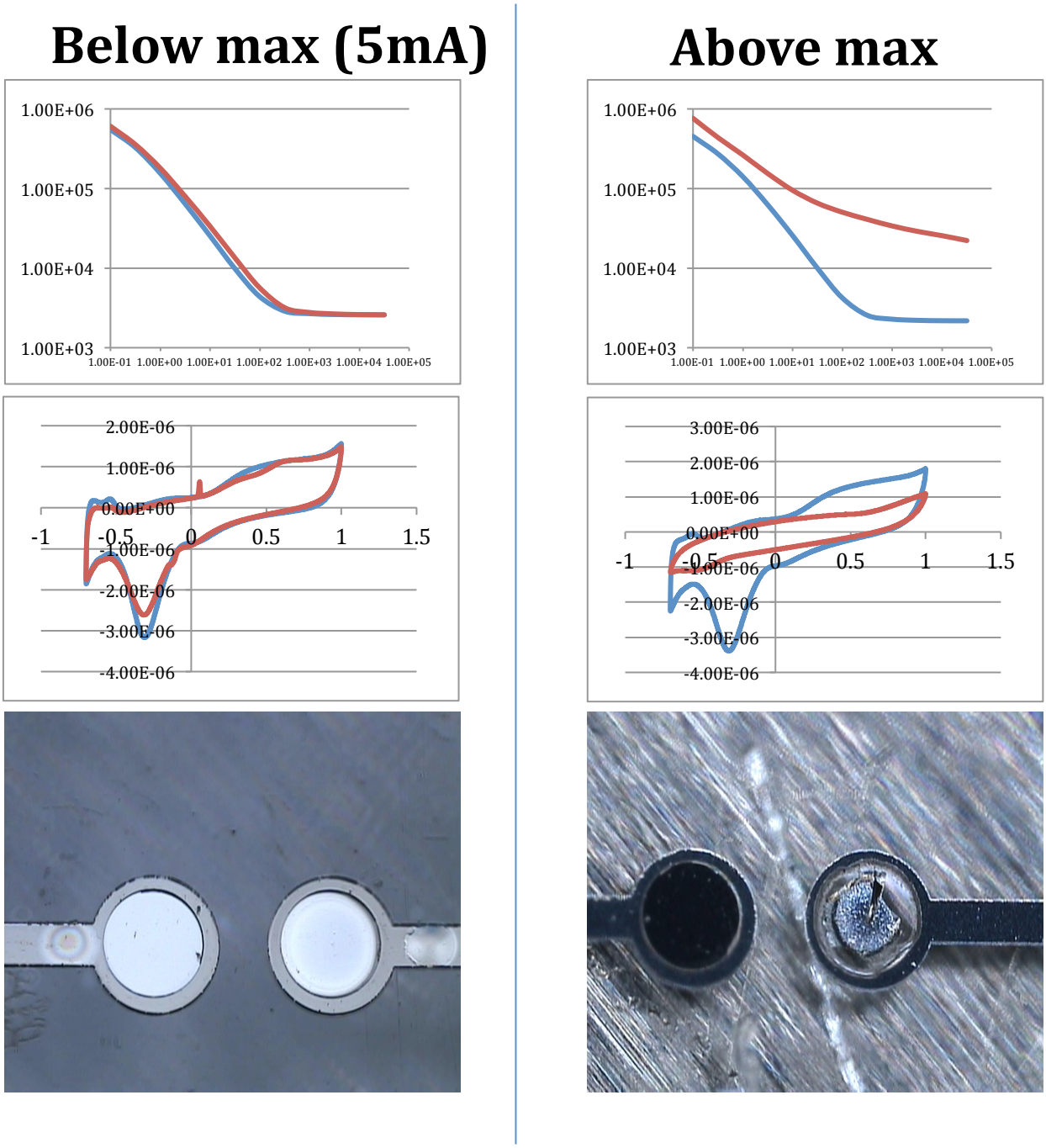

Figure 28. Comparison of an electrode stimulated below and above the maximum current level (5 and 6 mA, respectively, 1 Hz, 200 µsec biphasic pulses for 48 hours.) ACIS and CV (top two panels, respectively) show similar behaviors before (blue) and after (red) the 5 mA stimulation test. Optical microscope imaging also does not show any damage to the electrode. Not so for the 6 mA test – both the ACIS and CV curves show significantly decreased performance. The optical image shows that the stimulated electrode (right) is completely eroded.

Voltage excursion analysis provides a third way of analyzing the characteristics of the electrodes. Because in neural stimulation current is the critical parameter, it is useful to apply a current pulse

(biphasic, anodic first, 200 µsec per phase) to the electrode and record the voltage necessary to provide the current. In order to isolate just the potential at the electrode, one must subtract the series resistance contribution from the data. Such a plot can be seen in Figure 29, which shows the potential at the electrode during the anodic phase of the pulse. The potential reaches the boundary of the water window, at -.8V, at roughly 3000 µA. This implies that the maximum amount of current one can output on this electrode with the pulse parameters mentioned above, is 3 mA. It must be noted that the accuracy of this method is limited due to the inexact nature of series resistance approximation. The series resistance arises from the fact that the resistance of the thin platinum traces is around 1000 Ω.

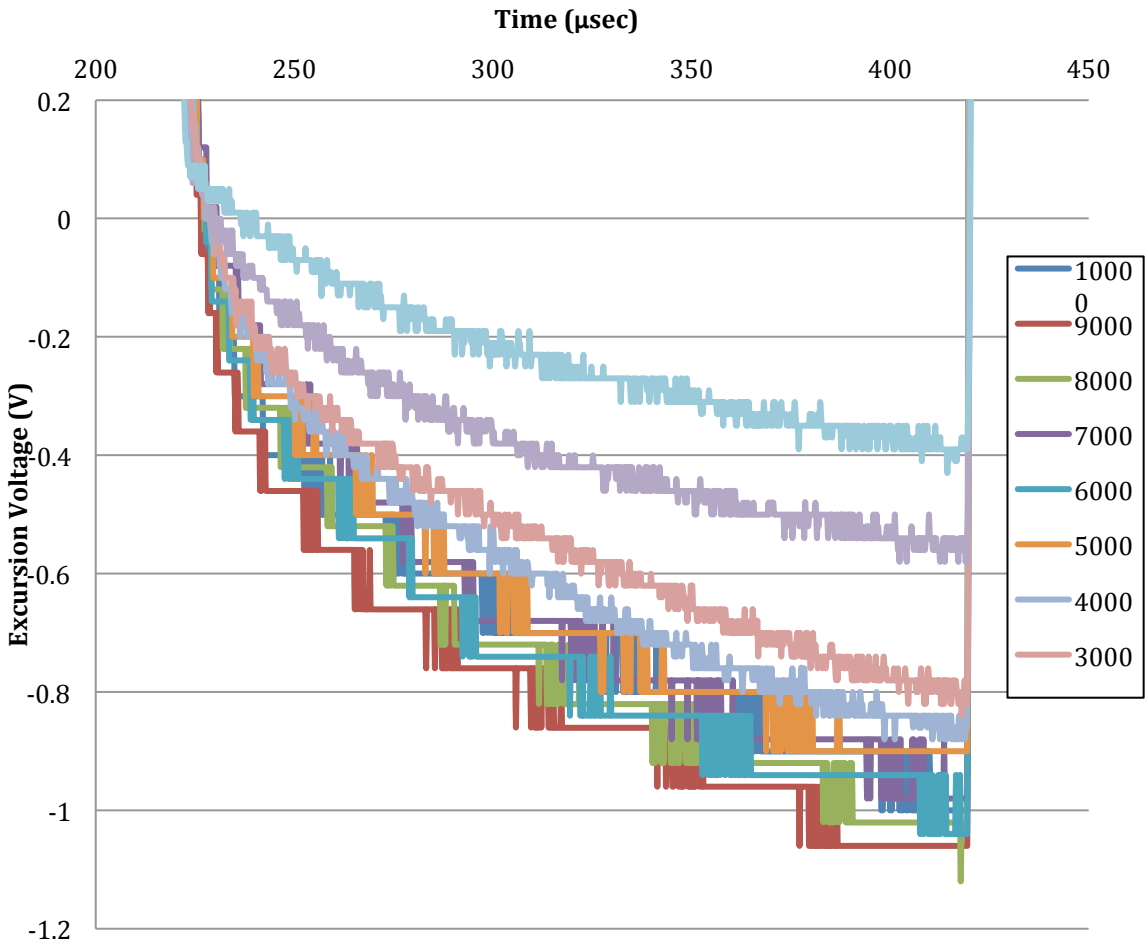

Figure 29. Voltage excursion plots for the 200 µsec anodic part of a biphasic pulse at different currents. The edge of the "water window" lies at roughly -.8V, indicating that if stimulated beyond 3000 µA, the safe injection charge will be exhausted on the electrode and oxygen gas will be generated instead.

The active, amplified recording electrode array shown in Figure 45 has been tested *in vivo*, measuring the somatosensory evoked potential (SEP.)

The two-channel array was placed subdurally on the spinal cord in an anesthetized rat at the cervical level. The rat forelimb was electrically stimulated (20 V, 0.5 ms pulses) to evoke a SEP in the spinal cord. Figure 30 shows neural responses, recorded on both the un-amplified and amplified channels, to 150 forelimb stimuli. After the negative stimulus artifact, there was a clear SEP recorded on both channels. The SEP was larger and had shorter latency on the un-amplified channel, consistent with this channel being closer to where the forelimb afferents are processed in the spinal cord. For the 10 ms interval before the stimulus, the noise was 30% lower on the amplified channel than on the unamplified channel (109 µVrms versus 74 µVrms).

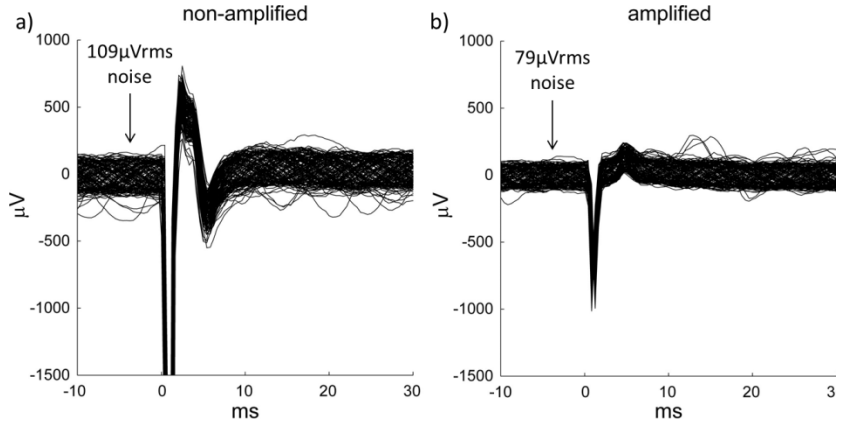

Figure 30. In vivo somatosensory evoked potential response in the spinal cord of a rat. a) neural signal recorded from a passive electrode b) neural signal recorded from a signal preamplified 100-fold by a custom amplifier integrated next to the recording electrode (reduced back 100-fold in above plot.)

4.2 Parylene Electrode Arrays

4.2.1 Basic Parylene/Platinum Neural Electrode Arrays

Parylene has been used as the flexible polymer substrate due to both its biocompatibility, strength and compatibility with microfabrication processes. Platinum was chosen as the electrode metal due to its relatively high safe injection charge capacity – a critical parameter for neural stimulation. In Figure 31 are several examples of recently completed neural arrays. Figure 31a

shows four spinal arrays fabricated in different geometries – from a simple linear array, to a T-shaped array that is designed to wrap around the spinal cord. Figure 31b demonstrates a cortical recording/stimulation array coupled to a custom-made circuit that allows for a reliable interconnection between the array and testing instrumentation. All of the arrays in Figure 31 have been tested *in vivo*, with the cortical array being implanted chronically.

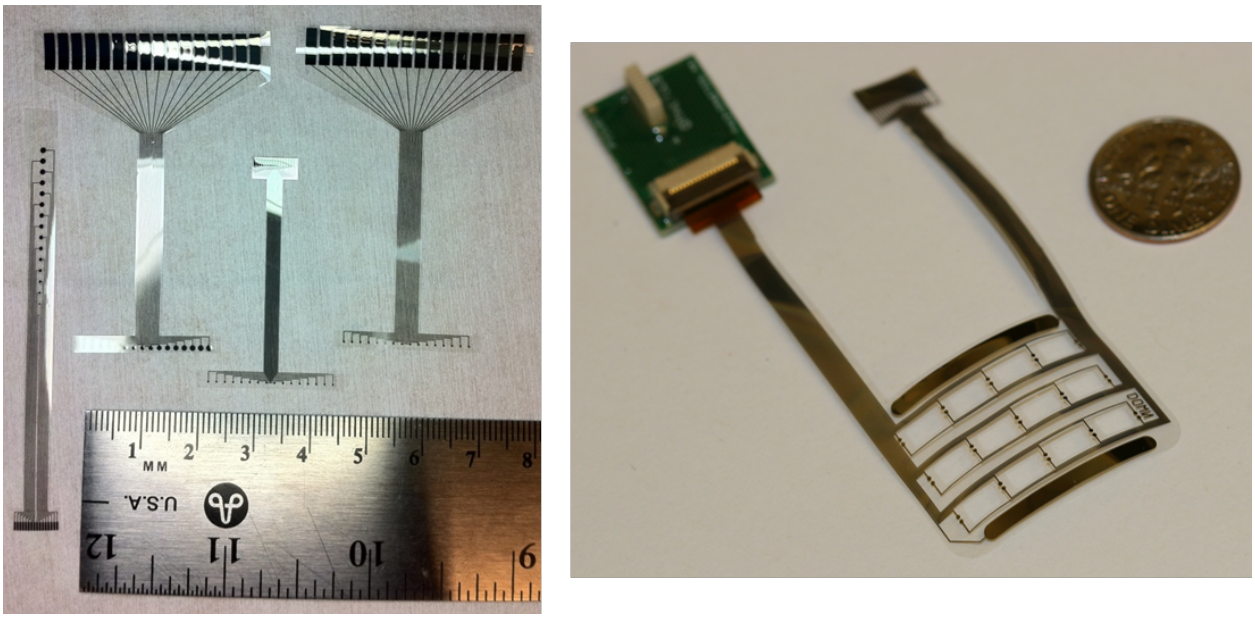

Figure 31. Recently fabricated neural electrode arrays that have been tested *in vivo.* Spinal arrays (left panel) and cortical array (right).

4.2.2 Neural Electrode Array Fabrication

All parylene-C deposition has been performed using the SCS Labcoter2 gas phase deposition system. Using the manufacturer provided recipes, a deposition rate of 1 μm of parylene polymer per gram of parylene monomer has been observed. Prime quality 4" silicon wafers have been used as the substrate of choice due to compatibility with microfabrication equipment used in subsequent processing steps. After the initial parylene deposition (normally 5-10 μm), a layer of metal is deposited via electron beam deposition. All lithographic steps used a positive AZ4620 photoresist, spun at 1000 RPM for 30 seconds, with a 10 second spin-up rate. Chromium and titanium can both be used as adhesion layer metals, as both adhere strongly to parylene. Chromium/platinum (10

nm/150 nm) were normally used as platinum provides both a quality neural electrode interface, as well as a strong plasma etch barrier in subsequent processing. Care must be taken to reduce the temperature at which platinum is deposited for fear of deforming the underlying parylene substrate. This can be achieved via a reduction of the platinum deposition rate to 1 angstrom per second, as well as an introduction of frequent pauses during the evaporation process that allow the heat to dissipate from the parylene layer. Platinum liftoff is performed in pure acetone, with care taken to not strongly sonicate the wafer as that can severely damage the pliable parylene layer. A second, capping parylene layer is deposited over the entire structure, binding well to both the first parylene layer, as well as the metal traces. A chromium/nickel (10 nm/100 nm) etch hard mask is patterned and evaporated on top of the second parylene layer. A pure oxygen ICP plasma etch can then be used to etch the parylene, which will define the outline of the electrode arrays (by removing all parylene around the array outline), as well as the electrode openings (by removing only the top parylene layer, leaving the parylene layer underneath the electrode intact). Platinum metal can easily withstand the said plasma etch, with no need to additionally mask the electrodes. Defined parylene arrays can then be easily detached from the silicon substrate by soaking the wafers in DI water. The Cr/Ni hardmask can be removed via a short soak in a chromium etchant solution. Rinsed well, the arrays are then ready for use.

4.2.3 ECoG Array Geometry

The ECoG arrays have been designed to occupy a single hemisphere of a macaque's brain. Two have been implanted simultaneously, epidurally. Thirty 300 μm platinum electrodes (Figure 32) have been designed to create stimulation electrode pairs (stimulating and counter) within one millimeter of each other. Additionally, two very large electrodes on either side of the array can be used as the counter electrode of a stimulation pair. The long electrode leads terminate in a Hirose-style ZIF mounting, and are long enough to protrude above the skull surface, allowing for direct electrical connection to the brain surface. A fully fabricated ECoG array, together with the Hirose

clamp can be seen in Figure 31. Unfortunately, the platinum electrodes have not been able to withstand the high electrical currents necessary to evoke a physiological response via epidural stimulation, requiring us to look for alternate stimulation electrode materials.

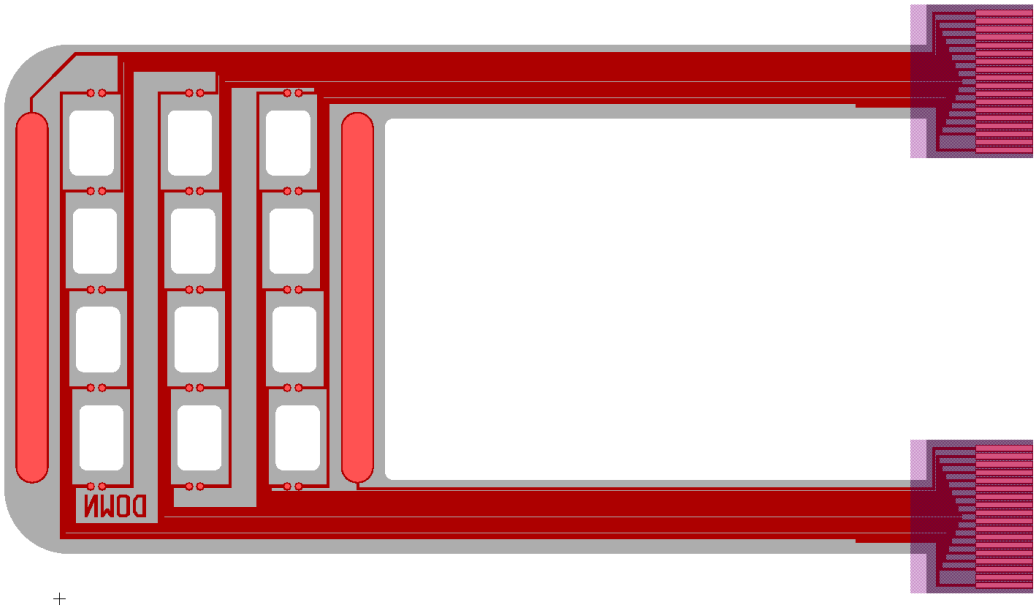

Figure 32. A thirty stimulation electrode pair array for ECoG.

4.2.4 Spinal Array Geometry

As part of the Keck electrode array project, we have also been building a system to record the signal off of a few places on the cortex, analyze the information, and then stimulate the nerves in the spinal cord based on the information conveyed to it by the cortex. An example of an early version of such an array is shown in Figure 33. Figure 31 shows the completed spinal arrays.

Figure 33 shows an early version of a T-shaped spinal array that allows us to electrically address multiple sites on the spinal cord. The array is designed such that the vertical part that contains the electrodes is meant to be wrapped around the spinal cord. The design also allows for a surgeon to cut off any unnecessary electrodes during surgery without disrupting the electrical performance of any of the other electrode sites.

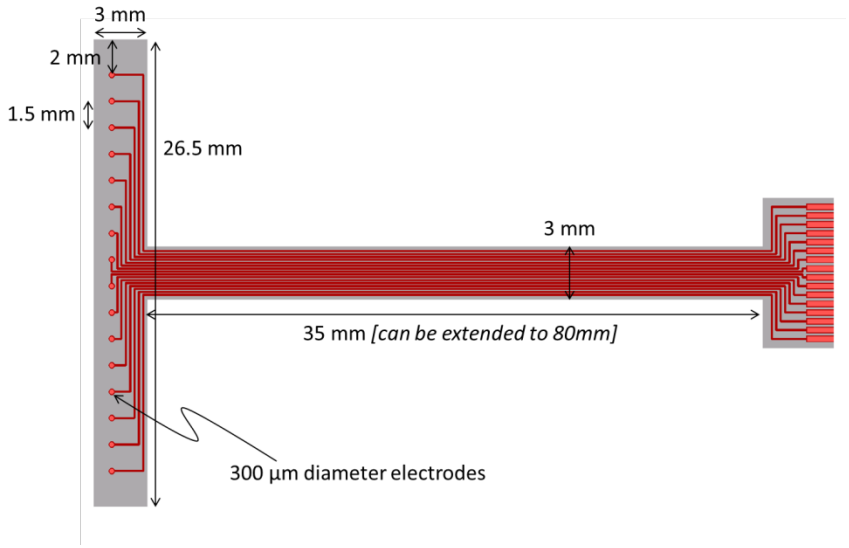

Figure 33. An example of a previously fabricated and tested spinal cord array. The left portion containing the electrodes can wrap around the spinal cord.

A second iteration of the spinal stimulation arrays has been designed and fabricated to take advantage of the boney part of the spinal column in immobilizing the array (Figure 34). This allows the surgeon to fix the array in place (via bone screws or epoxy glue) and allow the electrode containing part to freely slide along the spinal cord. If some slack is built into the array during the placement surgery, the array can stay immobile with respect to the spinal cord during the subject's normal movement. By keeping the stimulation sites constant, such an arrangement can significantly improve the stimulation effectiveness of the array. Figure 35 illustrates the design parameters of the S-shaped spinal stimulation arrays. Additional screw tabs can be added in parylene if bone screws are used to immobilize the electrode array.

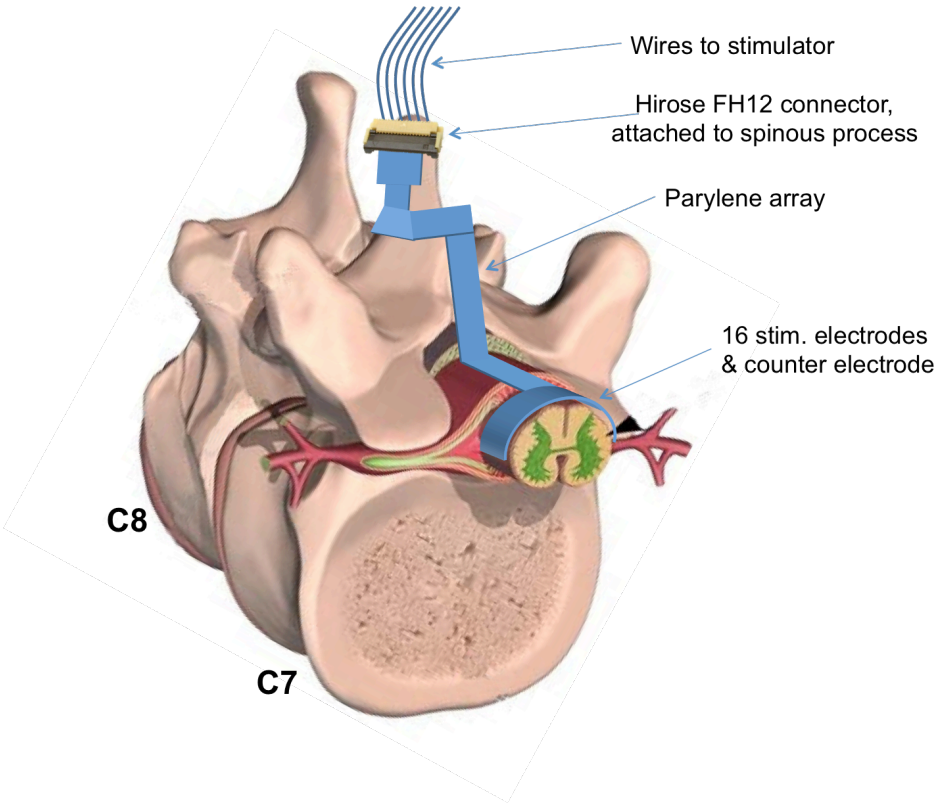

Figure 34. A cutaway of a representative electrode placement site on the C7 vertebra. The electrode array is fixed to the boney part of the vertebra, allowing for the electrode containing section to slide freely along the spinal cord. (Spine diagram courtesy of http://www.healthpages.org/anatomy-function/lumbar-spine-lower-back-structure-function/)

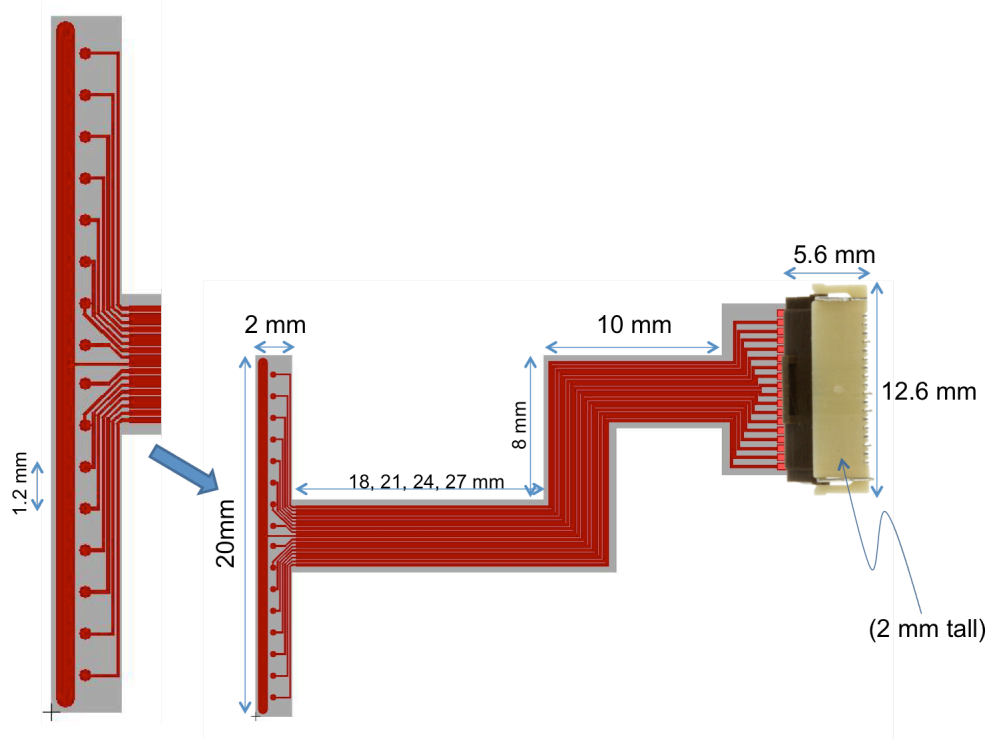

Figure 35. Layout design for the S-shaped spinal stimulation arrays. The bend in the electrode array allows for a more secure mechanical connection to the vertebra.

4.2.5 Long-term Platinum Electrode in-vitro Testing

A long-term (33 day) soak of a platinum electrode parylene array showed signs of array degradation. Liquid seepage between the parylene material and metal allows for a larger electrode area to be exposed to the electrolyte solution, leading to an increased area of the CV curve which correlates with available safe injection charge capacity (Figure 36a). An increase in the voltage necessary to generate a .5 mA pulse (Figure 36b) can be explained by electrode surface fouling. This effect can be cancelled by repeated electrode stimulation which can rejuvenate the electrode surface. This is an important point as related to in-vivo experiments. While the high frequency stimulation may not be affected by the liquid seepage due to electrolyte diffusion constraints, it is imperative to run at least twenty "cleaning" stimulation cycles (at a physiologically relevant amplitude) before engaging in in-vivo stimulation.

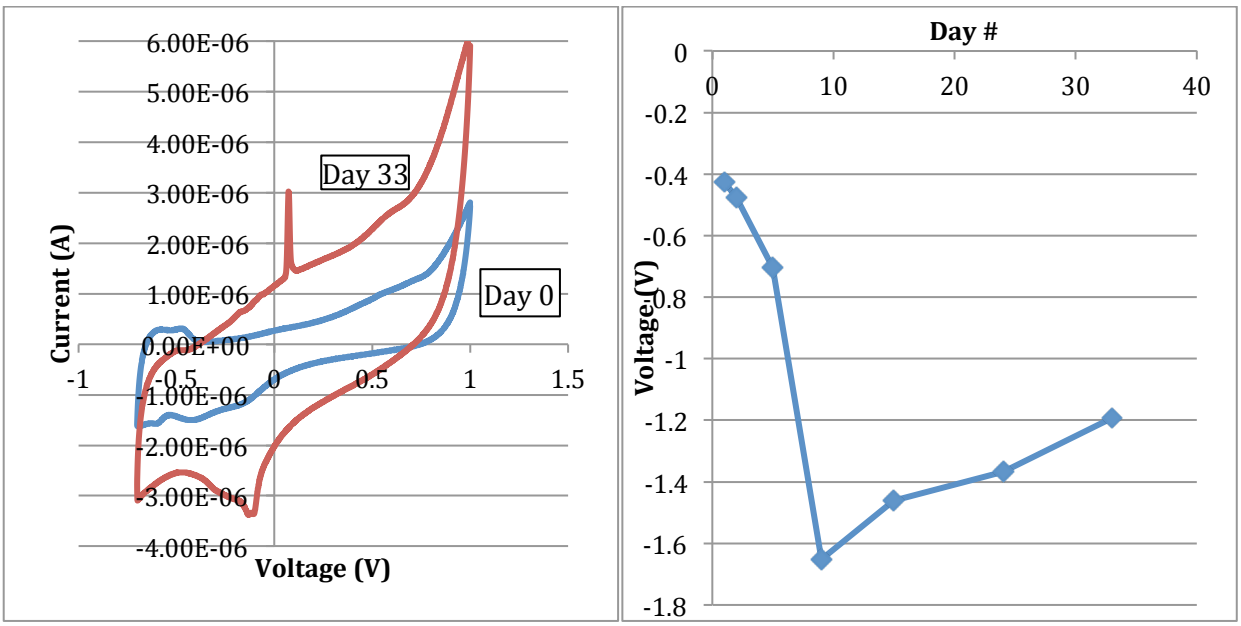

Figure 36. Long term electrical testing of the platinum electrode arrays has shown an expected increase in CV current (left) due to parylene-metal delamination, as well as a reversible degradation in the voltage excursion parameter, derived from a .5 mA stimulation (right).

4.2.6 Iridium Oxide Electrodes

As it has been shown in the previous section, platinum does not meet our requirements for neural stimulation – it simply has too little safe injection charge capacity. Instead of the required 10 mA, the actual stimulation maximum is around 3-4 mA (Figure 29).

Figure 37 shows a previously reported dramatic difference in safe injection charge capacity between platinum and iridium. This is due to the increased number of oxidation states of iridium as compared to platinum. Since the iridium redox mechanisms are very similar to platinum, namely oxide formation and hydrogen plating, we preserve the biocompatible nature of reversible pseudo-faradaic reactions as the basis for neural stimulation.

I have adapted the Lesker Sputter Coater tool in the UW microfabrication facility in order to deposit a sputtered iridium oxide film (SIROF). The IrOx crystal electrochemical characteristics are affected by the oxygen content of the crystal, as well as its thickness (Figure 38). Both have been optimized for the microfabrication requirements of iridium oxide – while a thicker and more oxygen rich IrOx layer could have provided a larger charge capacity, the manufacturing of such an

electrode proved to be impossible. Since the last step of the IrOx microfabrication process is a lift-off step in chromium etchant, under light sonication, a conformal sputtered layer of IrOx has been shown to be impossible to remove if it is thicker than 800 nm. Similarly, a 37.5% oxygen crystal has been shown to be just structurally stable enough to withstand the lift-off process. IrOx containing a larger amount of oxygen is far too brittle, freely delaminating from the underlying platinum.

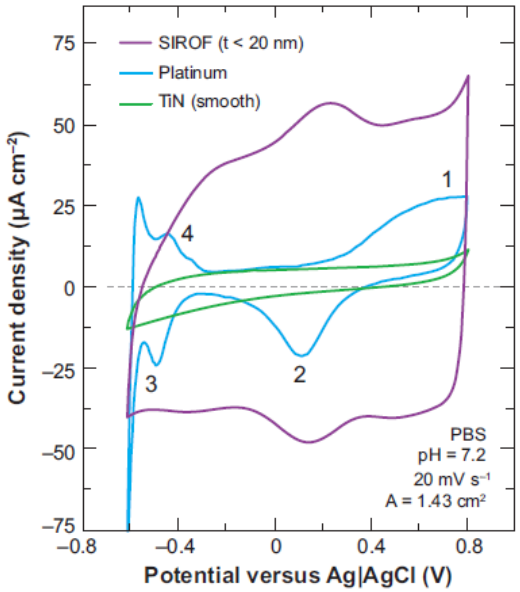

Figure 37. CV plots demonstrating the different amounts of safe surface charge of various materials (proportional to the area enclosed by the curve. Note that sputtered iridium oxide (purple) has significantly more charge capacity than platinum (blue) (Cogan, 2008).

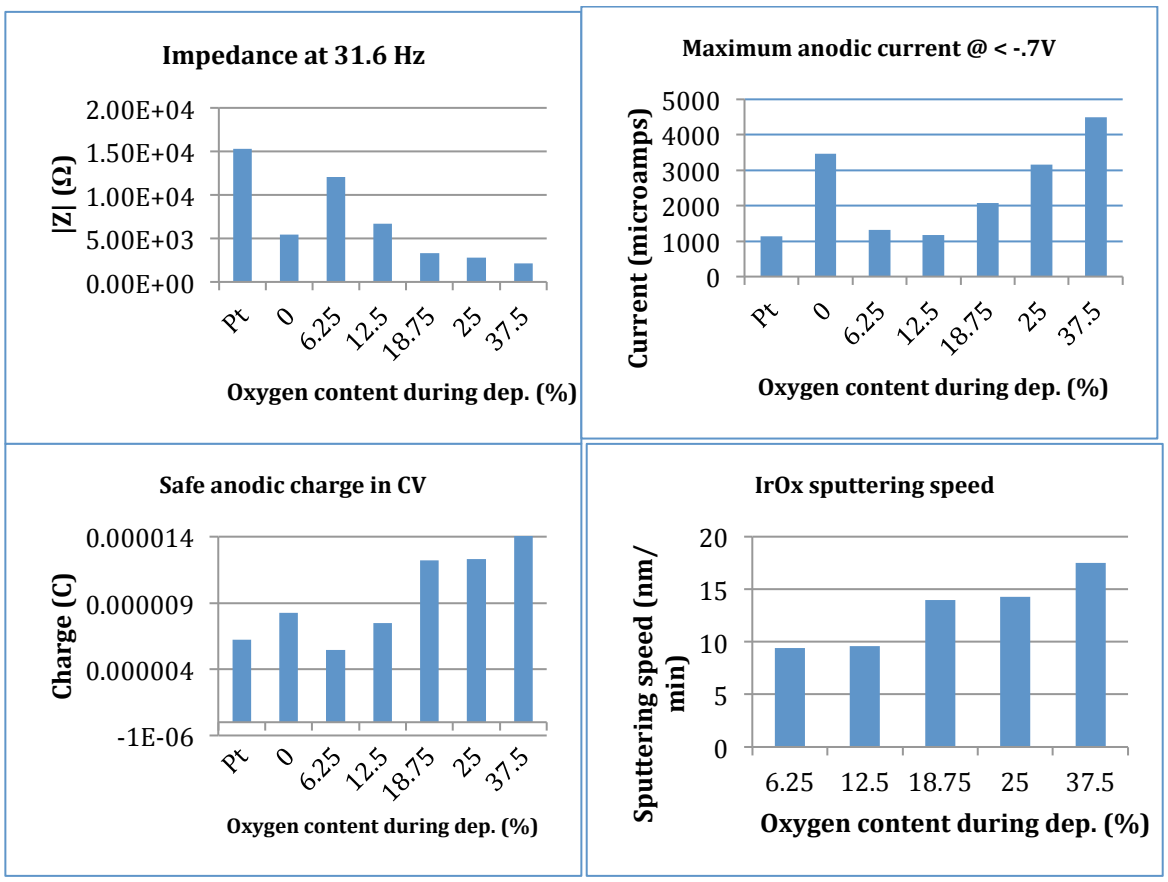

Figure 38 Iridium oxide deposition parameters and performance characteristics.

4.2.7 Iridium Oxide Electrode Microfabrication

The standard platinum-on-parylene microfabrication process is followed through the plasma etching of electrode openings. After the etching is complete, the parylene arrays are not lifted off the carrier wafer, but are spin coated with photoresist, and a layer of chromium (100 nm thickness) is patterned over the arrays, using the electron beam evaporation system, with openings over the electrodes. During the subsequent liftoff and rinse steps, the arrays are detached from the carrier wafer. The arrays can be reattached with metal clips to another substrate (e.g. a blank silicon wafer) and inserted into the metal sputtering tool (Lesker Lab 18). Iridium oxide is then sputtered over the entire array using the following settings:

	Target Cleaning (10 minutes)	IrOx Deposition (17.5 nm/min)
MFC1 (Oxygen)	0	60
MFC2 (Argon)	100	100
Power (W)	100	10
Pressure (mTorr)	10	10

The settings above have been found to create a stable plasma for a given pumping setting controlled by the cleanroom staff. If the pumping speed of the system has been changed, the minimum pressure of 10 mTorr may not be achievable, and the process must be run at a higher pressure. Also, higher concentrations of oxygen may not be able to generate a stable plasma at the metal target. After the deposition, the entire array is submerged into liquid chromium etchant (Cr Etchant 1020, Transene) and is weakly sonicated. The chromium layer, acting as a sacrificial layer, lifting off within 30 seconds, removing deposited IrOx everywhere but the exposed electrode surfaces. Great care must be taken to not allow the sonication to disturb the metal electrode adhesion to the parylene substrate. A sputtered IrOx layer thicker than 800 nm has been found to be too thick for successful liftoff, as the thick crystal layer delaminates from the underlying platinum.

4.2.8 Neural Array in-vitro Performance Comparison – Pt vs. IrOx

In-vitro characterization and comparison of IrOx and platinum electrodes clearly shows the benefit of the larger available injection charge in IrOx crystal. Figure 39a illustrates the different shapes (indicative of different native redox processes) of the CV curves for the two metals, taken in 1x PBS solution. The amount of charge available can be estimated by calculating the area enclosed between the axis and the initial CV anodic swing (from 0V to -.6V, bottom track). The 37.5% oxygen containing, 800 nm IrOx electrode (highest performing combination), contains 4.3 times the amount of safe injection charge as that of the plain platinum electrode.

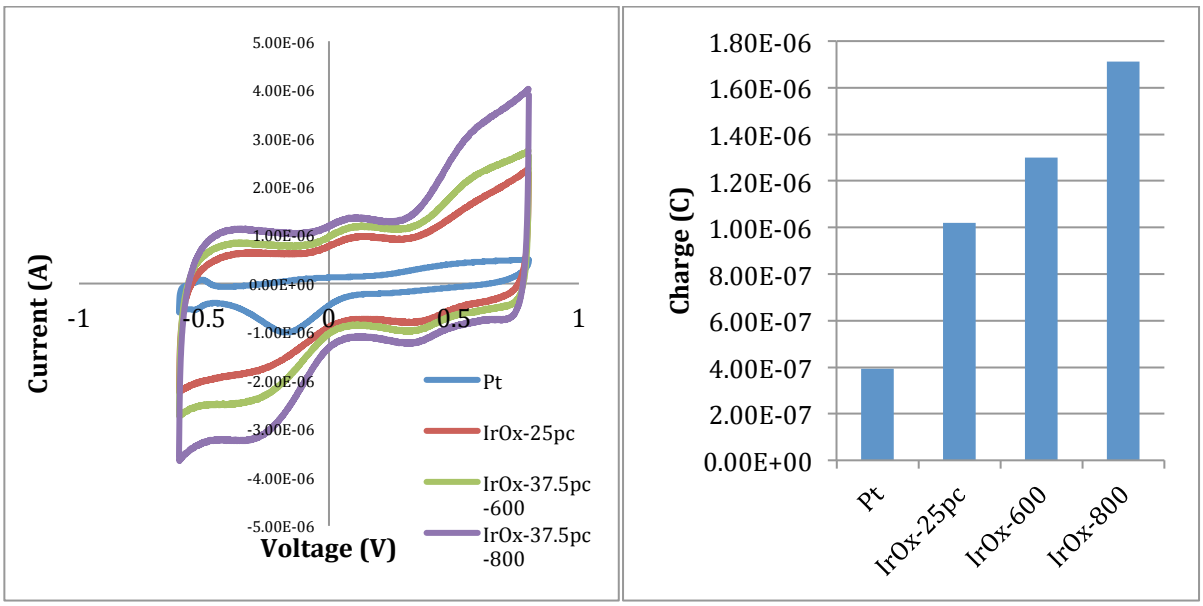

Figure 39 a) Comparison of CV characteristics of platinum and iridium electrodes, in-vitro (1x PBS). b) comparison of available safe injection charge.

Figure 40 describes the ACIS behavior of both the platinum, as well as IrOx electrodes. As expected, there is very little difference at the capacitive element dominated, higher stimulation frequencies. However, there is a marked decrease in impedance in the lower frequency range, where the higher injection charge capacity of the IrOx electrodes results in significantly lower impedances.

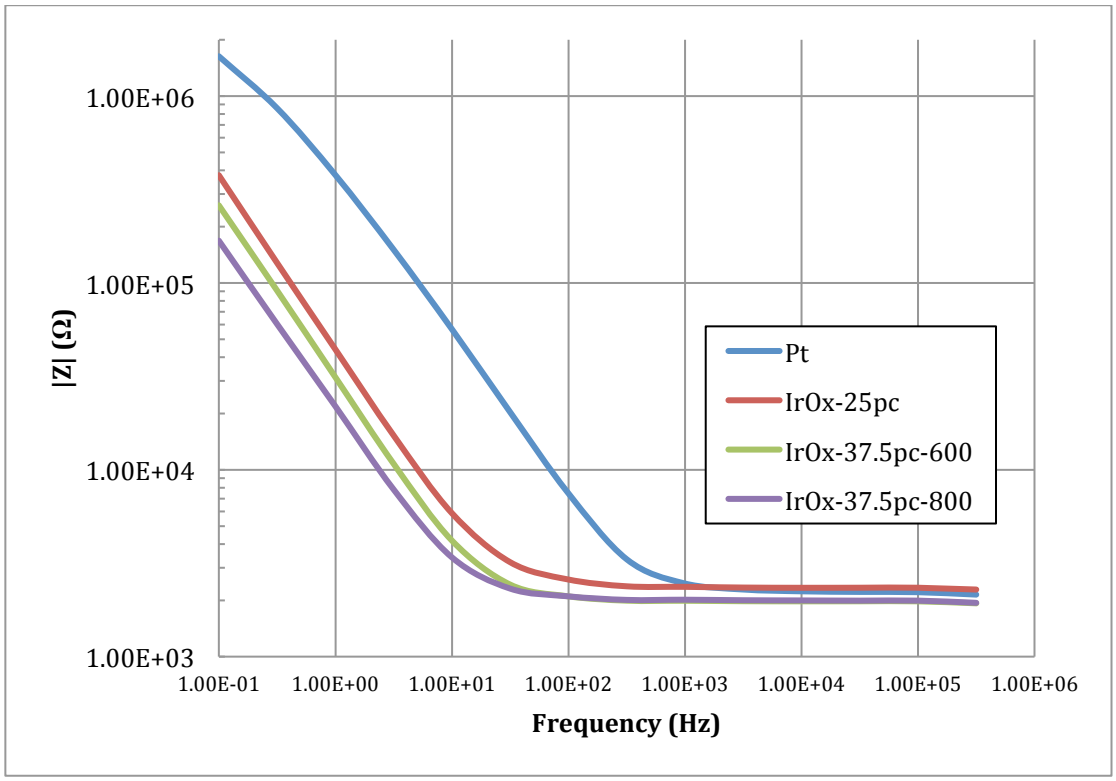

Figure 40 ACIS, in-vitro characterization and comparison of various platinum and iridium electrodes.

Figure 41, however, provides the most practical method of comparing the stimulation qualities of the two types of electrodes. The most pertinent characteristic of the electrodes is their ability to inject charge into the surrounding electrolyte solution without being destroyed by corrosive redox reactions – the voltage excursion analysis measures precisely that. From the plot below, you can see that our best performing IrOx electrode – the 37.5% oxygen, 800 nm thick crystal – can perform

electrical stimulation of up to 8 mA without reaching unsafe potentials. A significant increase over both platinum, and lesser IrOx electrodes.

However, in the case of IrOx, it is actually permissible to operate for prolonged periods of time in the "prohibited" domain outside of the water window, with minimal damage to the electrodes. Note that this is not the case with platinum electrodes which corrode very fast once unsafe voltage levels are reached. To illustrate this point, I have operated a single IrOx (37.5% O_2, 800 nm thick) electrode at 15 mA (.2 msec biphasic pulses, 1 Hz, 1x PBS solution) for 14 hours, achieving 50000 stimulation cycles. Figure 42 shows that there is virtually no corrosion on the electrode surface, nor is there a significant increase in the voltage excursion levels necessary to achieve the target stimulation current. The implication of this finding is that the practical maximum for stimulation current is significantly higher than the theoretical maximum. Thus, the very high stimulation currents necessary for cranial and spinal stimulation can be achieved via electrodes such as these.

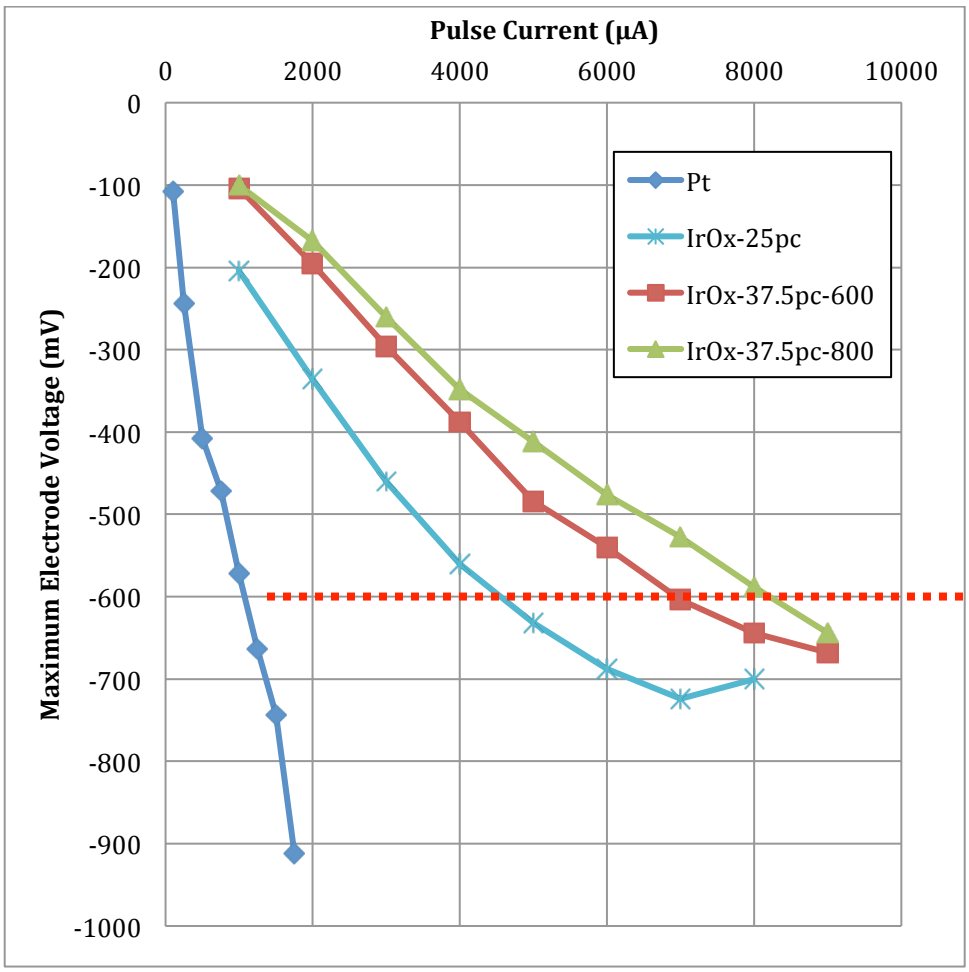

Figure 41 A comparison of voltage excursion values at various stimulation currents for platinum and IrOx electrodes. Standard .2 msec, biphasic square pulse was used. Red line demarcates the water window at -.6V

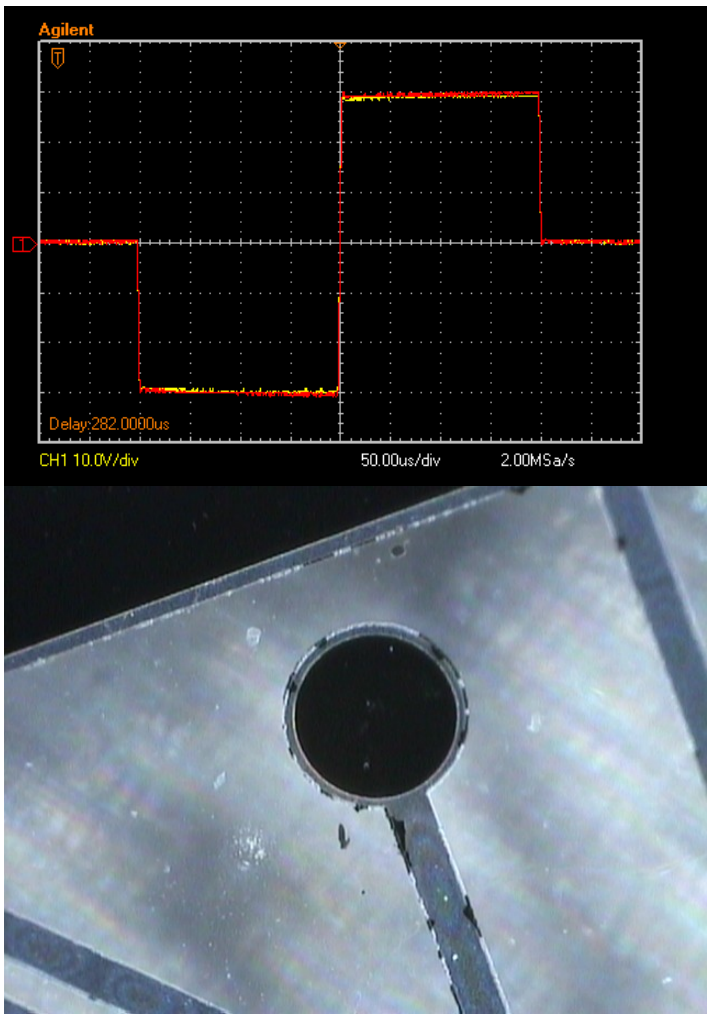

Figure 42 15 mA, biphasic, 200 µsec pulses. 50,000 times. 1x PBS. No visible damage to the electrode.

4.2.9 Iridium Oxide Electrodes in-vivo Behavior

An iridium oxide s-shaped spine stimulation array has been chronically implanted into a macaque monkey, epidurally, at the C7 vertebra. I have made an attempt at measuring the stimulation characteristics of the electrodes after the animal's post-surgery three week long recuperation period. Considering the amount of time that the electrodes have spent inside the animal, I have first attempted to clean the electrode surfaces via high current stimulation. Namely, I used a train of standard bi-phasic 200 µsec square stimulation pulses at 10 mA, and observed the number of pulses necessary to achieve a stable stimulation profile, for a given electrode. I used the large on-board counter electrode as the opposite electrode. It normally took twenty stimulation

cycles for the electrode surface to be sufficiently clean for stable stimulation readings. After the twenty cleaning pulses, the following two pulses (achieving 10 mA and 15 mA) were recorded. As can be seen in Figure 43, the in-vivo stimulation voltage excursions are significantly larger than those observed in-vitro, ranging from 2 to 10 times the observed values in-vitro. The variation in magnitude is likely due to the nonhomogeneous nature of the stimulation environment inside the vertebra.

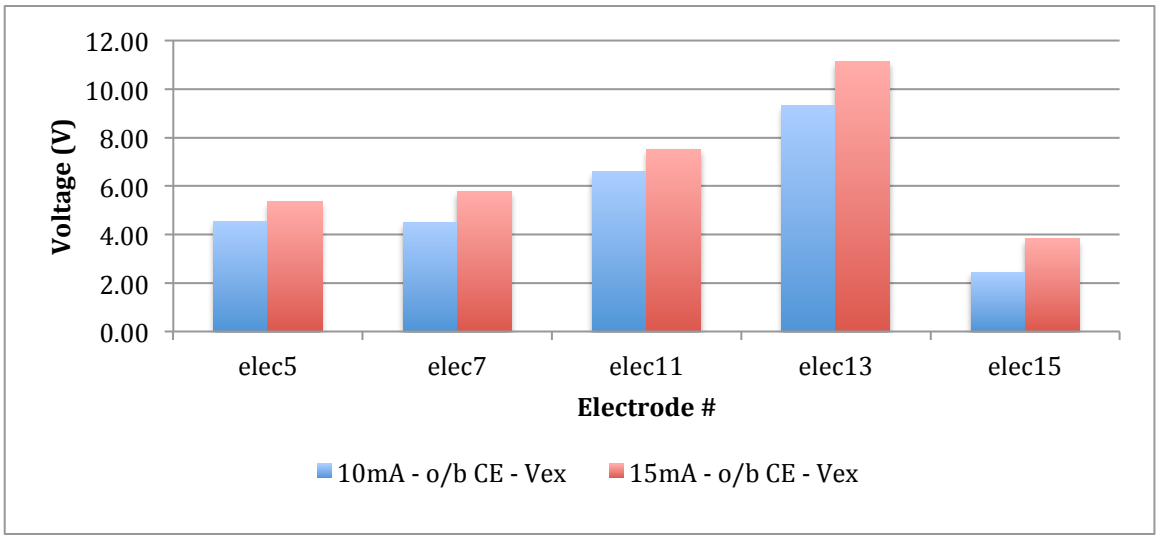

Figure 43. Voltage excursion measurements for five 300 micron IrOx electrodes. Stimulation delivered in-vivo, epidurally at the C7 vertebra of a macaque monkey.

I have also looked at the in-vivo CV and ACIS characteristics of the implanted electrodes (Figure 44). The CV exhibited an additional resistive component, as well as being larger overall – indicative of faradaic redox processes in the complex electrolyte environment in the spinal cord. The ACIS showed a marked increase in the higher frequency (capacitance dominated) ranges, which likely indicates residual surface contamination of the electrodes. Collection of such data during in-vivo experiments could result in a convenient method of analyzing the quality of the electrodes and their placement. However, more data is required in order to make meaningful conclusions.

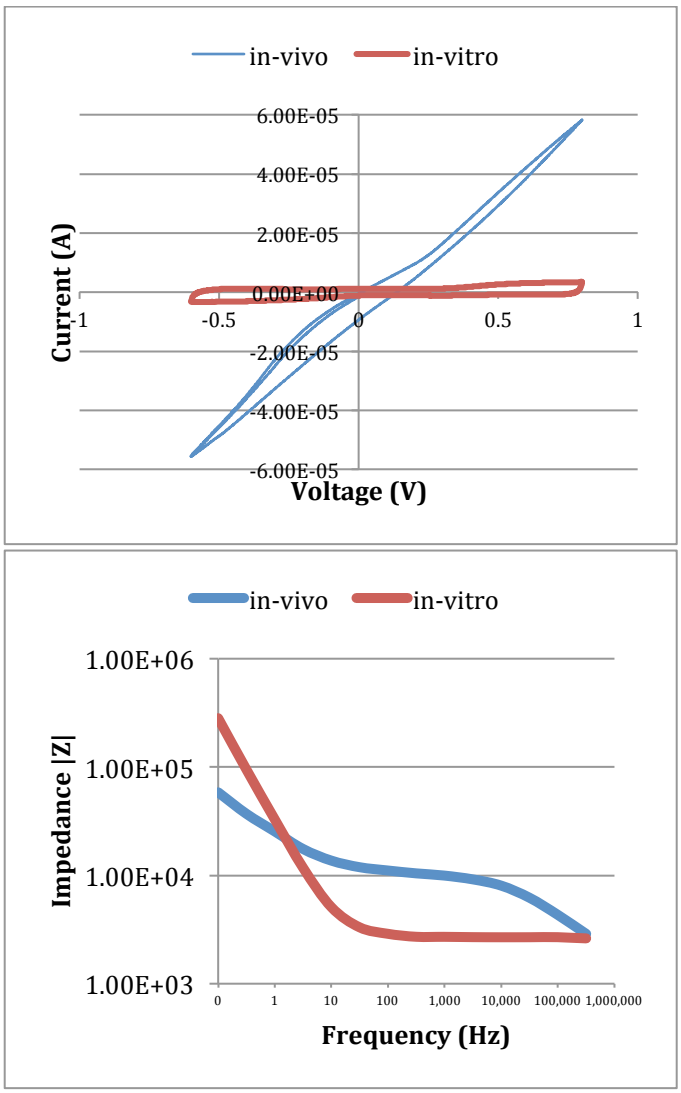

Figure 44 CV and ACIS characteristics of spinal IrOx electrodes, in-vivo.

4.3 Double-sided Active Neural Arrays

Of paramount importance in neuroscience is the idea of non-invasiveness – limiting the interaction between the inorganic measurement and stimulation components and the target neural tissues. Active neural arrays contain a large number of embedded electronic components that may create a highly non-uniform surface, which may negatively impact any neural tissues that come in contact with it. One way to eliminate this problem is to maintain a perfectly smooth electrode array surface that contacts the neural tissue, while placing the large electronic components on the

opposite side of the array. I have come up with two ways of fabricating such a device – both efforts are described below.

4.3.1 Double-sided, Manually-aligned Neural Array Microfabrication

As an example of both the versatility of the standard parylene array process, as well as IC integration, described below is a two-sided parylene fabrication process used to create a non-invasive neural recording array with a single active electronic component. Integrating a custom low noise amplifier chip with recording electrodes improves signal fidelity by minimizing the length of high-impedance unamplified neural signal interconnect. The recording array was tested by measuring an in vivo somatosensory evoked potential (SEP) in a rat.

My parylene fabrication process simplifies the integration of custom chips onto parylene substrates used in neural recording and stimulation. The key challenge in fabricating such devices is the ability to process both sides of the parylene substrate. My approach differs from previously reported integration schemes (Li, 2010) in that all of the parylene substrate fabrication is completed prior to the attachment of the chip. While integration of various active circuit components has been reported (Rodger, 2006; Li, 2010) I specifically address the major issue of low signal-to-noise ratio faced by neural recording in electromagnetically noisy environments, such as operating rooms. I integrated a specially built, sub-mm^3, 40 dB-gain low-noise amplifier (Yeager, 2009) onto a parylene based electrode array and demonstrated the efficacy of this device by observing in-vivo SEP measurement results in a rat (Figure 30).

The two-sided parylene-based electrode array fabrication is detailed in Figure 46. Standard photolithography is used to fabricate a single 150 nm platinum layer between two 10 μm layers of parylene-C, on a silicon wafer. Vias to the recording electrodes and the array outline are etched using a reactive ion etch (RIE) process. The arrays are peeled off the silicon substrate, sprayed with photoresist on one side, and reattached to the wafer with the photoresist side down. Heat curing the photoresist secures the arrays on the wafer. Bonding pad vias are defined using

photolithography, the array is reattached to the wafer using Crystalbond adhesive and RIE etched. Crystalbond is removed with acetone and the array is reattached to the carrier wafer using the photoresist spraying technique. The newly exposed pads are covered with a solder-compatible Cr/Ni/Au. Bond pads on the chip and the parylene substrate are coated with a low melting temperature solder (Lingley, 2010) and the two are soldered together using a flip-chip micropositioning system. The resulting electrode Figure 45 array measures 7 cm in length, 4 mm in width and 20 µm in height (1 mm high at the amplifier chip). Two recording electrodes (one amplified, one passive) consist of 300 µm diameter exposed platinum disks.

The fully-integrated low power neural recording amplifier was fabricated in a 0.5 µm SOI BiCMOS process. A two-stage topology using capacitive feedback provides high linearity and a precisely-controlled gain of 40 dB from 1 Hz to 6 kHz. The amplifier consumes 8 µA while exhibiting an input-referred noise floor lower than 5 µVrms.

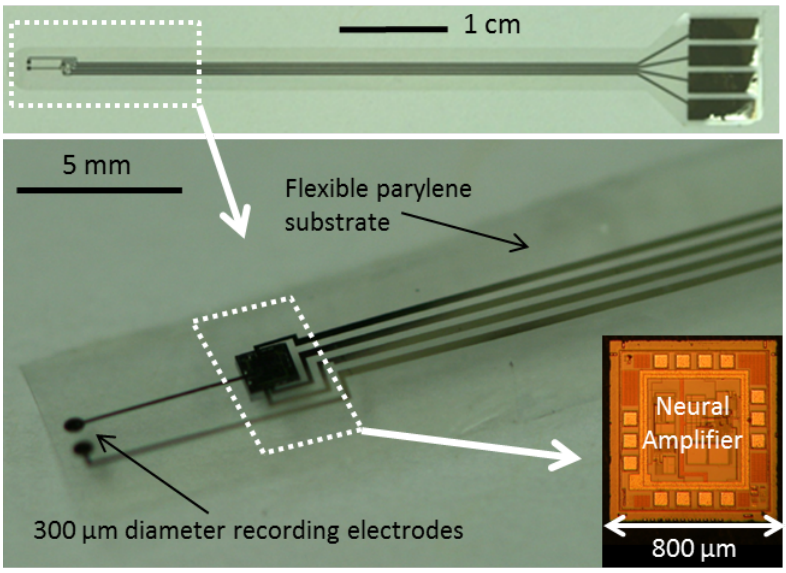

Figure 45. Neural recording array and detail of custom amplifier die.

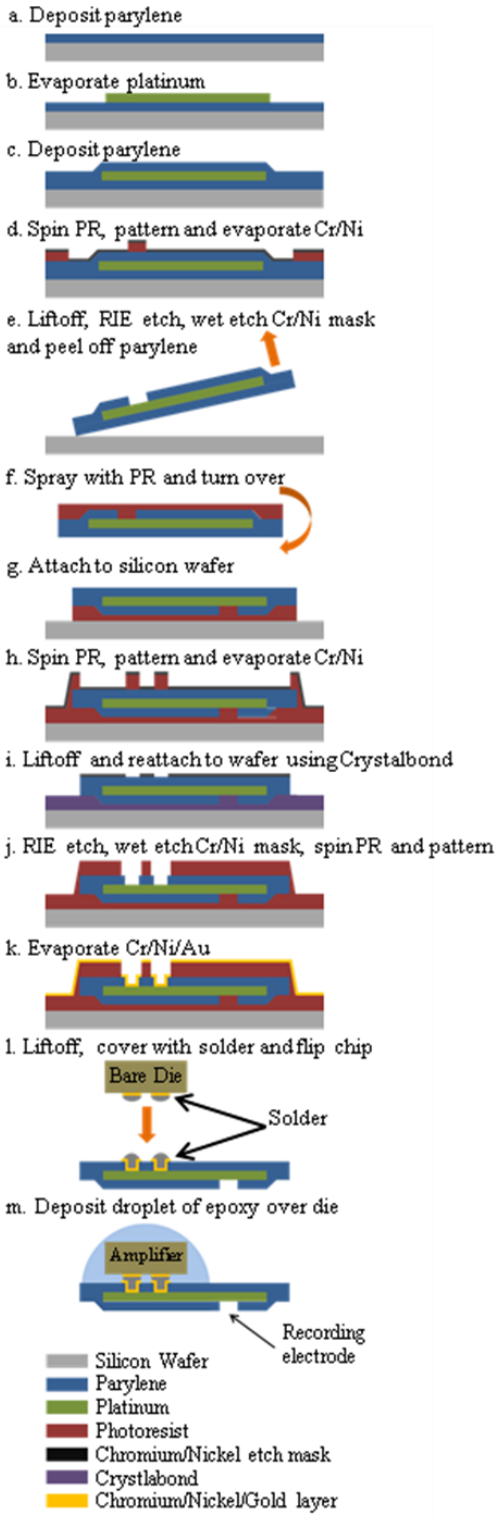

Figure 46. Parylene-platinum array fabrication and IC integration procedure.

4.3.2 Double-sided, Self-aligned Neural Array Microfabrication

While the IC integration onto parylene process described in the previous section is viable for single-IC designs, the major drawback of that process is that the required photolithography on the back side of the array has very low accuracy. The back side photolithography step is necessary to open the parylene layer for IC bonding. Inverting the array on the silicon wafer results in deformation of the pliable polymer material, making it impossible to align a new pattern to the existing one. A solution to this problem must eliminate the photolithography step on the back of the array. A fabrication procedure that I have developed, illustrated in Figure 47, uses gold electroplating to essentially build the entire array "upside down" on the handle wafer, and then etch away the sacrificial gold and parylene layers without the need for photolithography.

A 5 μm layer of sacrificial is deposited onto parylene onto the silicon wafer, then the parylene is coated with a 40 nm layer of gold which will act as a gold electroplating seed layer. Another layer of parylene is deposited (10 μm thick) and photolithography is performed to mask and etch openings in the parylene that correspond to the layout of the IC contact pads. 10 μm tall gold posts are then electroplated through the openings in the parylene layer (Figure 47, step 1). The next two steps follow the standard parylene array fabrication procedure, where platinum or iridium traces and electrode pads are deposited onto the wafer. The last layer of parylene is deposited and openings are etched into it to create electrodes (Figure 47, step 2). The entire parylene array is then peeled off the wafer, flipped over and secured with Crystalbond resin back onto the silicon template. An RIE etch eliminates the sacrificial parylene and a gold wet etch quickly etches away the seed layer, leaving only the array (Figure 47, steps 3 and 4). ICs are then secured onto the parylene using the flip-chip bonding process described in the previous section.

This new process allows for placement of an arbitrarily large number of ICs with dense contact pad geometries onto the flexible parylene electrode arrays.

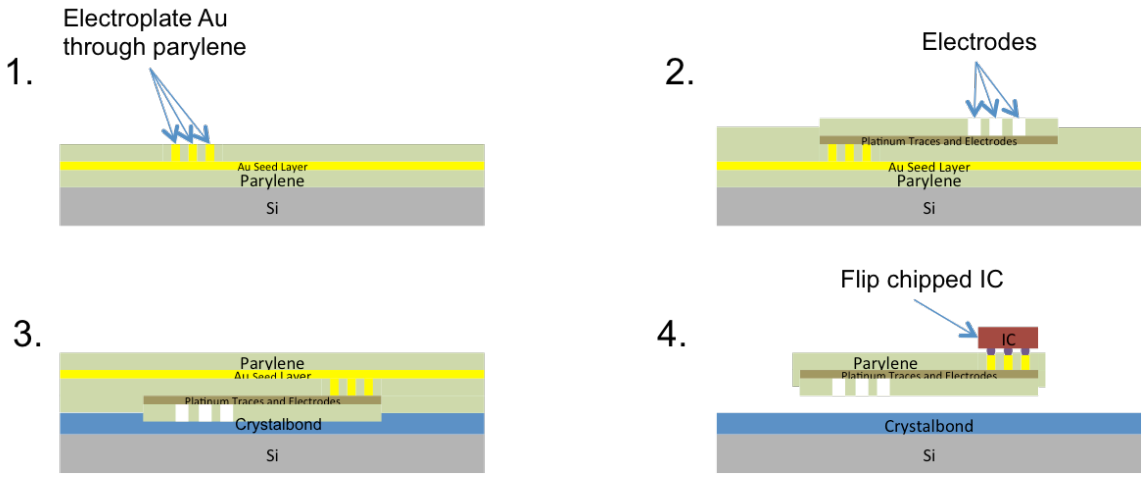

Figure 47. Scalable microfabrication process for IC integration onto planar neural electrode arrays. The process requires no photo-lithography on the back side of the array.

4.3.3 Parylene Microfabrication Pitfalls and Methods to Avoid Them

Several highly non-trivial negative aspects of parylene fabrication have arisen during the process development. Qualities that make parylene a desirable material for biomedical devices, create unique problems during the microfabrication process. Parylene-C melts at 290 °C, and will start to deform at temperatures above 200 °C. Many of the microfabrication steps one takes for granted when working with traditional semiconductor materials need to be re-developed to work with parylene. This section will describe the changes that need to be made to the metal evaporation, plasma etching, electroplating, lift-off and parylene coating steps in order for the microfabrication to be successful.

Figure 48 demonstrates the common parylene deformation patterns seen following a metal deposition step and liftoff. Enough stress can accumulate during a high-temperate large-area metal evaporation to introduce cracks into the parylene substrate. While the inside of the circle will be etched away in Figure 48, the sub-metal cracks seen under the metal layer in the right hand corner of the photograph will result in a destroyed array upon detachment from the carrier wafer. In order to resolve this issue, one must significantly lower the metal evaporation rate, thus lowering the deposition temperature. This reduces the amount of mechanical stress seen by the parylene

substrate upon the wafer's cooling subsequent to the metal deposition. Generally, a deposition rate of 1 Angstrom per second should not be exceeded.

Special care must be taken when a higher melting temperature metal, such as platinum is deposited. If a positive photoresist is used, the metal will partially cover the vertical parts of the photoresist pattern, forming a solid layer across the whole wafer. Upon the evaporation's end, as the wafer cools, the parylene can stretch and constrict such that all solid platinum traces acquire micro fissures, rendering the metal traces non-conductive. I suggest using either a lift-off optimized (LOR) negative photo-resist, or a sub-20 nm thick layer of chromium, which can act as a lift-off resist when submerged into liquid chromium etch. It has also been shown that inserting cooling 1-minute long pauses into the evaporation process can help lower the deposition temperature.

On a similar note, parylene deformation during a large gold electroplating seed layer (titanium/gold, 10 nm/100 nm) deposition can be so severe that the seed layer largely delaminates upon the wafer's extraction from the metal evaporator tool. One solution is to avoid evaporating a full-wafer seed layer, rather limiting it to 2 mm wide traces that cover all the electroplating locations. Together with a lowered metal evaporation temperature (i.e. lowered evaporation rate) the seed layer delamination problem can be avoided.

Multi-parylene layer devices are especially vulnerable to damage from particles embedded between the parylene layers. Although the particle may fall on an unpatterned area of the wafer and seemingly not affect the quality of the microfabricated structure, it can be devastating when the wafer is inserted into a sonicator during liftoff. The embedded particle acts as a focus for rapid delamination of the two parylene layers. An example of such an occurrence can be seen in Figure 49 a and b. The way to resolve this issue is to minimize the use of sonication for lift-off, and be exceedingly thorough in cleaning the wafers prior to parylene depositions. This is rather difficult, considering that the parylene coater tool itself can generate a large number of particles. A way to avoid sonication during liftoff is to minimize the amount of large-area metal sections in the pattern

which generally take a long time to liftoff, which is often shortened using sonication. Any remaining metal flakes can be removed by applying a strong stream of acetone to the wafer surface. However, one must be careful to not dislodge electroplated columns. These are particularly sensitive to any mechanical intervention to the surface of the wafer, as can be seen in Figure 49 c.

Plasma etching of parylene is normally the final microfabrication step. There can be three or more layers of parylene on the wafer, each potentially harboring particle-contaminant-caused air bubbles. When the wafer is transferred into the low pressure (10^{-6} torr) etch chamber, the air bubbles can rapidly expand, delaminating the entire parylene layer from the silicon substrate. When delaminated, the parylene layer loses its ability to transfer the heat generated in the plasma etch into the etcher chuck, and is destroyed (Figure 49 d). A way to avoid this is to score the surface of the parylene layer with a sharp razor blade, thus creating pathways for any trapped air to escape. The scored areas will be removed by the plasma etch.

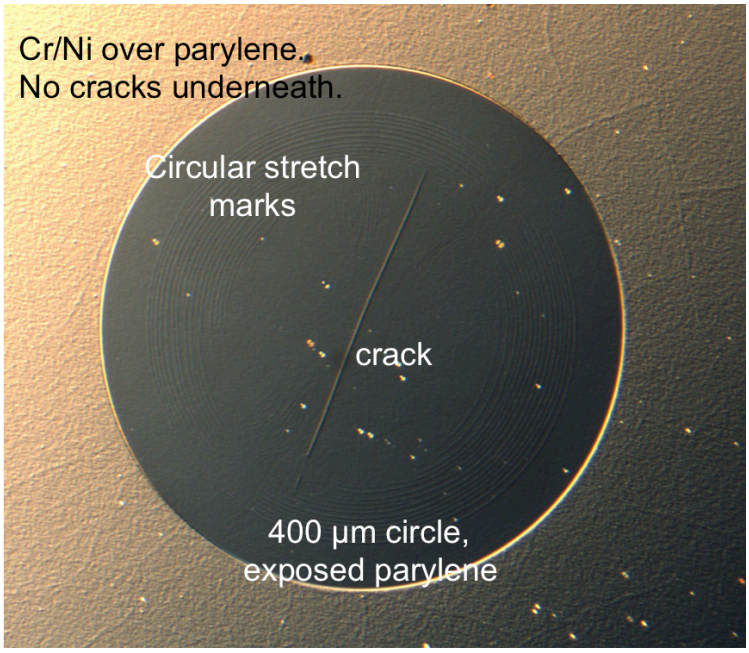

Figure 48. Optical microscope image illustrating stress damage to parylene substrates during metal deposition.

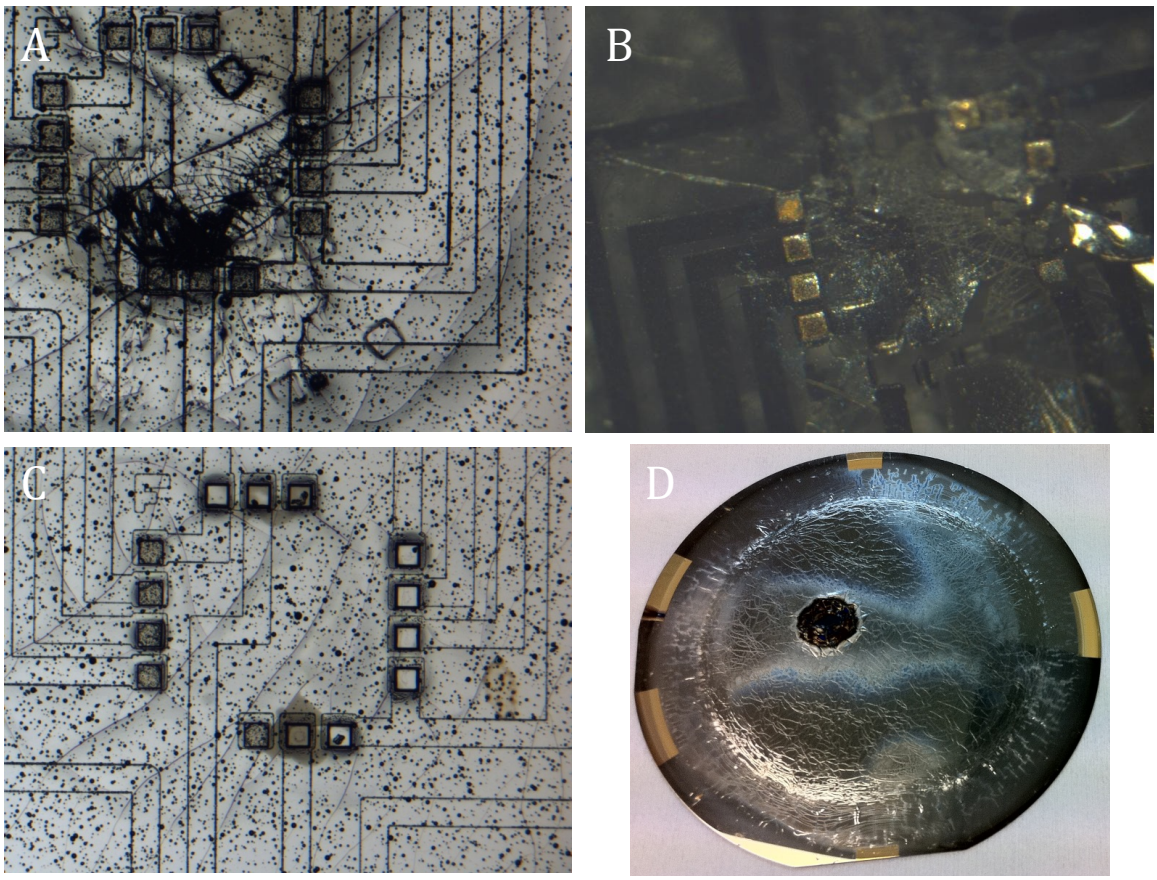

Figure 49. Various common failure modes during parylene microfabrication. a) particles trapped between parylene layers. b) cracked parylene. c) missing electroplated columns. d) catastrophic entrapped air bubble release which delaminated the entire parylene layer.

4.3.4 Laplacian Active Neural Array

One of the biggest challenges in cortical neural measurements is figuring out the foci of the detected electrical signals (Hjorth, 1975). A technique used in electroencephalogram (EEG) recording calculates the surface Laplacian (equation 3) at each measurement electrode in order to locate the excitation sources (MacKay, 1983).

$$\frac{\partial^2 V}{\partial x^2} + \frac{\partial^2 V}{\partial y^2} = \nabla^2 V \qquad (3)$$

We can use the same technique to improve our ECoG arrays, at once solving the tricky problem of reference electrode location for measurements, improving correlated noise interference as well as decreasing the computing power needed by analyzing a portion of the signal, in analog, on the electrode array itself. It has been shown in the literature (Oostendorp, 1989; Hjorth, 1975) that for an evenly spaced array of electrodes, an approximation to the Laplacian is calculated by taking the difference of the potential measurement at a central electrode and subtracting from it the mean of the potentials from the surrounding electrodes.

An electrode arrangement shown in Figure 50 describes how one could implement the computation of the Laplacian using standard circuit components. In this circuit, the mean signal from three surrounding electrodes (Vb, Vc and Vd) is subtracted from the signal measured at the central electrode, V1. An improvement on this scheme can include sharing of the surrounding electrodes with other central electrodes in order to decrease the complexity and density of the circuit.

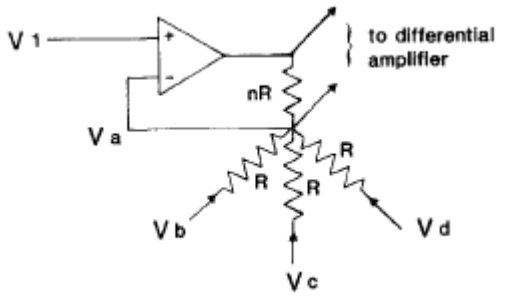

Figure 50. A 4-electrode unit cell for the calculation of the Laplacian, (per MacKay, 1983). V1 is the central electrode signal, Vb, Vc and Vd are the three equidistant surrounding electrodes. The circuit computes the difference between V1 and a mean of Vb, Vc and Vd. The output read off of the resistor nR is the difference multiplied by 3n (MacKay, 1983).

The advantage of implementing this circuit on the electrode array over performing the calculation on a computer is the significant decrease in the number of output wires connecting the implant to a control device, which significantly simplifies both the implantation and measurement processes. Also, by eliminating the low frequency common-mode signals normally present across

the entire electrode grid, we can decrease the complexity of the custom amplifier circuits being built for this project.

Fabrication of this circuit requires the assembly of several off-the-shelf and custom IC's – a low noise amplifier, an op-amp and several resistors. Assembly was performed per the method outlined in the previous section, using the flip-chip technique.

As can been seen in Figure 51, the reference electrodes (B, C, and D) are laid out in an equilateral triangle shape around the central recording electrode (C). Signals from all electrodes are first pre-amplified using the low-noise amplifiers described in Section 4.3.1. An op-amp (OP37) is then used in an adder-circuit-like configuration to generate a signal, V_{LP} across resistor R_2, that is proportional to the difference between the signal at electrode A and the mean of signals at electrodes B, C and D. The bare die parts sourced for this purpose were the LNAs (Brian Otis Lab), SMT resistors (Panasonic 0201 size; 30, 300 and 900 kΩ; Digikey) and a number of OP37 op-amps (Analog Devices via Micross Components). Contact pads on both the LNAs and OP37 chips were coated with gold using electroless nickel-gold deposition technique (performed by CV Inc.) in order to facilitate solder coating.

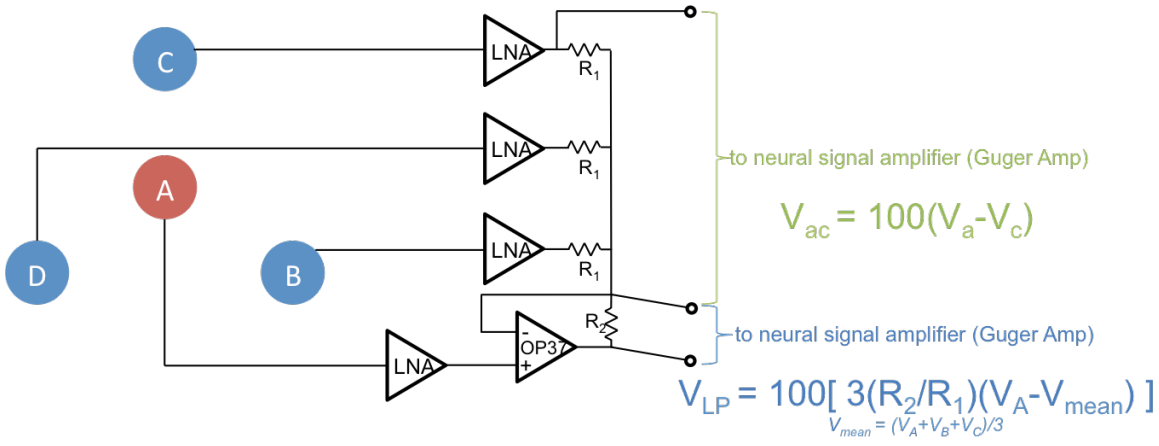

Figure 51. The schematic for a single Laplacian cell and the required electronic components.

A functional schematic and specific pad connection diagram is illustrated in Figure 52. Note that it may be impossible to place an entire circuit on a single layer of parylene. In that case, an extra layer of parylene must be deposited to make space for additional metal traces.

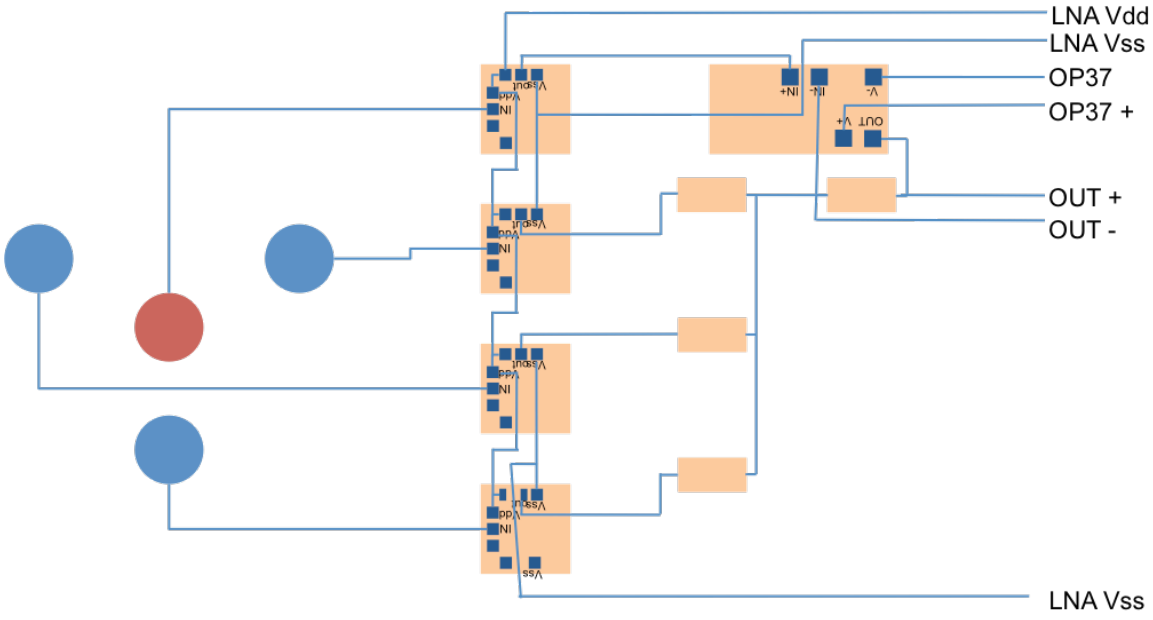

Figure 52. A functional layout and pad-out of all the components of the Laplacian circuit. Red electrode is the center, recording electrode, while the three blue electrodes serve as the combined reference electrodes.

The final layout for the microfabricated Laplacian array is presented in Figure 53. It became apparent during the assembly process that the metal pads designed for the 0603 sized resistor were too large, and would delaminate when the array was bent. Instead, 0201 sized resistors were used (requiring a change to the flip chip tooling) as can be seen in Figure 54. The array also contained one unamplified electrode that could be used to validate the performance improvement of a Laplacian circuit.

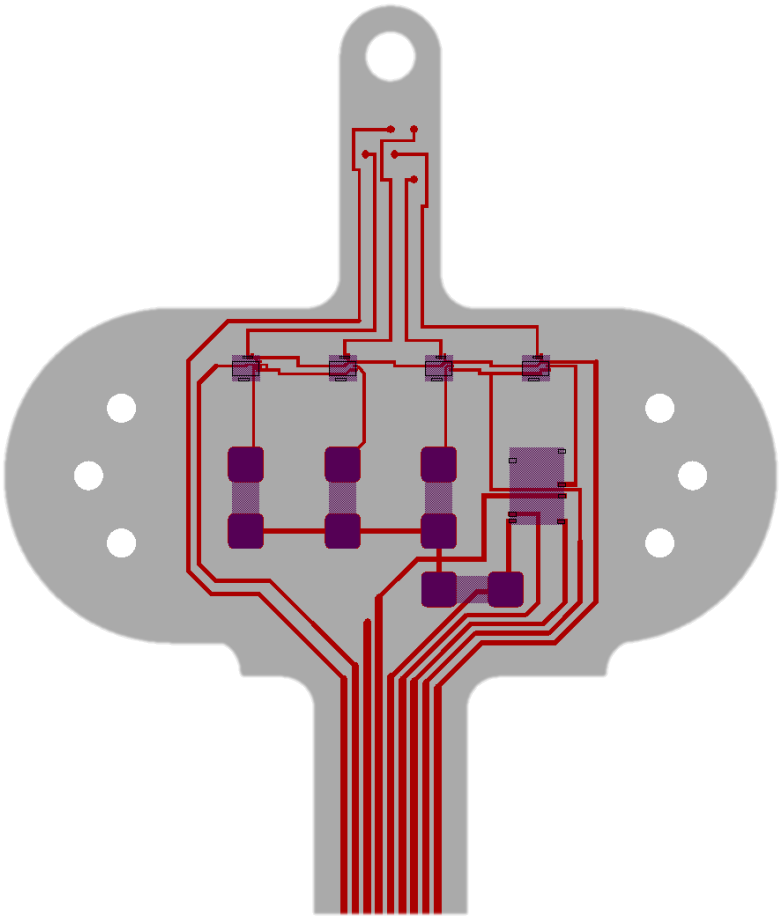

Figure 53. The electronics end of the Laplacian array.

Unfortunately, while the LNAs and the resistors were repeatedly placed successfully, it was not possible to reliably connect the OP37 chip to the parylene substrate. OP37's pads were very close to the side of the chip, allowing some solder to link the pad and the bulk of the device. Such a connection would lead to wildly unpredictable behavior of the operational amplifier, making the entire circuit unusable. Furthermore, the chip also contained several test pads in close proximity to active pads. Electrical shorts would occasionally form between the two, also leading to incorrect device behavior.

However, I believe it is quite possible to assemble this circuit given a more controlled solder deposition and chip placement systems which would both eliminate the problem of excess solder

deposition and excess downward pressure on the chip during soldering. Solving both of these issues will result in a precise connection between the chip's pads and the parylene substrate.

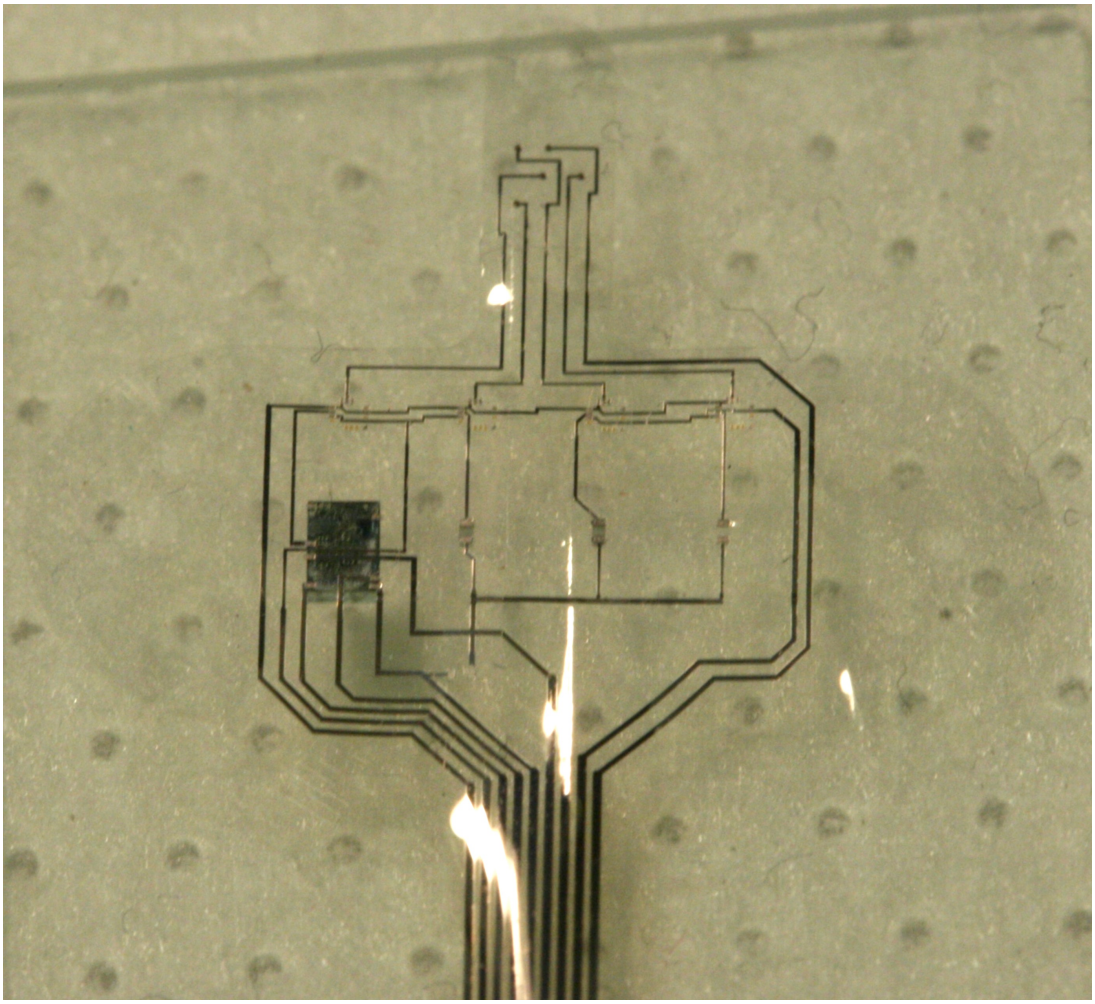

Figure 54. A partially assembled Laplacian array. The operational amplifier and two resistors are attached.

4.3.5 4-LNA Active Electrode Array

I have successfully assembled four Low Noise Amplifiers (LNAs) onto the double-sided parylene surface, thus demonstrating the fundamental effectiveness of the aforementioned double-sided, self-aligned fabrication process.

The 4-LNA device, in itself, is a highly capable active neural array that allows for pre-amplification of neural signals at their source, thus decreasing the noise that would have otherwise been accumulated across a lengthy signal path. All four LNA devices have remained functional

during the assembly process, Figure 55 demonstrates the output of the LNA in response to a 100 Hz input signal with an amplitude similar to those with physiological relevance (1 mV – 6 mV). Note that signals above 6 mV p-p are clipped due to limitations of the LNA on its voltage output. Figure 56 shows a measured frequency response of the LNA, based on a 2 mV amplitude sine wave input. The LNA maintains a gain of nearly 40 dB across the majority of the 5-10000 Hz range.

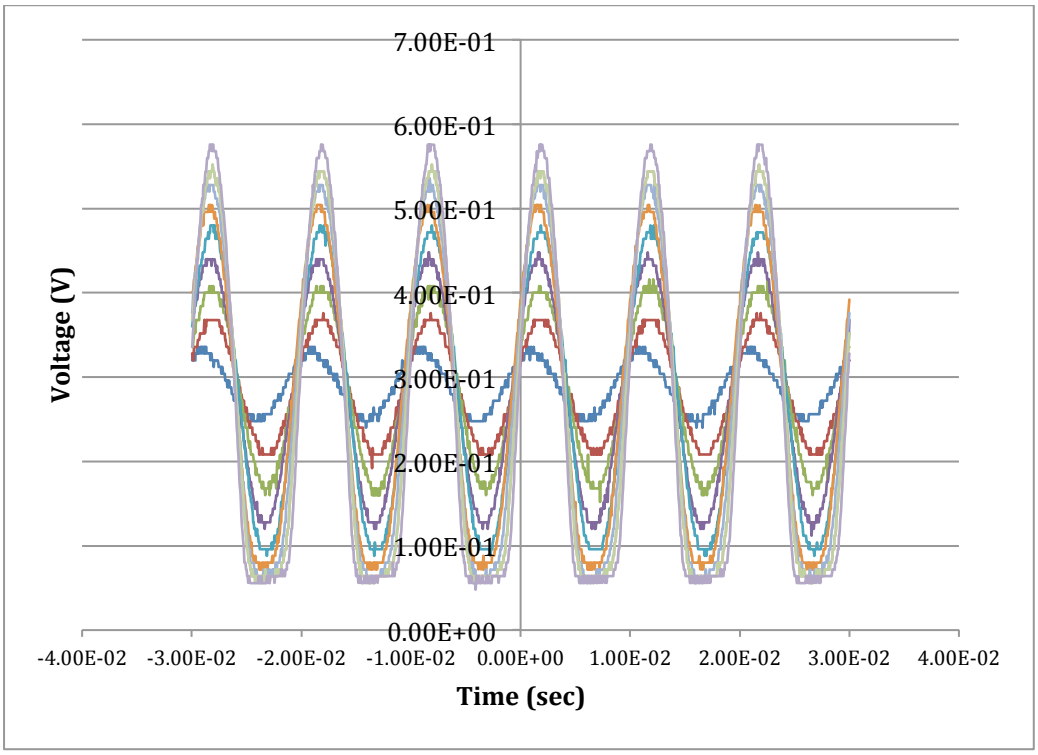

Figure 55 demonstrates a representative output of the 40 dB LNA, for various amplitudes of 100 Hz input signal. Signal amplitudes vary from 1 mV to 10 mV in .5 mV increments.

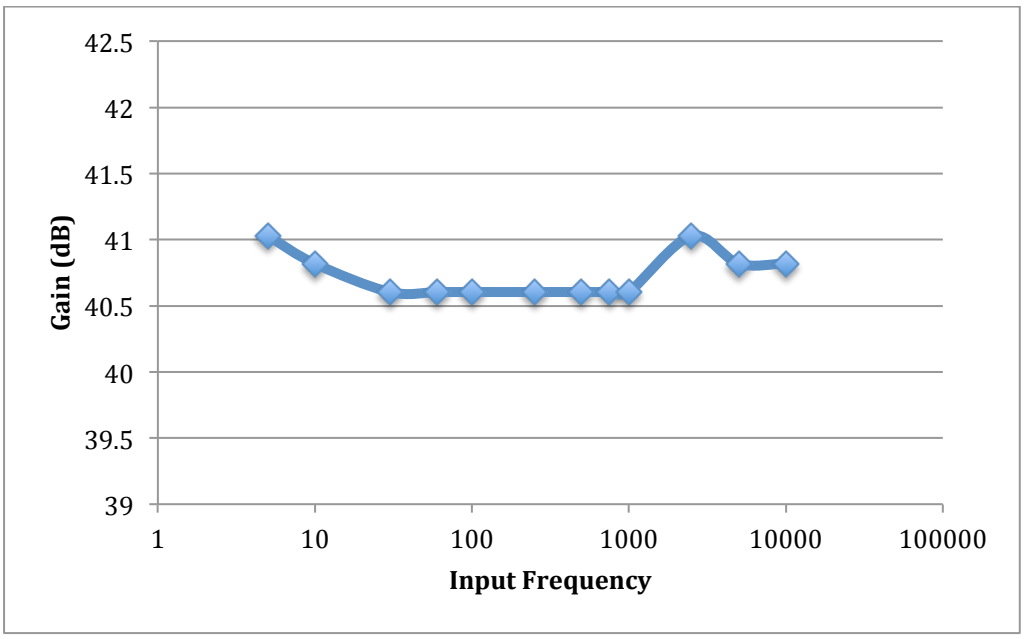

Figure 56. Frequency response of an LNA assembled on a parylene substrate.

5 Conclusion

In this dissertation I have described three main directions of my research related to the engineered interface between biological systems and novel microfabricated devices used to quantify various characteristics of said biological systems.

In Chapter 2, I have described two novel nanoscale devices that were designed, microfabricated and characterized with the goal of creating a standalone biomolecular detection system. I presented a reliable microfabrication method for an amperometric nanochannel biosensor, extensively tested and theoretically described its conduction characteristics based on a diffusion model. While a proposed functionalization scheme has not been fully successful when used with nanochannels, I have described a fast and effective method of validating functionalization sequences in bulk, using fluorescently tagged molecular markers. I have also described an effort to create a biomolecular sensor that exploits the high surface area to volume ratio of a semiconductive silicon nanowire to measure the concentration of specific biomolecules in solution. A detailed fabrication method of the nanowire sensor was presented, along with transistor-like

characterization results, an antibody surface functionalization procedure, as well as initial sensing results. I have also discussed the various difficulties that arise in building a functional semiconductor device that can interface with liquids, as well as several ideas that can be used to resolve them.

Chapter 3 describes the fabrication, characterization and first in-vivo testing of a microscale amperometric intraocular glucose sensor. While the device showed great promise when tested in-vitro, the in-vivo testing showed the need for further development of a biomolecule selective coating that can protect such a glucose sensor from a multitude of interfering molecular noise sources found in an in-vivo eye system. Furthermore, I have described a mechanical system that can be used for testing contact lens based glucose sensors that have been developed in my lab, in life-like eye conditions. Together with a simulated tear duct system, the eyelid movement simulator can create realistic tear fluid distributions on the contact lens, allowing for sensor testing without the expense of in-vivo experiments.

Chapter 4 presents my efforts in creating novel types of non-invasive, highly flexible cortical and spinal electrode arrays that can be integrated into an implantable RBCI system. A detailed microfabrication procedure is described that allows for reliable creation of two-sided parylene based neural electrode arrays that can be combined with multiple types of electronic components. Several passive electrode array designs are presented, as well as an active array that integrates four low noise neural amplifiers. Extensive electrode characterization describes the various electrical properties of both platinum and iridium oxide arrays, as well as their potential for long-term viability. Finally, in-vivo stimulation and recording experiments are described that demonstrate the differences between in-vivo and in-vitro electrode behaviors.

In my research, I have tackled many challenges surrounding successful integration of inorganic, microfabricated devices with oftentimes unpredictable in-vivo systems. The long term

potential of this work lies in the creation of novel therapeutic medical devices that can quickly diagnose, manage or even treat various types of diseases.

6 References

Sections of Ch. 2 were taken from:

Afanasiev A., Lähdesmäki I., Parviz B. A. "Fabrication and electrical characterization of integrated nano-scale fluidic channels", Microsystem Technologies, vol. 17, 2011

Afanasiev A., Mehta R., Parviz B.A., "Nanowire Sensors for Biomolecular Detection", AIAA Infotech@Aerospace Conference and Exhibit, April 2009

Sections of Ch. 3 were taken from:

Afanasiev A., Yao H., Marcheselli C., Lähdesmäki I., and Parviz B.A. "A Synthetic Eye Platform for Testing Contact Lenses with Integrated Electronic Biosensors", Nanotechnology (IEEE-NANO), 2010 10th IEEE Conference on, Aug. 2011

Ali M, Schiedt B, Neumann R, Ensinger W "Biosensing with Functionalized Single Asymmetric Polymer Nanochannels". Macromolecular bioscience, vol.10 p. 28–32, 2010

Armani AM, Kulkarni RP, Fraser SE, Flagan RC, Vahala KJ "Label-Free, Single-Molecule Detection with Optical Microcavities". Science vol, 317 p. 783-787, 2007

Baca, J.T., C.R. Taormina, E. Feingold, D.N. Finegold, J.J. Grabowski, and S.A. Asher, "Mass spectral determination of fasting tear glucose concentrations in nondiabetic volunteers," Clinical chemistry, vol. 53, p. 1370, 2007

Berger T. W., A. Ahuja, S. H. Courellis, S. A. Deadwyler, G. Erinjippurath, G. A. Gerhardt, G. Gholmieh, J. J. Granacki, R. Hampson, M. C. Hsaio, and others, "Restoring lost cognitive function," Engineering in Medicine and Biology Magazine, IEEE, vol. 24, no. 5, pp. 30–44, 2005.

Cogan S. F., "Neural stimulation and recording electrodes," Annu. Rev. Biomed. Eng., vol. 10, pp. 275–309, 2008.

Cui, Y., Wei, Q.Q., Park, H.K., and Lieber, C.M., "Nanowire nanosensors for highly sensitive and selective detection of biological and chemical species," Science, Vol. 293, No. 5533, pp. 1289-1292, 2001,.

Curreli, M., Zhang, R., Ishikawa, F.N., Chang, H.K., Cote, R.J., Zhou, C., et al, "Real-Time, Label-Free Detection of Biological Entities Using Nanowire-Based FETs," IEEE Transactions on Nanotechnology, Vol. 7, No. 6, pp. 651-667, 2008,

Cvoro V. et al., "Associations Between Diffusion and Perfusion Parameters, N-Acetyl Aspartate, and Lactate in Acute Ischemic Stroke," Stroke, vol. 40, no. 3, pp. 767-772, 2009.

Daiguji H, Yang P, Majumdar A, "Ion Transport in Nanofluidic Channels". Nano Letters, vol. 4, p.137-142, 2004

Daniels JS, Pourmand N, "Label-Free Impedance Biosensors: Opportunities and Challenges." Electroanalysis, vol. 19, p. 1239-1257, 2007

Durand NFY, Renaud P, "Label-free determination of protein–surface interaction kinetics by ionic conductance inside a nanochannel", Lab Chip, vol. 9, p. 319-324, 2009

Elfstrom, N., and Linnros, J., "Avalanche breakdown in surface modified silicon nanowires," Applied Physics Letters, Vol. 91, No. 10, p. 103502(1-3), 2007

Elfstrom, N., Juhasz, R., Sychugov, I., Engfeldt, T., Karlstrom, A.E. and Linnros, J., "Surface charge sensitivity of silicon nanowires: Size dependence," Nano Letters, Vol. 7, No. 9, pp. 2608-2612, 2007

Evans V., C. Vockler, M. Friedlander, B. Walsh, and M. D. P. Willcox, "Lacryglobin in human tears, a potential marker for cancer," Clinical & Experimental Ophthalmology, vol. 29, no. 3, pp. 161–163, 2001.

Goluch ED, Wolfrum B, Singh PS, Zevenbergen MAG, Lemay SG "Redox cycling in nanofluidic channels using interdigitated electrodes." Anal Bioanal Chem, vol. 394, p. 447-456, 2009

Grieshaber D, MacKenzie R, Voeroes J, Reimhult E "Electrochemical biosensors-Sensor principles and architectures." Sensors, vol. 8, p. 1400–1458, 2008

Grus, F. H., S.C. Joachim and N. Pfeiffer, "Proteomics in ocular fluids," PROTEOMICS – Clinical Applications, vol. 1, pp. 876–888, 2007

Haynes WM, Lide DR (2011) CRC Handbook of Chemistry and Physics. CRC Press, Boca Raton, Fl

Hjorth, B., "An on-line transformation of EEG scalp potentials into orthogonal source derivations," Electroencephalography and Clinical Neurophysiology, vol. 39, no. 5, pp. 526–530, 1975.

Homola J "Surface Plasmon Resonance Sensors for Detection of Chemical and Biological Species", Chem Rev, vol. 108, p. 462-493, 2008

Hudak, E., J. Mortimer, and H. Martin, "Platinum for neural stimulation: voltammetry considerations," Journal of Neural Engineering, vol. 7, p. 026005, 2010.

Ihalainen P, Peltonen J "Immobilization of streptavidin onto biotin-functionalized Langmuir-Schaefer binary monolayers chemisorbed on gold", Sensors and Actuators B: Chemical, vol. 102, p. 207–218, 2004

Karnik R, Castelino K, Fan R, Yang P, Majumdar A "Effects of Biological Reactions and Modifications on Conductance of Nanofluidic Channels.", Nano Letters, vol. 5, p. 1638-1642, 2005

King-Smith P. E., B. A. Fink, J. J. Nichols, K. K. Nichols, R. J. Braun, and G. B. McFadden, "The Contribution of Lipid Layer Movement to Tear Film Thinning and Breakup," Investigative Ophthalmology & Visual Science, vol. 50, no. 6, pp. 2747-2756, 2009.

Kutchoukov VG, Pakula L, Parikesit GOF, Nanver LK, Bossche "A Fabrication of nanofluidic devices in glass with polysilicon electrodes." Sensors and Actuators A: Physical, vol. 123-124, p. 602-607, 2005

Lee N.Y. and B.H. Chung, "Novel Poly(dimethylsiloxane) Bonding Strategy via Room Temperature "Chemical Gluing"," Langmuir, vol. 25, pp. 3861-3866, 2009

Li W., D. C. Rodger, A. Pinto, E. Meng, J. D. Weiland, M. S. Humayun, and Y. C. Tai, "Parylene-based integrated wireless single-channel neurostimulator," Sensors and Actuators A: Physical, 2010.

Li W., D. C. Rodger, and Y. C. Tai, "Integrated wireless neurostimulator," Micro Electro Mechanical Systems, 2009. MEMS 2009. IEEE 22nd International Conference on, 2009, pp. 248–251.

Li W., D. C. Rodger, E. Meng, J. D. Weiland, M. S. Humayun, and Y.-C. Tai, "Wafer-Level Parylene Packaging With Integrated RF Electronics for Wireless Retinal Prostheses," Journal of Microelectromechanical Systems, vol. 19, no. 4, pp. 735–742, 2010.

Li, Z., Chen, Y., Li, X., Kamins, T.I., Nauka, K., and Williams, R.S., "Sequence-specific label-free DNA sensors based on silicon nanowires," Nano Letters, 2, Vol. 4, No. 2, pp. 245-247, 2004

Lund, J., Mehta, R., and Parviz, BA, "Label-free direct electronic detection of biomolecules with amorphous silicon nanostructures," Nanomedicine, Vol. 2, No. 4, pp. 230-238, 2006

MacKay, D.M., "On-line source-density computation with a minimum of electrodes," Electroencephalography and clinical neurophysiology, vol. 56, no. 6, pp. 696–698, 1983.

Maleki T, Mohammadi S, Ziaie B "A nanofluidic channel with embedded transverse nanoelectrodes." Nanotechnology, vol. 20, p. 105302-105307, 2009

March W.F., A. Mueller, and P. Herbrechtsmeier, "Clinical trial of a noninvasive contact lens glucose sensors," Diabetes Techn. Therm, vol. 6, pp. 782-789, 2004

Merrill, D. R., M. Bikson, and J. G. Jefferys, "Electrical stimulation of excitable tissue: design of efficacious and safe protocols," Journal of Neuroscience Methods, vol. 141, no. 2, pp. 171–198, 2005.

Nair, P.R., and Alam, M.A., "Design considerations of silicon nanowire biosensors," IEEE Transactions on Electron Devices, Vol. 54, No. 12, pp. 3400-3408, 2007

Nandra, M. S., I. A. Lavrov, V. R. Edgerton, and Y. C. Tai, "A parylene-based microelectrode array implant for spinal cord stimulation in rats," in Micro Electro Mechanical Systems (MEMS), 2011 IEEE 24th International Conference on, pp. 1007–1010.

Ohashi Y., M. Dogru, and K. Tsubota, "Laboratory findings in tear fluid analysis," Clinica Chimica Acta, vol. 369, no. 1, p. 17–28, 2006.

Oostendorp T. F., A. van Oosterom, and G. Huiskamp, "Interpolation on a triangulated 3D surface," Journal of Computational Physics, vol. 80, no. 2, pp. 331–343, 1989.

Patolsky F, Filanovsky B, Katz E, Willner I "Photoswitchable Antigen–Antibody Interactions Studied by Impedance Spectroscopy", J Phys Chem B, vol. 102, p. 10359-10367, 1998

Patolsky, F., Zheng, G.F., Hayden, O., Lakadamyali, M., Zhuang, X. and Lieber, C.M., "Electrical detection of single viruses," PNAS, Vol. 101, No. 39, pp. 14017-14022, 2004

Peters, K. and T.J. Millar, "The role of different phospholipid on tear break-up time using a model eye," Current Eye Research, vol. 25, pp. 55-60, 2002

Pletcher D, Group SE (2001) Instrumental methods in electrochemistry. Horwood Publishing, Westergate, England

Rodger, D. C., J. D. Weiland, M. S. Humayun, and Y. C. Tai, "Scalable high lead-count parylene package for retinal prostheses," Sensors and Actuators B: Chemical, vol. 117, no. 1, pp. 107–114, 2006.

Rubehn, B., C. Bosman, R. Oostenveld, P. Fries, and T. Stieglitz, "A MEMS-based flexible multichannel ECoG-electrode array," Journal of neural engineering, vol. 6, p. 036003, 2009.

Schoch R, Han J, Renaud P, "Transport phenomena in nanofluidics", Rev Mod Phys, vol. 80, p. 839-883, 2008

Stein D, Kruithof M, Dekker C "Surface-Charge-Governed Ion Transport in Nanofluidic Channels.", Phys Rev Lett vol. 93, p. 035901-1-035901-4, 2004

Stern, E., Klemic, J.F., Routenberg, D.A., Wyrembak, P.N., Turner-Evans, D.B., Hamilton, A.D., et al., "Label-free immunodetection with CMOS-compatible semiconducting nanowires." Nature, Vol. 445, No. 7127, pp. 519-522, 2007

Tapaszto, I., "Pathophysiology of human tears," Int. Ophthalmol. Clin., vol. 13, pp. 119-147, 1973

van Haeringen, N.J., "Clinical biochemistry of tears," Survey of Ophthalmology, vol. 26, pp. 84-96, 1981

Viventi, J., D.-H. Kim, L. Vigeland, E. S. Frechette, J. A. Blanco, Y.-S. Kim, A. E. Avrin, V. R. Tiruvadi, S.-W. Hwang, A. C. Vanleer, D. F. Wulsin, K. Davis, C. E. Gelber, L. Palmer, J. Van der Spiegel, J. Wu, J. Xiao, Y. Huang, D. Contreras, J. A. Rogers, and B. Litt, "Flexible, foldable, actively multiplexed, high-density electrode array for mapping brain activity in vivo," Nature Neuroscience, Nov. 2011.

Wang, W.U., Chen, C., Lin, K.H., Fang, Y., and Lieber, C.M., "Label-free detection of small-molecule-protein interactions by using nanowire nanosensors," PNAS, Vol. 102, pp. 3208-3212, 2005

Wen Li, D. C. Rodger, E. Meng, J. D. Weiland, M. S. Humayun, and Yu-Chong Tai, "Wafer-Level Parylene Packaging With Integrated RF Electronics for Wireless Retinal Prostheses," Microelectromechanical Systems, Journal of, vol. 19, pp. 735–742, 2010.

Yao, H., A.J. Shum, M. Cowan, I. Lahdesmaki, and B.A. Parviz, "A contact lens with embedded sensor for monitoring tear glucose level," Biosensors and Bioelectronics, vol. 26, pp. 3290-3296, 2010.

Yao, H., Afanasiev, A., Lahdesmaki, I., Parviz, B.A. "A dual microscale glucose sensor on a contact lens, tested in conditions mimicking the eye", 2011 IEEE 24th International Conference on, Micro Electro Mechanical Systems (MEMS)

Yeager, D. J., J. Holleman, R. Prasad, J. R. Smith, and B. P. Otis, "NeuralWISP: A Wirelessly Powered Neural Interface With 1-m Range," IEEE Trans. Biomed. Circuits Syst., vol. 3, pp. 379–387, 2009.

Zayats M, Katz E, Willner I "Electrical contacting of flavoenzymes and NAD (P)+-dependent enzymes by reconstitution and affinity interactions on phenylboronic acid monolayers associated with Au-electrodes.", Journal of the American Chemical Society, vol. 124, p. 14724–14735, 2002

Zheng, G.F., Patolsky, F., and Lieber, C.M., "Multiplexed electrical detection of cancer marker proteins and single viruses by nanowire fet arrays,"Abstracts of papers of the American Chemical Society, Vol. 229, p. U782-U782, 2005